CHARACTERIZATION AND MODELING OF THORACO-ABDOMINAL RESPONSE TO BLAST WAVES

Volume 4. Biomechanical Model of Thorax Response to Blast Loading

Annual/Final Report

May 1985

C. J. Chuong
J. H. Stuhmiller, Principal Investigator

JAYCOR
11011 Torreyana Road
San Diego, California 92121

Contract No. DAMD17-82-C-2062

Supported by

U. S. Army Medical Research and Development Command
Fort Detrick, Frederick, Maryland 21701

The findings in this report are not to be construed as an official Department of the Army position unless so designated by other authorized documents.

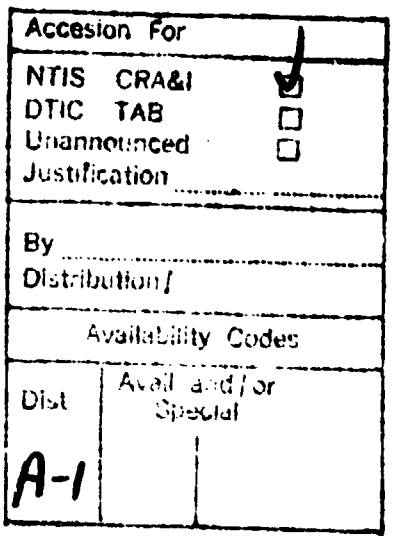

SECURITY CLASSIFICATION OF THIS PAGE

REPORT DOCUMENTATION PAGE

Form Approved
OMB No. 0704-0188

1a. REPORT SECURITY CLASSIFICATION UNCLASSIFIED	1b. RESTRICTIVE MARKINGS
2a. SECURITY CLASSIFICATION AUTHORITY	3. DISTRIBUTION / AVAILABILITY OF REPORT Approved for public release; distribution unlimited
2b. DECLASSIFICATION / DOWNGRADING SCHEDULE	
4. PERFORMING ORGANIZATION REPORT NUMBER(S)	5. MONITORING ORGANIZATION REPORT NUMBER(S)
6a. NAME OF PERFORMING ORGANIZATION JAYCOR 6b. OFFICE SYMBOL (If applicable)	7a. NAME OF MONITORING ORGANIZATION
6c. ADDRESS (City, State, and ZIP Code) 11011 Torreyana Road San Diego, California 92121	7b. ADDRESS (City, State, and ZIP Code)
8a. NAME OF FUNDING / SPONSORING ORGANIZATION U.S. Army Medical Research & Development Command 8b. OFFICE SYMBOL (If applicable)	9. PROCUREMENT INSTRUMENT IDENTIFICATION NUMBER DAMD17-82-C-2062
8c. ADDRESS (City, State, and ZIP Code) Fort Detrick Frederick, Maryland 21701-5012	10. SOURCE OF FUNDING NUMBERS PROGRAM ELEMENT NO. 61102A; PROJECT NO. 3M1 61102BS10; TASK NO. CG; WORK UNIT ACCESSION NO. 087

11. TITLE (Include Security Classification)
(U) Characterization and Modeling of Thoraco-Abdominal Response to Blast Waves
Volume 4. Biomechanical Model of Thorax Response to Blast Loading

12. PERSONAL AUTHOR(S)
C. J. Chuong and J.H. Stuhmiller

13a. TYPE OF REPORT	13b. TIME COVERED	14. DATE OF REPORT (Year, Month, Day)	15. PAGE COUNT
Annual/Final	FROM 2/15/82 TO 5/31/85	1985 May	125

16. SUPPLEMENTARY NOTATION
Annual covers time period of 15 February 1984 - 31 May 1985.
Annual/Final published in 8 volumes

17. COSATI CODES		
FIELD	GROUP	SUB-GROUP
06	21	
06	17	

18. SUBJECT TERMS (Continue on reverse if necessary and identify by block number)

19. ABSTRACT (Continue on reverse if necessary and identify by block number)

20. DISTRIBUTION / AVAILABILITY OF ABSTRACT ☐ UNCLASSIFIED/UNLIMITED ☒ SAME AS RPT. ☐ DTIC USERS	21. ABSTRACT SECURITY CLASSIFICATION Unclassified
22a. NAME OF RESPONSIBLE INDIVIDUAL Mary Frances Bostian	22b. TELEPHONE (Include Area Code) 301-663-7325 22c. OFFICE SYMBOL SGRD-RMI-S

DD Form 1473, JUN 86 *Previous editions are obsolete.* SECURITY CLASSIFICATION OF THIS PAGE

FOREWORD

This Annual/Final Report has eight volumes. The titles are as follows:

1. Project Summary
2. Blast Load Definition on a Torso Model
3. Lung Dynamics and Mechanical Properties Determination
4. Biomechanical Model of Thorax Response to Blast Loading
5. Experimental Investigation of Lung Injury Mechanism
6. Biomechanical Model of Lung Injury Mechanisms
7. Gastrointestinal Response to Blast
8. Effect of Clothing on Thoracic Response

CONTENTS

ILLUSTRATIONS

Page

TABLES

1. INTRODUCTION

1.1 OBJECTIVES

The objective of the Blast OverPressure (BOP) program is to understand the mechanisms by which biological organs are injured so that a Damage Risk Criteria (DRC) for humans can be defined in terms of blast parameters. In addition to the various experimental projects, mathematical models have been developed to understand the underlying mechanisms, correlate mechanical response and observed injury, and to provide a way to extrapolate animal experimental studies to the prediction of human exposure safety guidelines.

This report documents the construction of mathematical models to study animal response to external blast. Based on sheep anatomy a simplified 16-element three-dimensional model was constructed to capture the gross body response. A refined two-dimensional model was then constructed to follow wave propagation inside the thorax and to identify locations subjected to the greatest stress. Keywords: wounds and injuries; blast loads; blast waves

1.2 BACKGROUND

Extensive experiments of animal exposure to air and underwater blast waves have been carried out by the Lovelace Foundation of Albuquerque, New Mexico in the past 30 years [10, 15, 16, 17]. The study of blast effect on biological bodies has also been advanced by the Swedish group led by Clemedson and Jönsson [3, 4, 8, 18, 19].

In support of these experiments, Bowen et al. [15] in 1965 proposed a mechanical model of the lung for studies in blast biology. In this model the lung is considered to be an air-filled cavity with the chest and abdominal walls acting as pistons which move under the load of the blast wave and compress the air. Physically, the inertia, elasticity and damping effects from various organs and parts of the body are lumped into mass, spring, and dashpot representations. Calculated pressure in the air cavity represents the average pressure in the whole lung at any given time when the body is under blast

exposure. This idealized model, however, ignores the wave propagation characteristics inside the body thorax and its possible links to the resulting body injuries.

Clinical and experimental examination of blast injured lung, however, suggest wave dynamics may play an important role in causing damage. With the differences in wave speeds between the lung and the other organs [6], wave propagation is considered an important phenomenon in the body during blast exposure. Reflection and transmission of incident wave can be very different due to the mismatched impedance of the propagation media. For a given compression loading, spatial and temporal variations of the overpressure response at different regions of the lung are expected.

With this background, a finite element approach was taken in the work described in this report. With it we are able to see various wave propagation characteristics, e.g., focusing, reflection, inside the thorax. Different parts of the lung experience different wave loading histories depending on their geometry, location and neighboring organs. At the corresponding location where the esophageal pressures are taken, the ITP predictions have shown good agreement with experimental measurement. The constructed model is shown to be an effective approach toward better understanding of the blast biology.

1.3 GENERAL DESCRIPTION

Section 2 summarizes the basics of sheep anatomy. Section 3 outlines the mathematical basis and the formulation of the finite element method. Architecture of the computer code used for this program is documented. Procedures for exchanging data between the main finite element analysis program and graphics processor are also documented.

Section 4 describes a simplified three-dimensional model defined by 16 hexahedral elements representing internal organs. The muscle and rib cage are represented by lumped parameters which are coupled to the finite element equations. This model is used to reproduce global ITP response with qualitative agreement under low pressure (< 10 psi) loading range. This model is also used to study the influence of abdominal air on the ITP response. This application confirms the previous experimental observation of Zuckerman [14] and Clemedson et al. [2,3] that lung injuries are caused primarily by chest wall loading.

In Section 5, a two-dimensional model is constructed with refined spatial and temporal resolutions in order to study the wave propagation characteristics inside the thorax. Material parametric studies are carried out to identify the material parameters which are important in the body's ITP response to external blast wave. The model is then used to illustrate the spatial variation of lung overpressure histories when a sheep is exposed to external blast wave loadings. It suggests that the interpretation of measured esophageal pressure should be carefully justified as progressive wave propagation could result in different response histories at different parts of the lung and thereby different damages.

Following this the model is validated with experimental results from various loading cases, e.g., four single-peak, three double-peak, and ten cases from isoimpulse studies. Reasonably good agreement is obtained among comparisons made between the model ITP prediction and the experimental esophageal pressure measurement.

2. ANATOMICAL STRUCTURE OF SHEEP

Sheep are used as the primary experimental subjects in the BOP program. Various blast exposure experiments were planned in order to understand the biomechanical responses and the resulting injuries. Concurrently, a mathematical model of sheep torso was constructed to simulate the transient interaction of the animal and the blast wave. The model predictions of biomechanical responses can be validated by the experimental measurements, e.g., esophageal, intrathoracic pressures, chest wall displacement, acceleration histories. The combination of animal experiment and model simulation should identify the injury criterion and understand the injury mechanism. The modeling technique can then be used to extend the results to human and various loading conditions for the definition of a generalized safety guideline of blast exposure.

To model the response of a sheep torso under blast wave incidence, we first need to know its anatomical structure. We need to know the shape and the relative orientation of various organs to define the model geometry. We also need to know their basic mechanical properties to prescribe the structural rigidity and to determine the resulting mechanical stress under external loadings. Proper boundary conditions should be prescribed to represent the blast environment the animal encounters. With all this information together with appropriate engineering approximations, a finite element model can be constructed for the animal torso to predict its transient mechanical interaction with the blast overpressure wave loadings.

2.1 BASIC SHEEP ANATOMY

The details of the sheep torso anatomy are summarized in the following illustrations reproduced from References 7 and 9. Figure 2-1 is a side view of a sheep with superficial muscle layers while Figure 2-2 is a side view of a sheep skeleton. T_4, L_2, etc. are labeled on the figures to identify the locations where a cross sectional view is provided. T_4 and L_2, for example, mean the fourth thoracic vertebra and the second lumbar vertebra. Cross sectional views at T_4, T_7, and T_8 (Figs. 2-3, 2-4, and 2-5, respectively) show the size

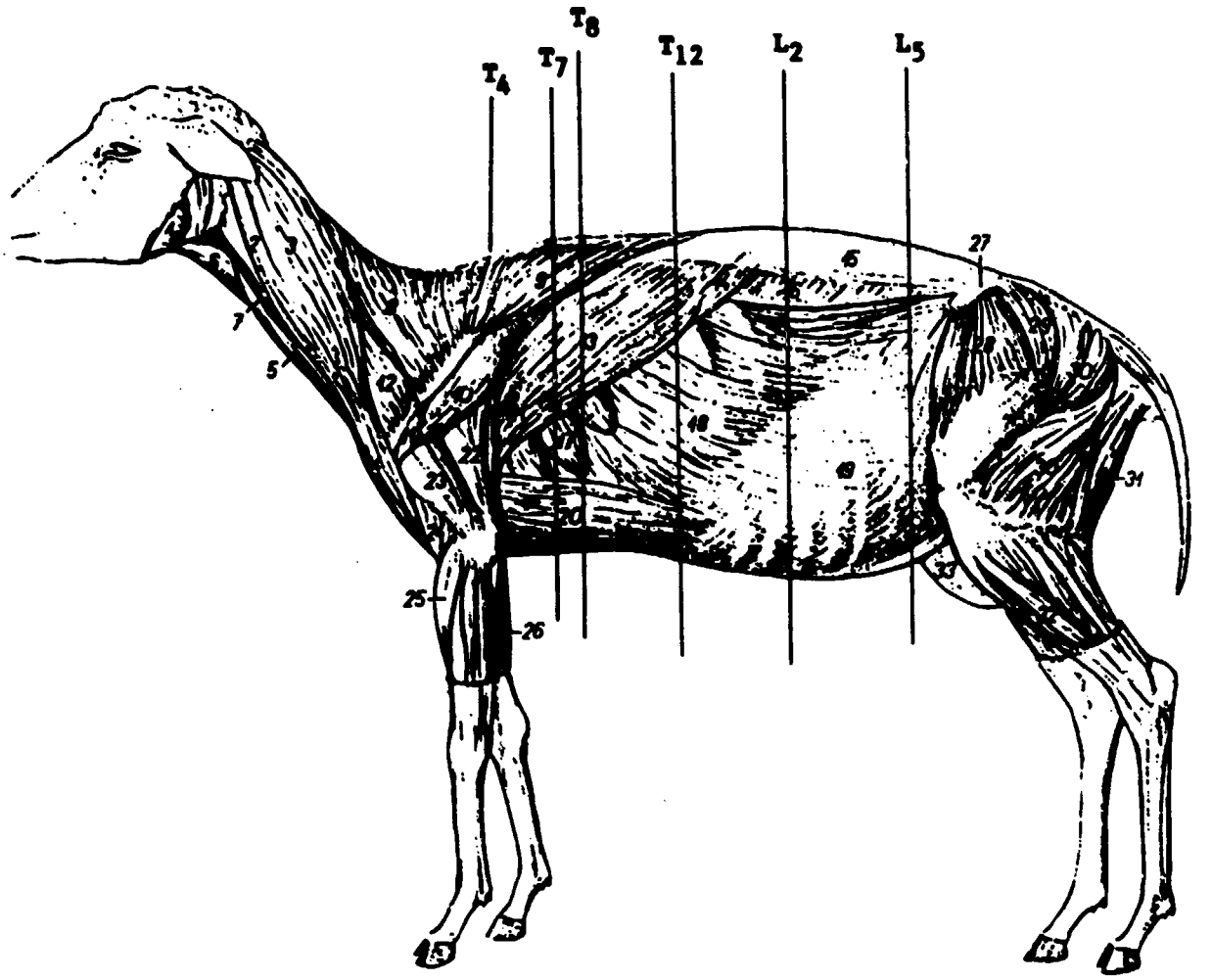

1. *m. masseter* — masseter muscle
2.–4. *m. brachiocephalicus* — brachiocephalic muscle
2. *m. cleidomastoideus* — cleidomastoid muscle
3. *m. cleidooccipitalis* — cleido-occipital muscle
4. *m. cleidobrachialis* — cleidobrachial muscle
5. *m. sternomastoideus (m. sternocephalicus)* — sternomastoid muscle (sternocephalic muscle)
6. *m. sternohyoideus et m. sternothyroideus* — sternohyoid and sternothyroid muscles
7. *vena jugularis* — jugular vein
8. *pars cervicalis mm. trapezii* — cervical part of trapezius muscle
9. *pars thoracica mm. trapezii* — thoracic part of trapezius muscle
10. *pars scapularis mm. deltoidei* — scapular part of deltoid muscle
11. *pars acromialis mm. deltoidei* — acromial part of deltoid muscle
12. *m. omotransversarius* — omotransverse muscle
13. *m. latissimus dorsi* — latissimus dorsi muscle
14. *m. serratus dorsalis caudalis* — caudal dorsal serratus muscle
15. *fascia thoracolumbalis* — thoracolumbar fascia
16. *m. obliquus internus abdominis* — internal oblique abdominal muscle
17. *m. serratus ventralis thoracis* — thoracic ventral serratus muscle
18. *m. obliquus externus abdominis* — external oblique abdominal muscle
19. *aponeurosis mm. obliqui abdominis externi et mm. obliqui abdominis interni* — aponeurosis of external and internal oblique abdominal muscles
20. *m. pectoralis profundus (m. pectoralis descendens)* — deep pectoral muscle (ascending pectoral muscle)
21. *m. tensor fasciae antebrachii* — tensor fasciae antebrachii muscle
22. *caput longum mm. tricipitis brachii* — long head of triceps brachii muscle
23. *caput laterale mm. tricipitis brachii* — lateral head of triceps brachii muscle
24. *m. brachialis* — brachial muscle
25. *m. extensor carpi radialis* — extensor carpi radialis muscle
26. *m. extensor carpi ulnaris* — extensor carpi ulnaris muscle
27. *tuber coxae* — tuber coxae
28. *m. tensor fasciae latae* — tensor fasciae latae muscle
29. *m. gluteus medius* — middle gluteal muscle
30., 30'. *m. glutobiceps* (30. *m. gluteus superficialis*, 30'. *m. biceps femoris*) — gluteobiceps muscle (30. superficial gluteal muscle, 30'. biceps femoris muscle)
31. *m. semitendinosus* — semitendinosus muscle
32. *m. peroneus longus* — peroneus longus muscle
33. *uber* — udder

Figure 2-1. Side view of superficial muscle layer of a sheep.

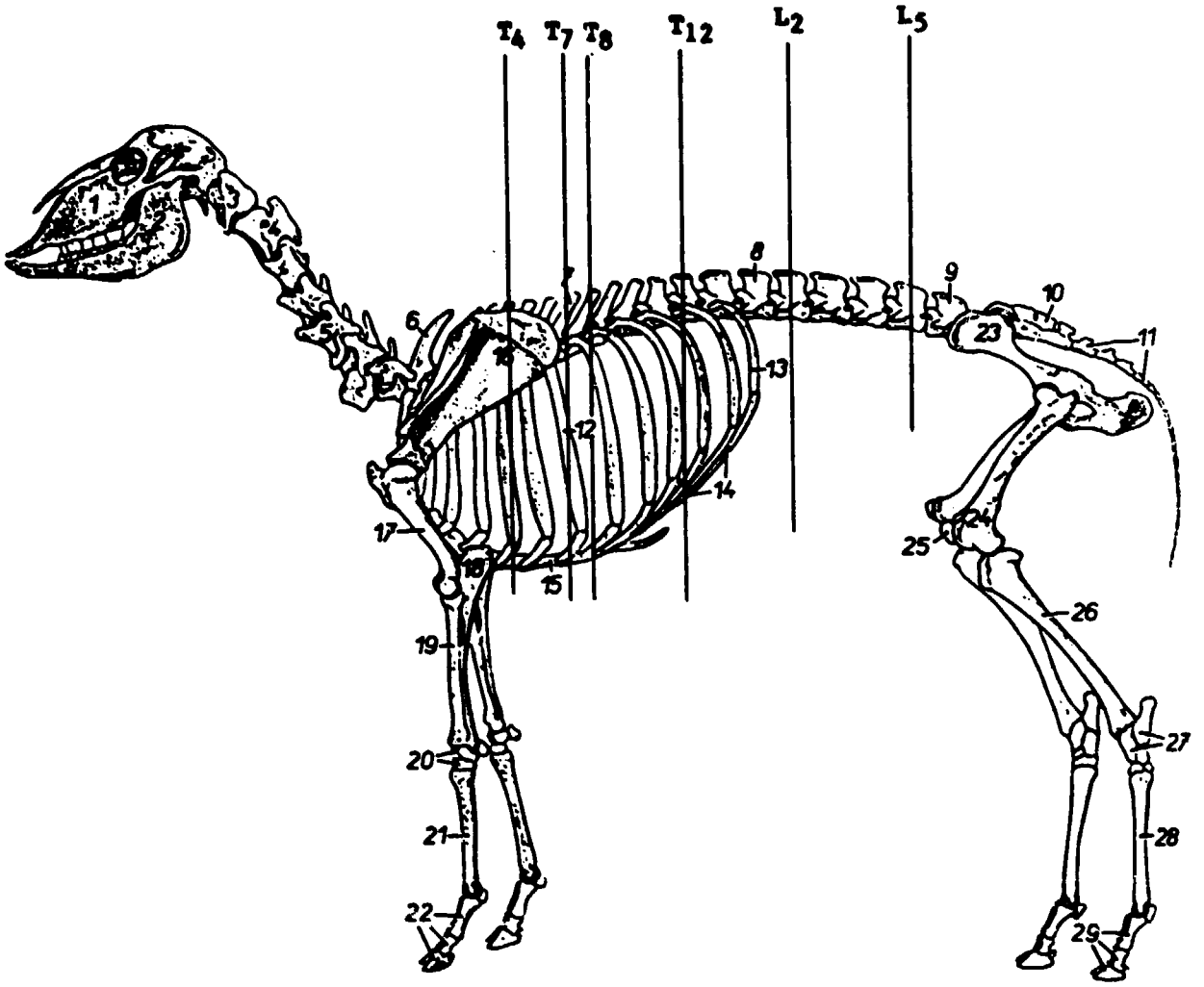

1. *maxilla* — maxilla
2. *mandibula* — mandible
3. *atlas* — atlas
4. *axis* — axis
5. *vertebra cervicalis V* — fifth cervical vertebra
6. *vertebra thoracica I* — first thoracic vertebra
7. *vertebra thoracica VII* — seventh thoracic vertebra
8. *vertebra lumbalis I* — first lumbar vertebra
9. *vertebra lumbalis VI* — sixth lumbar vertebra
10. *os sacrum* — sacrum
11. *vertebrae coccygeae* — coccygeal vertebrae
12. *costa VII* — seventh rib
13. *costa XIII* — thirteenth rib
14. *arcus costalis* — costal arch
15. *corpus sterni* — body of sternum
16. *scapula* — scapula
17. *humerus* — humerus
18. *ulna* — ulna
19. *radius* — radius
20. *ossa carpi* — carpal bones
21. *os metacarpale III et IV* — third and fourth metacarpal bone
22. *ossa digitorum manus* — phalanges of thoracic appendage
23. *os coxae* — os coxae
24. *os femoris* — femur
25. *patella* — patella
26. *tibia* — tibia
27. *ossa tarsi* — tarsal bones
28. *os metatarsale III et IV* — third and fourth metatarsal bone
29. *ossa digitorum pedis* — phalanges of pelvic appendage

Figure 2-2. Side view of a sheep skeleton.

and relative location of major organs in the thoracic cavity. At T_7 and T_8 the abdominal contents occupy most of space. At T_{12} (Fig. 2-6) we can see a small portion of the basal tip of the right lung. This gives us an idea of the domed shape of the diaphragm which contacts the lower boundary of the lungs. Cross sectional views at L_2 and L_5 (Figs. 2-7 and 2-8) show various abdominal contents at different levels.

Figure 2-9(a) shows the ventral view of an isolated sheep lung and heart. Enclosed in the ipsilateral pleural sac each lung is covered by the pulmonary pleura and is free to move in the sac. The right lung [Fig. 2-9(b)] is subdivided into four lobes by interlobar fissures, namely the apical, the middle, the diaphragmatic, and the accessory. The left lung [Fig. 2-9(c)] is divided by an interlobar fissure into two lobes, the apical and the diaphragmatic. Between the lungs is the mediastinum, soft tissue encasing the esophagus, trachea and aorta. From the cross sectional view at T_4 and T_7 we can see the esophagus close to the lung lobes. This is where the experimental esophageal pressure is taken.

Figure 2-10 shows the abdominal contents at superficial level looking from the right. Almost three-fourths of the abdominal cavity is occupied by the stomach. The stomach consists of four compartments: the rumen, reticulum, omasum, and abomasm. The remainder of the abdominal cavity is occupied by the spleen, liver, small intestine and large intestine.

The size of the stomach and GI tracts is significant in the sheep torso. It is known to trap large amounts of air under normal circumstances when compared with other species. Due to differences in compressibility between air and the surrounding tissues, the air has been suspected to be directly related to the cause of GI tissue damage after animal blast exposure. It has also been suspected of enhancing the possibility of lung injury due to its presence in the abdomen. A three-dimensional model is constructed to study this coupling effect in Section 4.

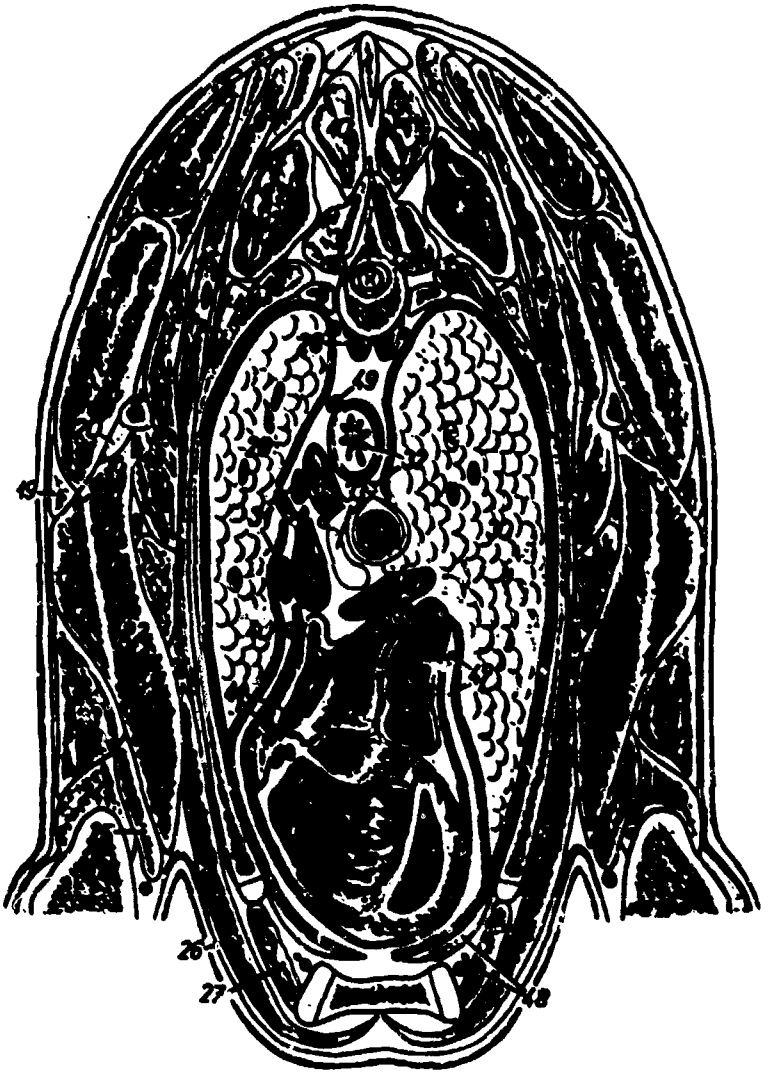

1. *processus spinosus vertebrae thoracicae III* – spinous process of third thoracic vertebra
2. *corpus vertebrae thoracicae IV* – body of fourth thoracic vertebra
3. *caput costae IV* – head of fourth rib
4. *scapula* – scapula
5. *costa IV* – fourth rib
6. *sternum* – sternum
7. *humerus* – humerus
8. *m. rhomboideus thoracis* – thoracic rhomboideus muscle
9. *m. serratus ventralis thoracis* – thoracic ventral serratus muscle
10. *m. spinalis et m. semispinalis thoracis et cervicis* – spinalis et semispinalis thoracis et cervicis muscle
11. *m. supraspinatus* – supraspinous muscle
12. *m. longissimus thoracis* – longissimus thoracis muscle
13. *m. multifidus thoracis* – multifidus thoracis muscle
14. *m. infraspinatus* – infraspinous muscle
15. *m. serratus dorsalis cranialis* – cranial dorsal serratus muscle
16. *mm. intercostales* – intercostal muscles
17. *m. iliocostalis thoracis* – thoracic iliocostal muscle
18. *m. subscapularis* – subscapular muscle
19. *m. deltoideus* – deltoid muscle
20. *m. teres minor* – teres minor muscle
21. *m. teres major* – teres major muscle
22. *caput longum m. tricipitis brachii* – long head of triceps brachii muscle
23. *caput laterale m. tricipitis brachii* – lateral head of triceps brachii muscle
24. *m. anconeus* – anconeus muscle
25. *caput mediale m. tricipitis brachii* – medial head of triceps brachii muscle
26. *m. pectoralis profundus (m. pectoralis accessorius)* – deep pectoral muscle (ascending pectoral muscle)
27. *m. intercostalis internus (m. intercartilagineus)* – internal intercostal muscle (intercartilaginous muscle)
28. *m. longus colli, truncus sympathicus* – longus colli muscle, sympathetic trunk
29. *lobus cranialis pulmonis sinistri* – cranial lobe of left lung
30. *lobus cranialis pulmonis dextri* – cranial lobe of right lung
31. *v. azygos sinistra* – left azygos vein
32. *oesophagus, n. vagus dexter* – esophagus, right vagus nerve
33. *n. vagus sinister, lnn. mediastinales medius* – left vagus nerve, middle mediastinal lymph node
34. *aorta* – aorta
35. *trachea* – trachea
36. *a. pulmonalis sinistra* – left pulmonary artery
37. *a. pulmonalis dextra* – right pulmonary artery
38. *vv. pulmonales* – pulmonary veins
39. *atrium sinistrum cordis* – left atrium of heart
40. *n. phrenicus sinister* – left phrenic nerve
41. *auricula atrii sinistri (auricula sinistra) cordis* – auricle of left atrium (left auricle) of heart
42. *ventriculus sinister* – left ventricle
43. *paries ventriculi sinistri* – left ventricular wall
44. *atrium dextrum cordis* – right atrium of heart
45. *ventriculus dexter* – right ventricle
46. *ostium v. cavae caudalis* – opening of caudal vena cava
47. *n. phrenicus dexter, pericardium* – right phrenic nerve, pericardium
48. *m. transversus thoracis, a. et v. thoracica interna* – transverse thoracic muscle, internal thoracic artery and vein
49. *ductus thoracicus* – thoracic duct

Figure 2-3. Cross-sectional view of a sheep at the fourth thoracic vertebra.

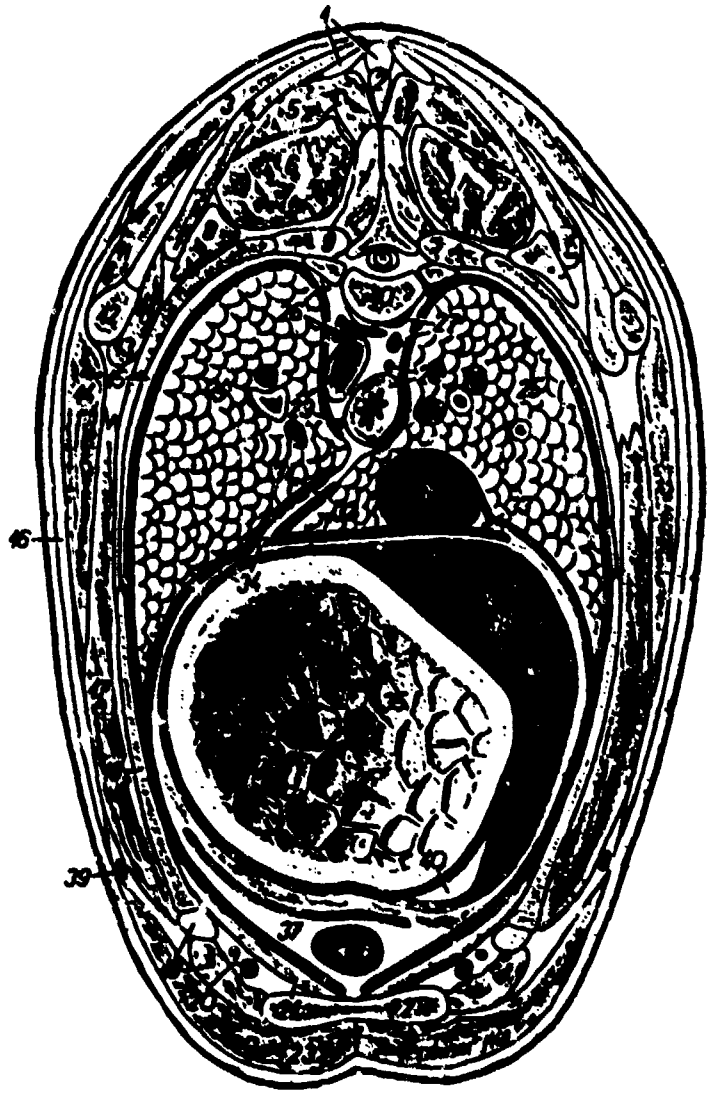

1. *lig. supraspinale et lig. nuchae* — supraspinal and nuchal ligaments
2. *processus spinosus vertebrae thoracicae VI* — spinous process of sixth thoracic vertebra
3. *m. trapezius (pars thoracica)* — trapezius muscle (thoracic part)
   rhomboideus thoracis — thoracic rhomboid muscle
4. *m. spinalis et semispinalis thoracis et cervicis* — spinalis et semispinalis thoracis et cervicis muscle
5. *m. longissimus thoracis* — longissimus thoracis muscle
6. *m. multifidus thoracis* — multifidus thoracis muscle
7. *m. iliocostalis thoracis* — thoracic iliocostal muscle
8. *m. levator costae* — levator muscle of rib
9. *vertebra thoracica VII* — seventh thoracic vertebra
10. *m. infraspinatus* — infraspinous muscle
11. *scapula* — scapula
12. *m. subscapularis* — subscapular muscle
13. *m. latissimus dorsi* — latissimus dorsi muscle
14. *mm. intercostales* — intercostal muscles
15. *m. cutaneus trunci* — cutaneous muscle of trunk
16. *m. serratus ventralis thoracis* — thoracic ventral serratus muscle
17. *costa VII* — seventh rib
18. *m. intercostalis internus (m. intercartilagineus), cartilago costalis VII* — internal intercostal muscle (intercartilaginous muscle), cartilage of seventh rib
19. *a. et v. thoracica interna* — internal thoracic artery and vein
20. *m. transversus thoracis* — transverse thoracic muscle
21. *sternum* — sternum
22. *m. pectoralis profundus (m. pectoralis descendens)* — deep pectoral muscle (descending pectoral muscle)
23. *lobus caudalis pulmonis sinistri* — caudal lobe of left lung
24. *lobus caudalis pulmonis dextri* — caudal lobe of right lung
25. *truncus sympathicus, v. azygos sinistra* — sympathetic trunk, left azygos vein
26. *m. longus colli, ductus thoracicus* — longus colli muscle, thoracic duct
27. *truncus vagalis dorsalis, oesophagus* — dorsal vagal trunk, oesophagus
28. *aorta, truncus vagalis ventralis* — aorta, ventral vagal trunk
29. *v. cava caudalis* — caudal vena cava
30. *mediastinum caudale* — caudal mediastinum
31. *lobus accessorius pulmonis* — accessory lobe of lung
32. *n. phrenicus dexter, pleura & mesodiaphragma* — right phrenic nerve, fold of caudal vena cava
33. *n. phrenicus sinister, oesophagus* — left phrenic nerve, diaphragm
34. *reticulum* — reticulum
35. *hepar* — liver
36. *pericardium* — pericardium
37. *apex cordis* — apex of heart
38. *v. thoracica externa* — external thoracic vein
39. *omentum minus (lig. hepatogastricum)* — lesser omentum (hepatogastric ligament)

Figure 2-4. Cross-sectional view of a sheep at the seventh thoracic vertebra.

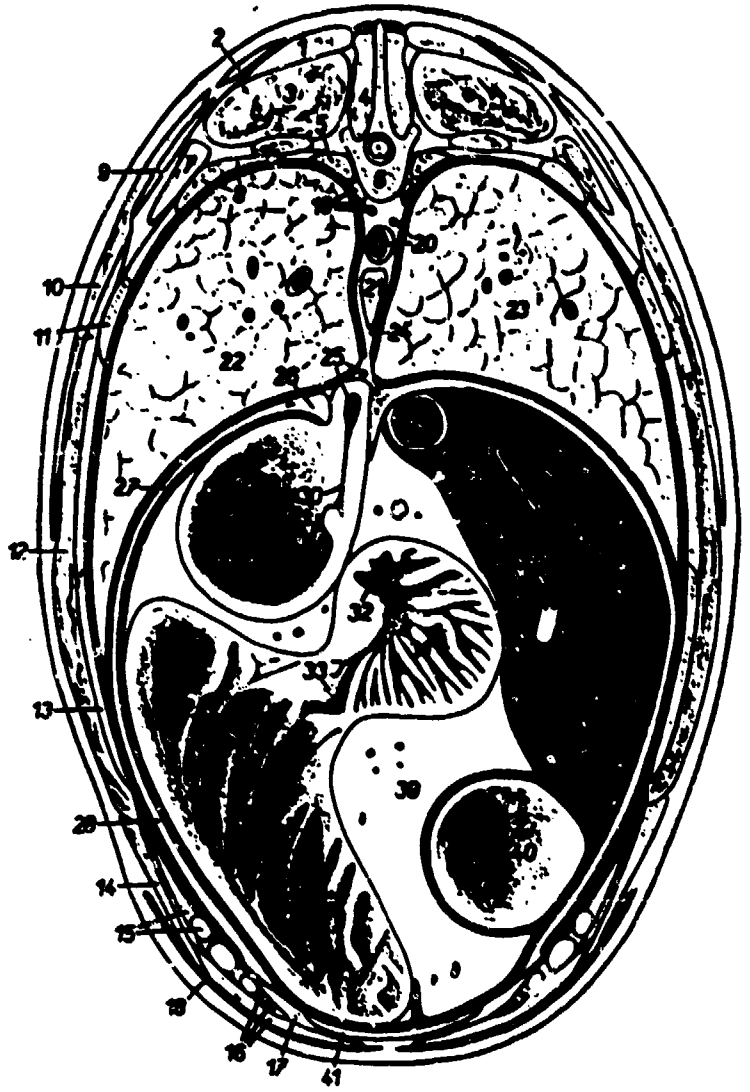

1. *m. spinalis et semispinalis thoracis et cervicis* – spinalis et semispinalis thoracis et cervicis muscle
2. *pars thoracica m. trapezii* – thoracic part of trapezius muscle
3. *m. longissimus thoracis* – longissimus thoracis muscle
4. *m. multifidus thoracis* – multifidus thoracis muscle
5. *costa VIII, m. levator costae* – eighth rib, levator muscle of rib
6. *vertebra thoracica VIII* – eighth thoracic vertebra
7. *m. iliocostalis thoracis* – thoracic iliocostal muscle
8. *costa IX, mm. intercostales* – ninth rib, intercostal muscles
9. *cartilago scapulae* – cartilage of scapula
10. *m. latissimus dorsi* – latissimus dorsi muscle
11. *costa X* – tenth rib
12. *m. serratus ventralis thoracis* – thoracic ventralis serratus muscle
13. *costa XI* – eleventh rib
14. *m. obliquus externus abdominis* – external oblique abdominal muscle
15. *mm. intercostales, cartilago costalis XI* – intercostal muscles, eleventh costal cartilage
16. *a. et v. thoracica interna, m. rectus abdominis* – internal thoracic artery and vein, straight abdominal muscle
17. *m. transversus abdominis* – transverse abdominal muscle
18. *m. pectoralis profundus (m. pectoralis descendens)* – deep pectoral muscle (descending pectoral muscle)
19. *m. psoas minor, truncus sympathicus, v. azygos sinistra* – psoas minor muscle, sympathetic trunk, left azygos vein
20. *aorta, ductus thoracicus* – aorta, thoracic duct
21. *lnn. mediastinales caudales* – caudal mediastinal lymph node
22. *pulmo sinister* – left lung
23. *pulmo dexter* – right lung
24. *mediastinum caudale* – caudal mediastinum
25. *truncus vagalis dorsalis, oesophagus* – dorsal vagal trunk, oesophagus
26. *crus mediale sinistrum diaphragmatis* – left medial crus of diaphragm
27. *centrum tendineum diaphragmatis* – central tendon of diaphragm
28. *pars costalis diaphragmatis* – costal part of diaphragm
29. *atrium ruminoreticuli* – atrium of ruminoreticulum
30. *sulcus reticuli* – reticular sulcus
31. *omasum* – omasum
32. *ostium reticulo-omasicum* – reticulo-omasal opening
33. *ostium omphalomesaraicum* – omasal opening
34. *v. cava caudalis* – caudal vena cava
35. *abomasum* – abomasum
36. *v. hepatica* – hepatic vein
37. *hepar* – liver
38. *ramus v. portae, ductus hepaticus* – branch of portal vein, hepatic duct
39. *omentum minus* – lesser omentum
40. *vesica fellea* – gallbladder
41. *cartilago xiphoidea* – xiphoid cartilage

Figure 2-5. Cross-sectional view of a sheep at the eighth thoracic vertebra.

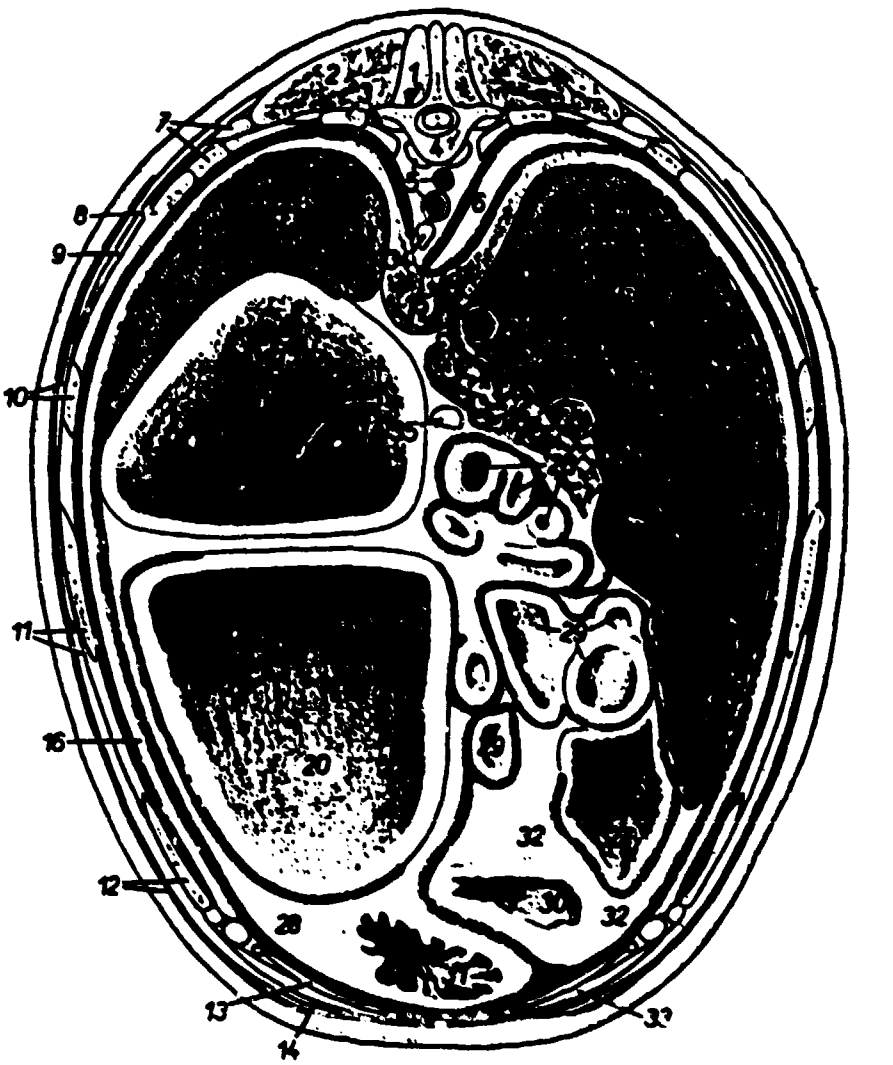

- ... *multifidus thoracis* – multifidus thoracis muscle
- 2. *m. longissimus thoracis* – longissimus thoracis muscle
- 3. *costa XII, m. psoas major* – twelfth rib, psoas major muscle
- 4. *vertebra thoracica XII* – twelfth thoracic vertebra
- 5. *m. psoas minor, v. azygos sinistra, aorta* – psoas minor muscle, left azygos vein, aorta
- 6. *pulmo dexter* – right lung
- 7. *m. iliocostalis thoracis, costa XI* – thoracic iliocostal muscle, eleventh rib
- 8. *m. intercostales* – intercostal muscles
- 9. *m. serratus dorsalis caudalis* – caudal dorsal serratus muscle
- 10. *m. latissimus dorsi, costa X* – latissimus dorsi muscle, tenth rib
- 11. *costa IX, m. obliquus externus abdominis* – ninth rib, external oblique abdominal muscle
- 12. *costa VIII, m. cutaneus trunci* – eighth rib, cutaneous muscle of trunk
- 13. *m. transversus abdominis* – transverse abdominal muscle
- 14. *m. pectoralis profundus (m. pectoralis antebrachii)* – deep pectoral muscle (ascending pectoral muscle)
- 15. *crura diaphragmatis* – diaphragmatic crura
- 16. *pars costalis diaphragmatis* – costal part of diaphragm
- 17. *lien* – spleen
- 18. *hepar* – liver
- 19. *saccus dorsalis ruminis* – dorsal ruminal sac
- 20. *saccus ventralis ruminis* – ventral ruminal sac
- 21. *v. cava caudalis* – caudal vena cava
- 22. *v. portae* – portal vein
- 23. *ductus hepaticus* – hepatic duct
- 24. *foramen epiploicum* – epiploic foramen
- 25. *pancreas* – pancreas
- 26. *ansa sigmoidea partis ascendentis duodeni* – sigmoid ansa of cranial part of duodenum
- 27. *vesica fellea* – gallbladder
- 28. *omentum majus* – greater omentum
- 29. *jejunum* – jejunum
- 30. *pars pylorica abomasi* – pyloric part of abomasum
- 31. *abomasum* – abomasum
- 32. *omentum minus* – lesser omentum
- 33. *m. rectus abdominis* – straight abdominal muscle
- 34. *lnn. mediastinales caudales* – caudal mediastinal lymph node
- 35. *lnn. pancreaticoduodenales* – pancreaticoduodenal lymph node

Figure 2-6. Cross-sectional view of a sheep at the twelfth thoracic vertebra.

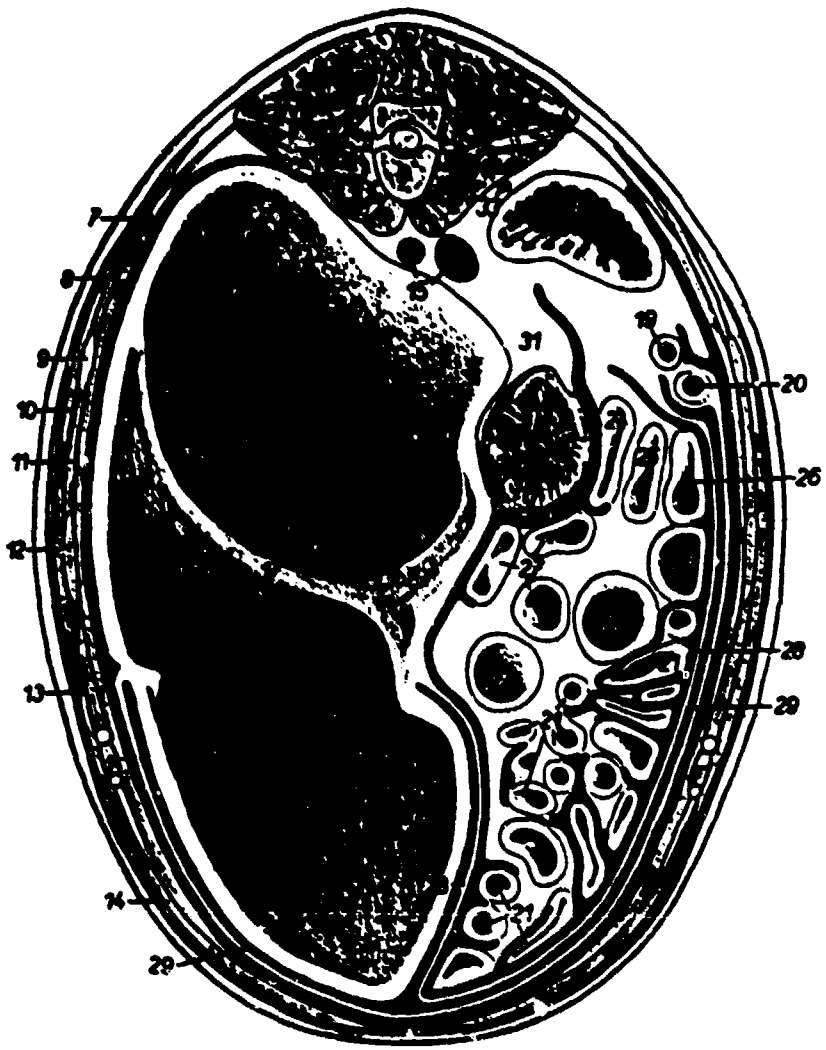

1. *m. longissimus lumborum* – longissimus lumborum muscle
2. *m. multifidus lumborum* – multifidus lumborum muscle
3. *processus transversus vertebrae lumbalis II, m. quadratus lumborum* – transverse process of second lumbar vertebra, quadratus lumborum muscle
4. *m. psoas major* – psoas major muscle
5. *vertebra lumbalis II* – second lumbar vertebra
6. *m. psoas minor* – psoas minor muscle
7. *m. transversus abdominis* – transverse abdominal muscle
8. *m. obliquus internus abdominis* – internal oblique abdominal muscle
9. *costa XIII* – thirteenth rib
10. *m. obliquus externus abdominis* – external oblique abdominal muscle
11. *mm. intercostales* – intercostal muscles
12. *costa XII* – twelfth rib
13. *m. cutaneus trunci* – cutaneous muscle of trunk
14. *m. rectus abdominis* – straight abdominal muscle
15. *aorta, v. cava caudalis* – aorta, caudal vena cava
16. *saccus dorsalis ruminis* – dorsal ruminal sac
17. *pilar cranialis ruminis* – cranial pillar of rumen
18. *saccus ventralis ruminis* – ventral rumi... ...c
19. *pars descendens duodeni* – ascending part of duodenum
20. *pars descendens duodeni* – descending part of duodenum
21. *jejunum* – jejunum
22. *cecum* – cecum
23.–27. *colon descendens* – ascending colon
23. *ansa proximalis (gyrus ventralis) coli* – proximal ansa (middle gyrus) of colon
24. *ansa proximalis (gyrus dorsalis) coli* – proximal ansa (dorsal gyrus) of colon
25. *ansa distalis coli (gyrus dorsalis)* – dist... ...sa of colon (dorsal gyrus)
26. *ansa distalis coli (gyrus ventralis)* – dist... ...sa of colon (ventral gyrus)
27. *ansa spiralis coli* – spiral ansa of colon
28. *pars profunda omenti majoris* – deep layer of greater omentum
29. *pars superficialis omenti majoris* – superficial layer of greater omentum
30. *colon descendens* – descending colon
31. *lig. suspensorium renis* – suspensory ligament of kidney
32. *ren sinister* – left kidney
33. *ureter dexter* – right ureter

Figure 2-7. Cross-sectional view of a sheep at the second lumbar vertebra.

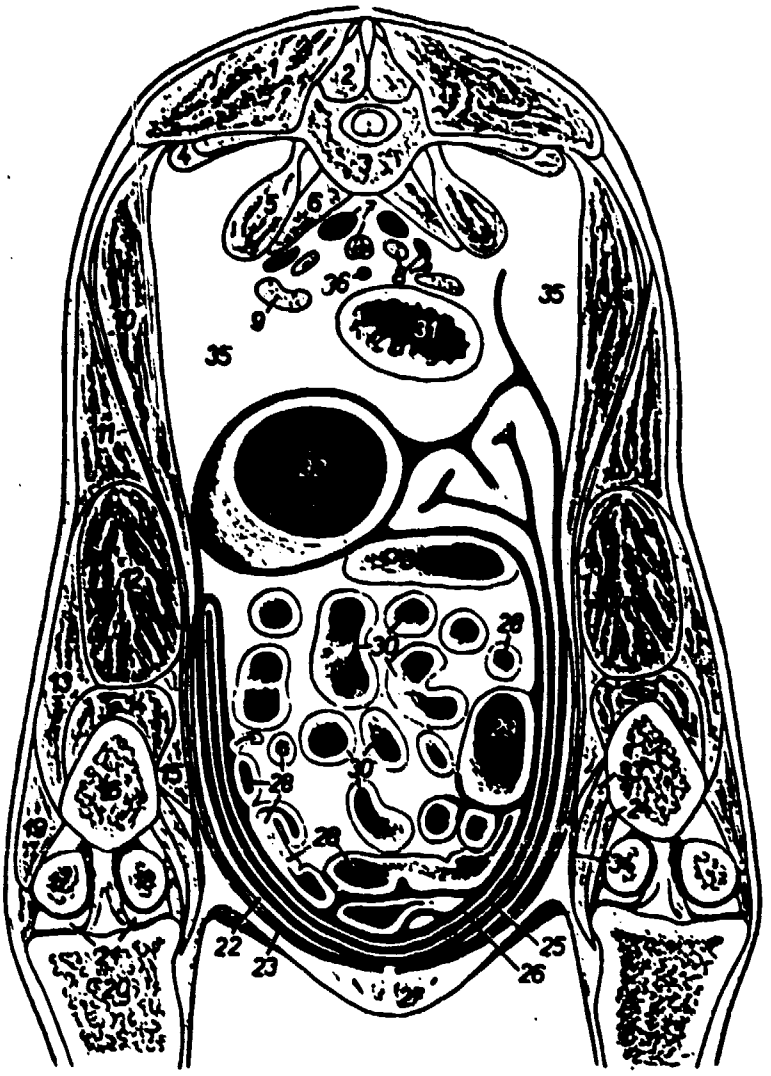

1. *m. longissimus lumborum* – longissimus lumborum muscle
2. *m. multifidus lumborum* – multifidus lumborum muscle
3. *vertebra lumbalis V* – fifth lumbar vertebra
4. *m. quadratus lumborum* – quadratus lumborum muscle
5. *m. psoas major* – psoas major muscle
6. *m. psoas minor* – psoas minor muscle
7. *a. et v. iliaca interna* – internal iliac artery and vein
8. *a. et v. iliaca externa, ureter dexter* – external iliac artery and vein, right ureter
9. *ln. iliacus mediali* – middle iliac lymph node
10. *m. obliquus internus abdominis* – internal oblique abdominal muscle
11. *m. tensor fasciae latae* – tensor fasciae latae muscle
12. *m. quadriceps femoris* – quadriceps femoris muscle
13. *m. rectus femoris* – straight femoral muscle
14. *m. vastus lateralis* – lateral vastus muscle
15. *m. vastus intermedius* – intermediate vastus muscle
16. *m. vastus medialis* – medial vastus muscle
17. *femur* – femur
18. *condylus lateralis ossis femoris* – lateral condyle of femur
19. *condylus medialis ossis femoris* – medial condyle of femur
20. *m. biceps femoris* – biceps femoris muscle
21. *tibia* – tibia
22. *musculi* – menisci
23. *m. rectus abdominis* – straight abdominal muscle
24. *m. obliquus externus abdominis* – external oblique abdominal muscle
25. *m. adductor* – adductor muscle
26. *pars superficialis omenti majoris* – superficial layer of greater omentum
27. *pars profundus omenti majoris* – deep layer of greater omentum
28. *uber* – udder
29. *jejunum* – jejunum
30. *caecum* – cecum
31. *ansa spiralis coli* – spiral ansa of colon
32. *rectum* – rectum
33. *saccus caecus caudodorsalis rumenis* – caudodorsal blind sac of rumen
34. *m. gracilis* – gracilis muscle
35. *m. sartorius* – sartorius muscle
36. *corpus adiposum* – adipose body
37. *ureter sinister* – left ureter

Figure 2-8. Cross-sectional view of a sheep at the fifth lumbar vertebra.

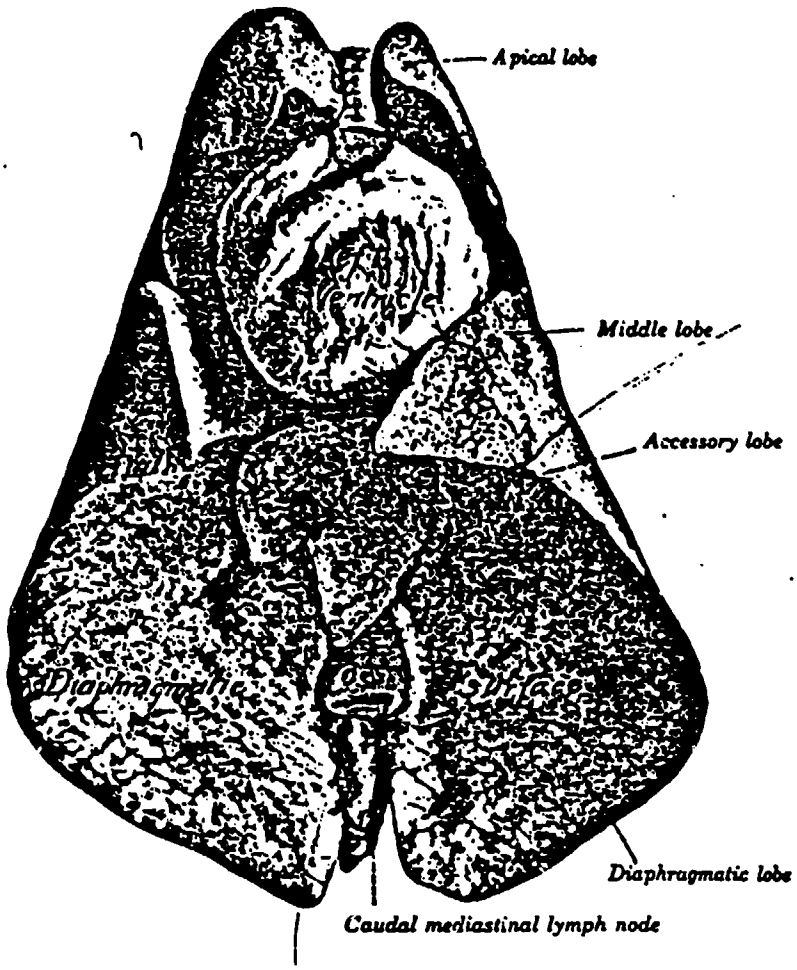

(a) Ventral view of lungs and heart (from Ref. 1, Fig. 30-22)

Figure 2-9. Lungs and heart of sheep.

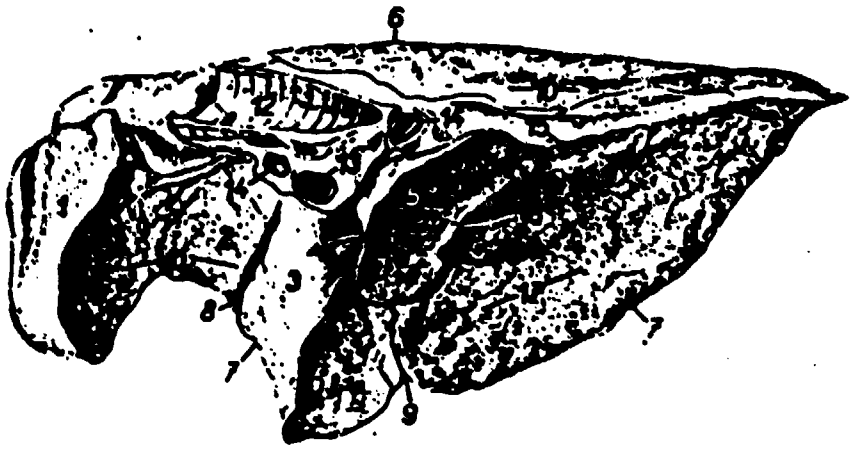

1. *pars cranialis lobi cranialis* – cranial part of cranial lobe
2. *pars caudalis lobi cranialis* – caudal part of cranial lobe
3. *lobus medius* – middle lobe
4. *lobus caudalis* – caudal lobe
5. *lobus accessorius* – accessory lobe
6. *margo dorsalis (obtusus)* – dorsal margin (obtuse)
7. *margo acutus ventralis* – ventral acute margin
8. *fissura interlobaris cranialis* – cranial interlobar fissure
9. *fissura interlobaris caudalis* – caudal interlobar fissure
10. *impressio aortica* – aortic impression
11. *impressio cardiaca* – cardiac impression
12. *trachea* – trachea
13. *a. pulmonalis dextra* – right pulmonary artery
14. *vv. pulmonales* – pulmonary veins
15. *insertio pleurae mediastinalis* – insertion of mediastinal pleura
16. *sulcus v. cavae caudalis* – sulcus for caudal vena cava
17. *facies diaphragmatica* – diaphragmatic surface
18. *bronchus trachealis* – tracheal bronchus

(b) Right lung (from Ref. 2, Vol. 2, Fig. 68).

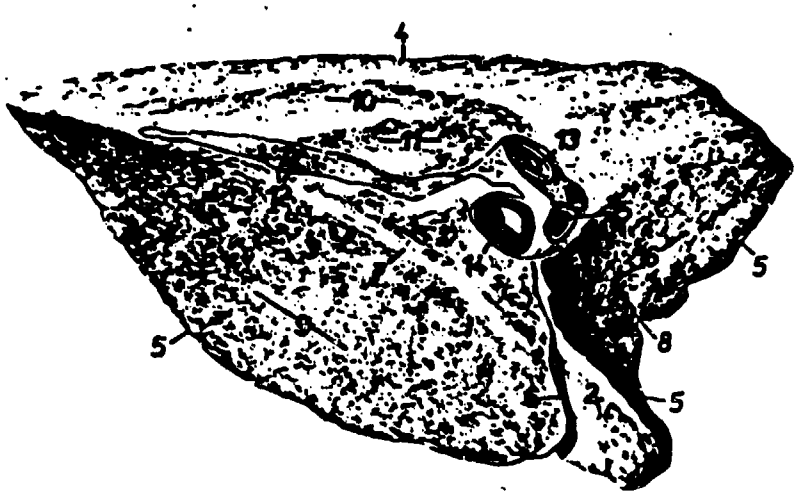

1. *pars cranialis lobi cranialis* – cranial part of cranial lobe
2. *pars caudalis lobi cranialis* – caudal part of cranial lobe
3. *lobus caudalis* – caudal lobe
4. *margo dorsalis (obtusus)* – dorsal margin (obtuse)
5. *margo acutus ventralis* – ventral acute margin
6. *fissura interlobaris (caudalis)* – interlobar fissure (caudal)
7. *margo acutus basalis* – basal acute margin
8. *incisura cardiaca* – cardiac notch
9. *facies diaphragmatica* – diaphragmatic surface
10. *impressio aortica* – aortic impression
11. *impressio oesophagea* – esophageal impression
12. *insertio pleurae mediastinalis* – insertion of mediastinal pleura
13. *bronchus principalis sinister* – left main bronchus
14. *vv. pulmonales* – pulmonary veins
15. *a. pulmonalis sinistra* – left pulmonary artery
16. *impressio cardiaca* – cardiac impression

(c) Left lung (from Ref. 2, Vol. 2, Fig. 67).

Figure 2-9. (Cont'd)

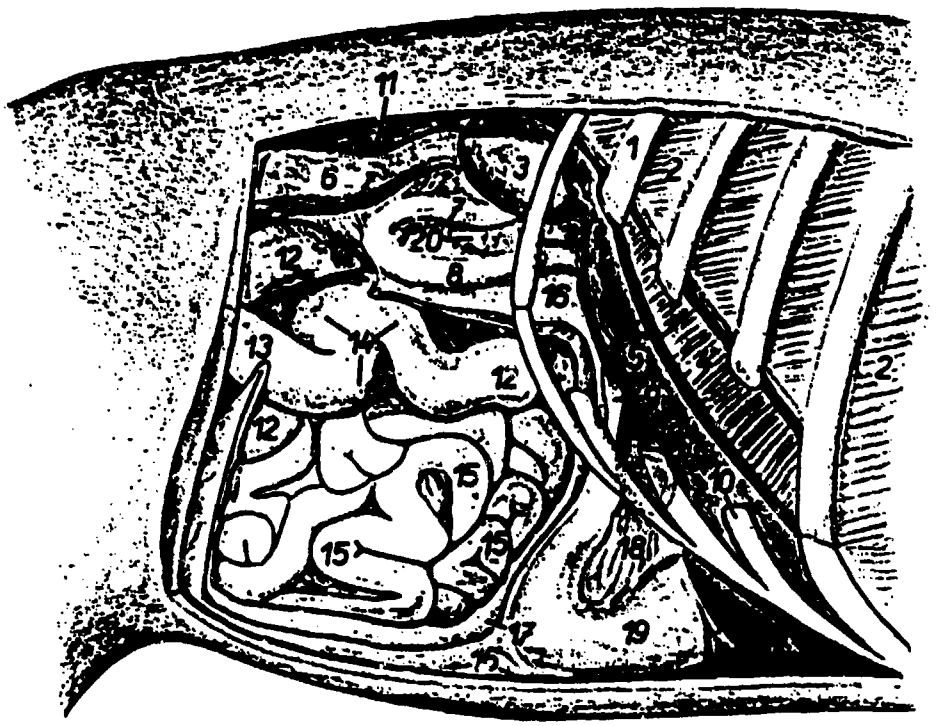

1. *costa XII* — twelfth rib
2. *mm. intercostales* — intercostal muscles
3. *ren dexter* — right kidney
4. *pars costalis diaphragmatis* — costal part of diaphragm
5. *hepar* — liver
6. *colon descendens* — descending colon
7. *pars ascendens duodeni* — ascending part of duodenum
8. *pars descendens duodeni* — descending part of duodenum
9. *pars cranialis duodeni, vesica fellea* — cranial part of duodenum, gallbladder
10. *cartilago costalis X* — tenth costal cartilage
11. *ureter dexter* — right ureter
12. *ansa spiralis coli* — spiral ansa of colon
13. *cecum* — cecum
14. *ansa proximalis coli* — proximal ansa of colon
15. *jejunum* — jejunum
16. *pars superficialis omenti majoris* — superficial layer of greater omentum
17. *pars profundus omenti majoris* — deep layer of greater omentum
18. *omentum minus* — lesser omentum
19. *abomasum* — abomasum
20. *pancreas* — pancreas

Figure 2-10. The abdominal contents at superficial level looking from the right.

3. FINITE ELEMENT COMPUTER PROGRAM

3.1 MATHEMATICAL BASIS AND THE FORMULATION OF FINITE ELEMENT METHOD

3.1.1 Introduction

Finite element method (FEM) is used to construct a mathematical model of the animal body and to study its structural response under external blast overpressure. The idea of FEM is to divide a continuous body into a number of elements of finite size. The original continuous body is replaced by the assembly of these elements. The continuous physical quantities are then approximated by functions which are smooth in each element, but are continuous and only piecewise smooth in the whole body assembly. The governing differential equation is solved in a "weak form" in that it is satisfied in a weighted average sense. The choice of approximations is, therefore, a key to the FEM. Basically, we approximate the physical quantities in terms of nodal unknown parameters through spatial interpolation function. Instead of the original differential equations we then have a set of algebraic equations in generalized coordinates defined at nodal points. The distribution in an element is obtained through interpolation.

There is a wide variety of approaches to FEM discretization depending on the variational statement or weight residual method [13]. Here a compatible displacement model based on the principle of virtual work is used. The principle of virtual work states that for a body of volume V bounded by surface A the virtual work done by the external body force F_i, inertial force $\rho_o \ddot{u}_i$ and surface traction force $\overset{\nu}{T}_i$ can be written at any instant of time as:

$$\int_V \sigma_{ij} \delta\varepsilon_{ij} \, dV = \int_V (F_i - \rho_o \ddot{u}_i) \delta u_i \, dV + \int_{A_T} \overset{\nu}{T}_i \, \delta u_i \, dA \quad , \tag{1}$$

where σ_{ij} and ε_{ij} denote the Cauchy stress and small strain tensors and A_T denotes the portion of the boundary surface where traction is prescribed.

The immediate step is to find displacement function u_i such that $u_i = \bar{u}_i$ on A_u (displacement or Dirichlet type boundary conditions) and Eq. (1) is satisfied for all admissible virtual displacement δu_i. If the choice of u_i is

sufficiently smooth the solution to Eq. (1) could well be exactly that to its original differential form of equation of motion. One important merit with FEM lies in that it requires the choice of u_i only to make Eq. (1) integrable. In other words, requirements on the choice of admissible function u_i is not so rigid as to satisfy the original differential equation exactly but only need to satisfy it in a sense of weighted average. This way we gain flexibility in coping with irregular geometry and boundary conditions. A sparse and symmetrically banded matrix equation is formed to be solved for nodal displacement at each time step. The body configuration is updated for the incremental solution at each time increment before marching to the next time step.

3.1.2 Spatial Discretization

The finite element discretization is done by first dividing the whole body into a finite number of sub-domains, each called an element. For a general continuum model nodal displacements are chosen to be the primary unknown to solve for. For a 3D model each node is assigned with three degrees of freedom. By looking at the variational statement, Eq. (1), a C_0 continuous type interpolation function will be sufficient to represent the displacement field in each element. We, therefore, write

$$u_i(x,y,z) = \sum_{a=1}^{ND} N^a(x,y,z)\ U_i^a \tag{2}$$

for each element where $N^a(x,y,z)$ is the element interpolation function associated with node a and U_i^a is the i^{th} component of nodal displacement at node a. Note the summation in Eq. (2) is to be carried up to the total nodal number ND associated with an element.

In our application we shall construct both 3D and 2D models for different purposes. In the 3D model, eight node brick elements are used with trilinear interpolation functions. In the 2D model, 4-node quadrilateral elements are used with bilinear interpolation functions. Isoparametric formulation is used in the formulations:

$$x_i(x,y,z) = \sum_{a=1}^{ND} N^a(x,y,z)\ X_i^a \tag{3}$$

With substitution of Eqs. (2) and (3) into Eq. (1), we yield:

$$\sum_{e=1}^{E} \left(M_{ij}^{ab} \ddot{U}_i + K_j^b - R_j^b \right) = 0 \tag{4}$$

where

$$M_{ij}^{ab} = \int_{V^e} \rho_o N^a N^b \, dV \, \delta_{ij} \tag{5}$$

is the consistent mass matrix;

$$K_j^b = \int_{V^e} \sigma_{ij} \, N_{,i}^b \, dV \tag{6}$$

is the internal force vector; and

$$R_j^b = \int_{A_T^e} \overset{\nu}{T}_j \, N^b \, dA + \int_{V^e} \rho_o \, F_j \, N^b \, dV \tag{7}$$

is the generalized force vector. The first term in Eq. (4), with $\ddot{U}_i$ denoting nodal acceleration, is the inertial force. The second term, the internal force vector, accounting for the force due to elasticity, can further be written as the sum of contributions from incremental stress and initial stress. The last term, or generalized force vector, specifies the generalized nodal force due to prescribed body force and surface tractions. Note that M_{ij}^{ab}, K_j^b, and R_j^b are the corresponding matrices or vector in element level. The integration is carried at element level with V^e and A^e denoting element volume and surface area, respectively. The global form of discretized equation of motion is obtained through assembly of contributions from all elements. The assembly procedure is symbolically written in terms of summation through total number of element E.

At a given time, once the global equation of motion [Eq. (4)] is assembled, it is then modified for non-zero Dirichlet boundary conditions and/or general mixed type boundary conditions. Note that Neumann type boundary condition enters the problem by dictating the variational statement, Eq. (1).

3.1.3 Temporal Discretization

We next have to do temporal discretization of Eq. (4) since it involves time differentiation. A direct integration scheme based on Newmark approximation is used:

$$\mathbf{U}_{n+1} = \mathbf{U}_n + \Delta t\, \dot{\mathbf{U}}_n + \Delta t^2 \left[\left(\frac{1}{2} - \beta\right) \ddot{\mathbf{U}}_n + \beta\, \ddot{\mathbf{U}}_{n+1}\right] \tag{8}$$

$$\dot{\mathbf{U}}_{n+1} = \dot{\mathbf{U}}_n + \Delta t \left[(1 - \gamma)\, \ddot{\mathbf{U}}_n + \gamma\, \ddot{\mathbf{U}}_{n+1}\right] \tag{9}$$

in which the subscripts denote variables at t_{n+1} and t_n, respectively, and $\Delta t = t_{n+1} - t_n$. $\dot{\mathbf{U}}$ and $\ddot{\mathbf{U}}$ are nodal velocity and acceleration, respectively. β and γ are parameters that control numerical damping and stability. For linear problem $\gamma = 1/2$ produces no numerical damping. By choosing $2\beta \geq \gamma \geq 1/2$ unconditional stability is achieved regardless of the size of time step Δt.

At time t_{n+1} we can rewrite the glogal form of generalized equation of motion in matrix notation as:

$$\mathbf{M}\, \ddot{\mathbf{U}}_{n+1} + \mathbf{K}(\mathbf{U}_{n+1}) = \mathbf{R}_{n+1} \tag{10}$$

Substitution of Eqs. (8) and (9) into (10) yields

$$\frac{\mathbf{M}}{\beta \Delta t^2} \mathbf{U}_{n+1} + \mathbf{K}(\mathbf{U}_{n+1}) = \mathbf{R}_{n+1} + \mathbf{A}_n$$

$$= \mathbf{R}_{n+1} + \frac{\mathbf{M}}{\beta \Delta t^2} \left\{\mathbf{U}_n + \Delta t\, \dot{\mathbf{U}}_n + \left(\frac{1}{2} - \beta\right) \Delta t^2\, \ddot{\mathbf{U}}_n\right\} \quad . \tag{11}$$

To solve Eq. (11) for $\mathbf{U}_{n+1}$ we can first rewrite it in a different form,

$$\mathbf{F}(\mathbf{U}_{n+1}) = 0 \quad . \tag{12}$$

The question is then to find solution $\mathbf{U}_{n+1}$ such that Eq. (12) is satisfied within specified error tolerance. We may write Taylor expansion of $\mathbf{F}$ about $\mathbf{U}^o_{n+1}$ where $\mathbf{U}^o_{n+1}$ denotes an initial test point:

$$F(U^{o}_{n+1} + \Delta U_{n+1}) = F(U^{o}_{n+1}) + DF(U^{o}_{n+1}) \cdot \Delta U_{n+1} + (\text{high order terms}) \quad .$$

$$= 0 \quad . \tag{13}$$

with D denoting Frechet derivative operator. Iteration formula can be obtained with linearization of Eq. (13):

$$DF(U^{j}_{n+1}) \cdot \Delta U^{j}_{n+1} = - F(U^{j}_{n+1}) \tag{14}$$

and

$$U^{j+1}_{n+1} = U^{j}_{n+1} + \Delta U^{j}_{n+1} \quad . \tag{15}$$

For a general nonlinear form of Eq. (12), iteration is repeated until ΔU^{j}_{n+1} is smaller than certain specified error tolerance.

Following these steps Eq. (11) is to be solved from

$$\left\{ DK(U^{j}_{n+1}) + \frac{M}{\beta \Delta t^{2}} \right\} \cdot \Delta U^{j}_{n+1} = \{ R_{n+1} - K(U^{j}_{n+1}) - M\ddot{U}^{j}_{n+1} \} \tag{16}$$

and

$$U^{j+1}_{n+1} = U^{j}_{n+1} + \Delta U^{j}_{n+1} \tag{17}$$

Equation (16) can be rewritten as

$$\hat{K}^{j}_{n+1} \cdot \Delta U^{j}_{n+1} = \hat{R}^{j}_{n+1} \tag{18}$$

with $\hat{K}$ and $\hat{R}$ denoting effective stiffness matrix and effective load vector, respectively.

3.1.4 Material Description

In our application the materials of various organs are assumed to be isotropic, linear viscoelastic. The constitutive relationship is written as:

$$\sigma_{ij}(t) = \int_{-\infty}^{t} \delta_{ij} \left[K(t - \tau) - \frac{2}{3} G(t - \tau) \right] d\varepsilon_{kk} + 2 \int_{-\infty}^{t} G(t - \tau)\, d\varepsilon_{ij} \tag{19}$$

where σ_{ij} and ε_{ij} denote Cauchy stress and small strain tensors, K, G are bulk and shear relaxation moduli, respectively, and δ_{ij} is the Kronecker delta function. If we further assume that the body is completely undisturbed prior to time 0 we can rewrite Eq. (19) as

$$\sigma_{ij}(t) = \sigma^{o}_{ij}(t) + \int_0^t \delta_{ij}\left[K(t-\tau) - \frac{2}{3}G(t-\tau)\right] d\varepsilon_{kk} + 2\int_0^t G(t-\tau)\, d\varepsilon_{ij} \qquad (20)$$

where

$$\sigma^{o}_{ij}(t) = \delta_{ij}\left[K(t) - \frac{2}{3}G(t)\right]\varepsilon_{kk}(o) + 2G(t)\,\varepsilon_{ij}(o) \quad .$$

For practical application the relaxation moduli are approximated by the following exponential series (Ref. 11):

$$K(t) = K_o + \sum_{i=1}^{NK} K_i \exp^{-t/\lambda_i} \qquad (21)$$

and

$$G(t) = G_o + \sum_{j=1}^{NG} G_j \exp^{-t/\beta_j} \quad . \qquad (22)$$

Substitution of Eqs. (21) and (22) into (20) gives

$$\sigma_{ij}(t) = \sigma^{o}_{ij} + \delta_{ij} \sum_{m=1}^{NK} K_m\, e^{-t/\lambda_m} \int_0^t e^{\tau/\lambda_m}\, d\varepsilon_{kk}$$

$$+ \sum_{n=1}^{NG} G_n\, e^{-t/\beta_n} \int_0^t e^{\tau/\beta_n}\left(2d\varepsilon_{ij} - \frac{2}{3}\delta_{ij}\, d\varepsilon_{kk}\right) \quad . \qquad (23)$$

If we assume the strain varies linearly within each time increment we can write

$$d\varepsilon_{ij} = \left(\frac{\partial \varepsilon_{ij}}{\partial \tau}\right) d\tau$$

and the resulting integrals can be evaluated to give a recursion formula for each term in the sum. Two forms are used:

$$I_m(t_{n+1}) = e^{-\Delta t/\lambda_m} I_m(t_n) + K_m \frac{\lambda_m}{\Delta t}\left(1 - e^{-\Delta t/\lambda_m}\right) \Delta\epsilon_{kk} \tag{24a}$$

and

$$J_p(t_{n+1}) = e^{-\Delta t/\beta_p} J_p(t_n) + G_p \frac{\beta_p}{\Delta t}\left(1 - e^{-\Delta t/\beta_p}\right)\left[2\Delta\epsilon_{ij} - \frac{2}{3}\delta_{ij}\Delta\epsilon_{kk}\right] \tag{24b}$$

where

$$\Delta t = t_{n+1} - t_n$$

and

$$\Delta\epsilon_{kk} = \epsilon_{kl}(t_{n+1}) - \epsilon_{kk}(t_n) \quad .$$

In terms of I_m and J_p we can rewrite Eq. (23) as:

$$\sigma_{ij}(t_{n+1}) = \delta_{ij}\left(K_o - \frac{2}{3}G_o\right)\epsilon_{kk}(t_{n+1}) + 2G_o\epsilon_{ij}(t_{n+1}) + \delta_{ij}\sum_{m=1}^{MK} I_m(t_{n+1}) + \sum_{p=1}^{MG} J_p(t_{n+1}) \quad . \tag{25}$$

The tangent modulus D_{ijkl} at t_{n+1} is written as:

$$D_{ijkl} = \delta_{ij}\delta_{kl}\left[\left(K_o - \frac{2}{3}G_o\right) + \sum_{m=1}^{MK} K_m \frac{\lambda_m}{\Delta t}\left(1 - e^{-\Delta t/\lambda_m}\right) - \frac{2}{3}\sum_{p=1}^{MG} G_p \frac{\beta_p}{\Delta t}\left(1 - e^{-\Delta t/\beta_p}\right)\right] + \left(\delta_{ik}\delta_{jl} + \delta_{il}\delta_{jk}\right)\left[G_o + \sum_{p=1}^{MG} G_p \frac{\beta_p}{\Delta t}\left(1 - e^{-\Delta t/\beta_p}\right)\right] \tag{26}$$

This is the expression of DK used in Eq. (16).

3.2 COMPUTER CODE ARCHITECTURE

Based on the above framework the FEM is used as a tool to study the transient response of a sheep torso model under external blast overpressure. Consideration of sheep anatomy is described in Section 2. Materials of various

organs are assumed to be described by the isotropic linear viscoelastic law as outlined in Section 3.1.4.

The computer code FEAPWS is used to perform this analysis. It is a version modified from FEAP74 developed by R. L. Taylor of UC Berkeley [11]. It was adapted to run on the JAYCOR mainframe Univac 1100/60. The storage arrangement has been restructured for clarity and user control. The program has been modified for different specific needs and tasks.

The computer code FEAPWS consists of two functional units: Data input module and equation solving and output module. In data input module the user defines his specific boundary-initial-value problem by supplying the following information (Fig. 3-1a):

1. Control parameters - including input of
   Dimensions - size of the problem
   Number of degrees of freedom per node
   Total number of elements, nodal points and materials
   Dimensioning size of storage arrays
   Total number of time steps, time increment of each time step
   Numerical method, stability and damping control parameters
   Output data managing parameters
   etc.

2. Material data - input of
   Mechanical properties
   Physical properties
   Kind of structural element to use
   etc.

3. Nodal data - for each node, input of
   Nodal number
   Coordinates
   Boundary constraint code
   etc.

4. Element data - for each element, input of
   Element number
   Element connection array
   Material type
   etc.

5. Boundary conditions - specification of magnitude and direction of displacement boundary conditions in terms of generalized nodal displacement.

6. Force loadings - specifications of magnitude and direction of point nodal force, surface traction and body force. These loading are all converted into equivalent generalized nodal force.

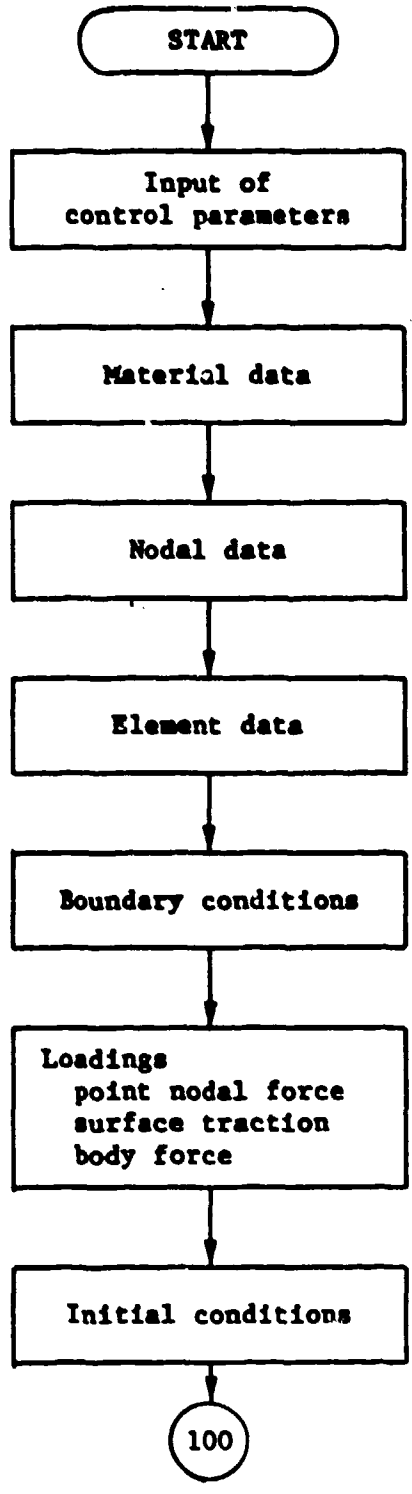

Figure 3-1(a). Flow chart showing data input module.

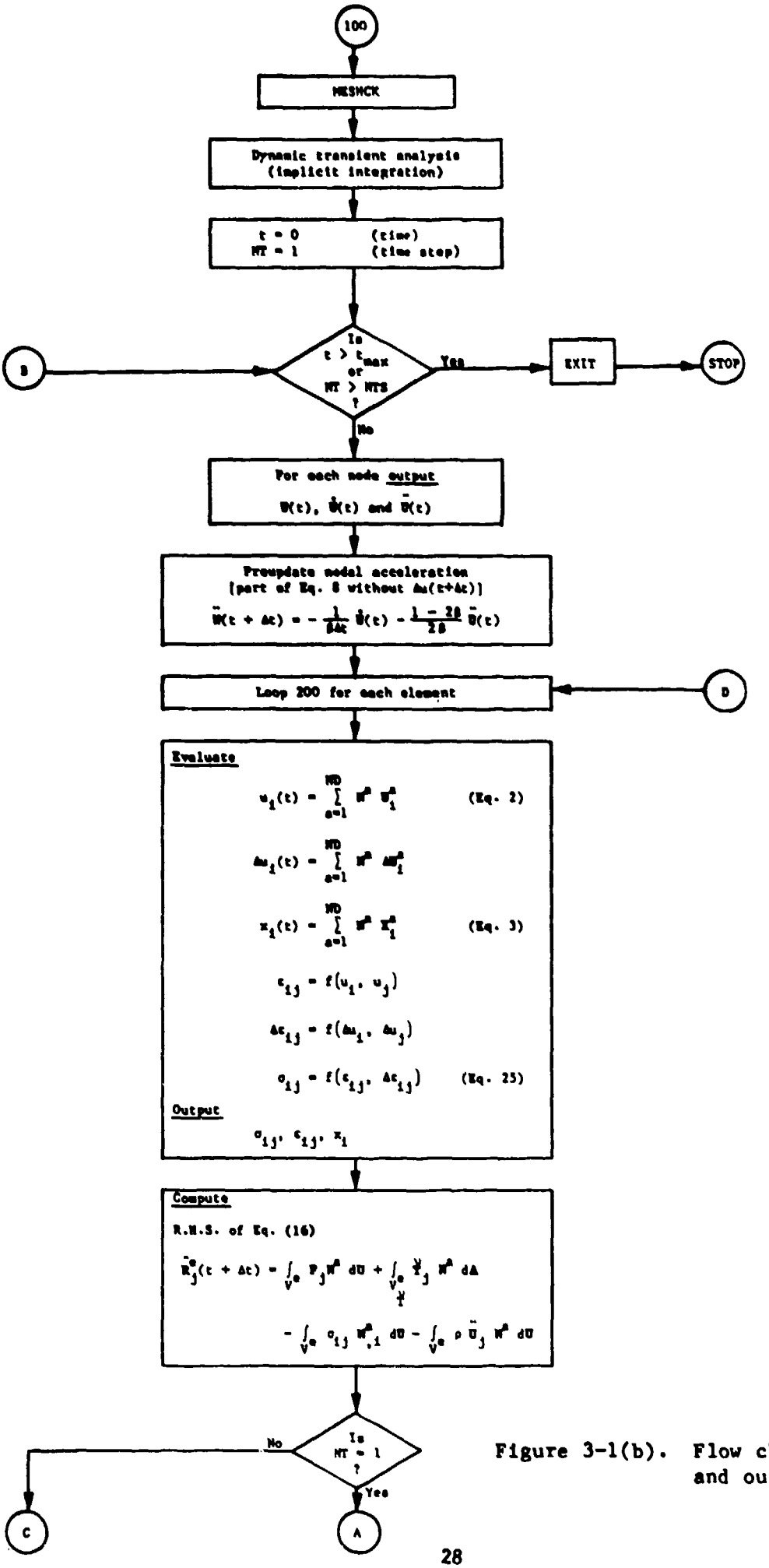

Figure 3-1(b). Flow chart showing solution and output module.

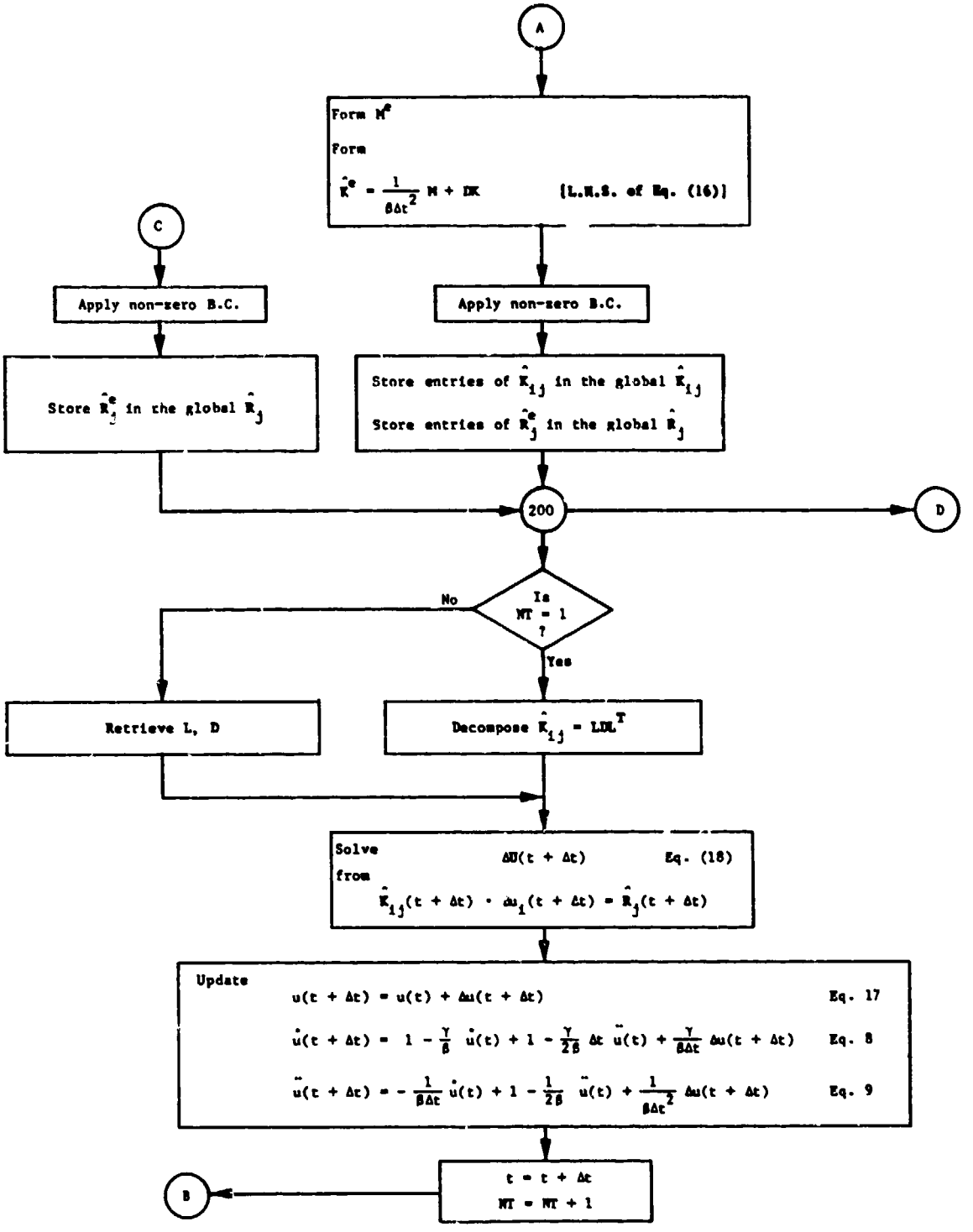

Figure 3-1(b). (Cont'd)

7. Initial conditions - input of displacement, velocity and acceleration initial conditions, if any.

The equation solving and output module starts with a check made on all the input data to make sure that they are consistent. The total number of equations, the maximum bandwidth are determined before the beginning of step-by-step time integration. For each given time t the following steps are followed:

1. For each node output U_i (displacement), $\dot{U}_i$ (velocity), and $\ddot{U}_i$ (acceleration) for the current time t.

2. Preupdate nodal acceleration

$$\ddot{W}_i(t + \Delta t) = -\frac{1}{\beta \Delta t}\dot{U}_i(t) - \left(\frac{1 - 2\beta}{2\beta}\right)\ddot{U}_i(t) \quad . \qquad \text{(part of the RHS of Eq. 11)}$$

3. For each element,

(A) Compute

$$u_i = \sum_{a=1}^{ND} N^a U_i^a \qquad \text{(Eq. 2)}$$

$$\Delta u_i = \sum_{a=1}^{ND} N^a \Delta U_i^a$$

$$x_i = \sum_{a=1}^{ND} N^a x_i^a \qquad \text{(Eq. 3)}$$

$$\varepsilon_{ij} = \frac{1}{2}\left(u_{i,j} + u_{j,i}\right)$$

$$\Delta\varepsilon_{ij} = \frac{1}{2}\left(\Delta u_{i,j} + \Delta u_{j,i}\right)$$

$$\sigma_{ij} = f(\varepsilon_{ij}, \Delta\varepsilon_{ij}) \quad . \qquad \text{(Eq. 25)}$$

(B) Output strain and stress components, $\varepsilon_{ij}(t)$ and $\sigma_{ij}(t)$.

(C) Compute the effective load vector $\hat{R}_j^e(t + \Delta t)$ (R.H.S. of Eq. 18).

(D) If NT ≠ 1 (not the first time step) go to (E).

(a) Form diagonal lumped mass matrix M^e.

(b) Form effective element stiffness matrix

$$\hat{K}^e = \frac{1}{\beta \Delta t^2} M^e + DK \quad . \qquad \text{(L.H.S. of Eq. 18)}$$

(c) Apply displacement boundary condition.

(d) Store entries of $\hat{K}^e$ in global effective stiffness matrix $\hat{K}$ (Fortran name A(I,J))

(e) Store entries of $\hat{R}^e$ in global effective load vector $\hat{R}$. (Fortran name DF)

(f) Decompose $\hat{K} = LDL^T$

(g) Go to 4

(E) (a) Apply displacement boundary conditions, if needed.

(b) Store entries of $\hat{R}^e$ in global effective load vector $\hat{R}$. (Fortran name DF)

(c) Retrieval of L and D.

4. Solve Δu from $\hat{K}(t + \Delta t) \cdot \Delta u(t + \Delta t) = \hat{R}(t + \Delta t)$. (Eq. 18)

5. Update

$$u_i(t + \Delta t) = u_i(t) + \Delta u_i(t + \Delta t) \qquad \text{(Eq. 17)}$$

$$\dot{u}_i(t + \Delta t) = \left(1 - \frac{\gamma}{\beta}\right) \dot{u}_i(t) + \left(1 - \frac{\gamma}{2\beta}\right) \Delta t \, \ddot{u}_i(t) + \left(\frac{\gamma}{\beta \Delta t}\right) \Delta u_i(t + \Delta t) \qquad \text{(Eq. 8)}$$

$$\ddot{u}_i(t + \Delta t) = -\left(\frac{1}{\beta \Delta t}\right) \dot{u}_i(t) + \left(1 - \frac{1}{2\beta}\right) \ddot{u}_i(t) + \left(\frac{1}{\beta \Delta t^2}\right) \Delta u_i(t + \Delta t) \qquad \text{(Eq. 9)}$$

6. $t = t + \Delta t$
   NT = NT + 1
   Go to 1 for next time step.

For brevity these steps are summarized in the flowchart on Figure 3-1(b). Note that this algorithm is for linear problems only. For nonlinear problems iteration should be called for to obtain Δu under prescribed error tolerance from Eq. (18) in step 4.

3.3 DATA EXCHANGE BETWEEN FINITE ELEMENT ANALYSIS PROGRAM AND GRAPHICS PROCESSOR

MOVIE is an interactive graphics program installed in the standalone SUPERSET graphics processor (SST) while FEAPWS is the finite element analysis program on the Univac 1100/60. The linkage between these two codes will enable us

- To define and modify the geometry of finite element models with MOVIE and at the same time display it on a graphics terminal until satisfied,
- To visualize the body deformation and display various function distributions of the model under analysis.

To achieve this the following steps must be followed (see Figure 3-2):

1. Define the model geometry with MOVIE in SST.
2. Rewrite the geometry data in the "Univac way" since the ASCII code is written in different ways on different machines. This is done with UTL.READ80/ASCII.
3. Once the data is transmitted to the Univac, rewrite the geometry file in FEAP format. Information on material properties, loadings, boundary conditions, initial conditions and the FEM model basic parameters as well as the numerical scheme parameters are added, then an input file for FEM analysis is prepared. This subtask is performed by LINK.MOVFEA.
4. Upon completion of FEM transient analysis with FEAPWS, the computational results (displacement, stress components, etc.) are written to an output file in MOVIE format. This is done by LINK.FEAMOV.
5. Rewrite the resulting file in "SST way" with UTL.WRITE80/ASCII so it is recognizable to SST.
6. Once the data is transmitted to the SST, then the graphics display functions of MOVIE can be used to visualize the computational results. Even then, the procedure to display any result is quite tedious. The results are written to separate data files, e.g., geometry, displacement (nodal values), and scalar functions (element values), for each time step. A long sequence of interactive commands have to be supplied by the user to manipulate the data into a form ready for graphic display. To simplify this procedure, file manipulation commands and interactive display commands have been packed and written as two programs, FILEPREP and LOOK which are executed by the user at the SST terminal.

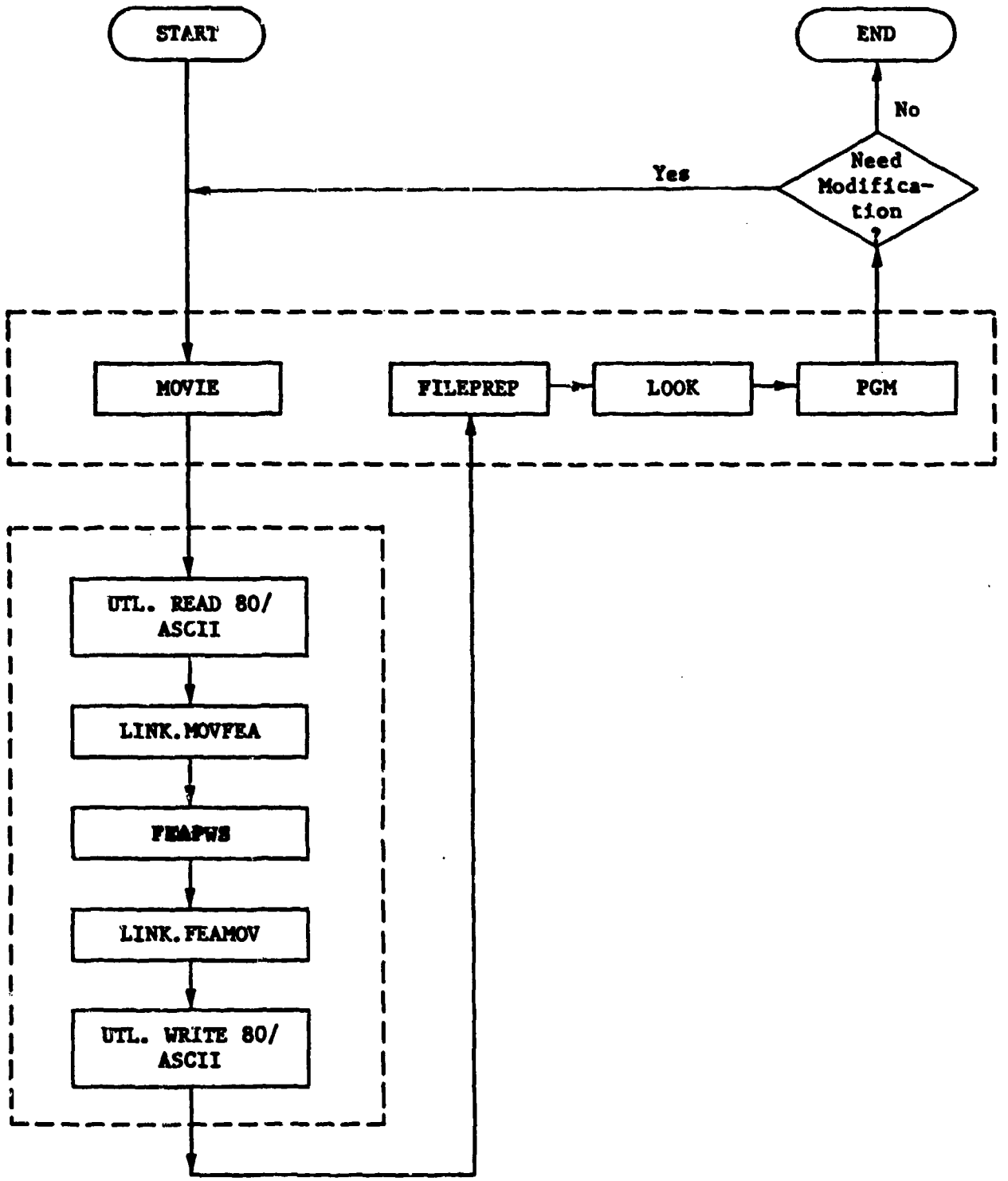

Figure 3-2. Block diagram summarizing steps in linkage automation between MOVIE and FEAPWS.

7. If further corrections or modifications (spatial element refinement, varying geometric size, shape, material properties, different loadings, boundary conditions, etc.) are necessary, steps 1 through 6 are repeated.

Programs written for each of the specific steps in this section are reproduced in Appendix A for future reference.

4. A SIMPLIFIED THREE-DIMENSIONAL MODEL

4.1 DESCRIPTION OF THE MODEL

4.1.1 Treatments of Lumped Material Properties on the FEM Model

Based on the sheep torso anatomy, a three-dimensional FEM model of 16 eight-node brick elements and 64 nodal points is defined to capture the major organ responses important in blast overpressure exposure of a sheep. Figure 4-1(a) is an exploded view showing representations of various major internal organs in the thorax and abdomen. Figure 4-1(b) indicates the dimensions of different parts in the model.

To describe all the other structural aspects of the anatomy (muscle layer, rib cage, spinal column, etc.) and not increase the number of solid elements used in the analysis, it is necessary to implement a model to combine lumped material properties (suggested by Professor Y. C. Fung). The idea is to lump the inertial and elastic properties of the rib cage and muscle layers to the edges and nodal points of those elements describing the internal organs. This treatment brings the contributions of rib cage and muscle layer into consideration. It, however, greatly reduces the size of matrix equation to be solved at each time step and makes the computational cost and time feasible.

To explain this in detail we shall write the global linearized form of equation of motion for internal organs as [Eq. (16) of Sec. 3.1.3]

$$\left\{ DK\left(U^{j}_{n+1}\right) + \frac{M}{\beta \Delta t^{2}} \right\} \cdot \Delta U^{j}_{n+1} = \left\{ R_{n+1} - K\left(U^{j}_{n+1}\right) - M\ddot{U}^{j}_{n+1} \right\} \qquad (16)$$

where M represents the contribution due to mass inertia of various internal organs. The additions of muscle layer and rib cage are justified as follows:

Muscle Layer - The muscle layer is considered to be "bordering" the external surface of the internal organ medium. To lump its mass to the FEM representation of the internal organs we first have to determine the volume of each of the muscle masses. This is estimated by multiplying the surface area, obtained from the coordinates of the 4 nodal points, by an average thickness

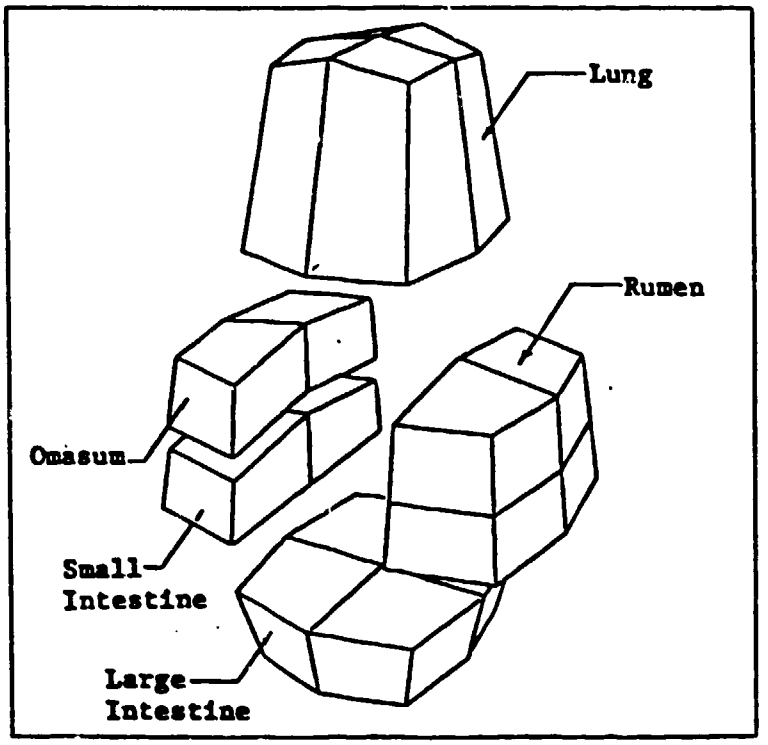

(a) Exploded view showing various organs represented

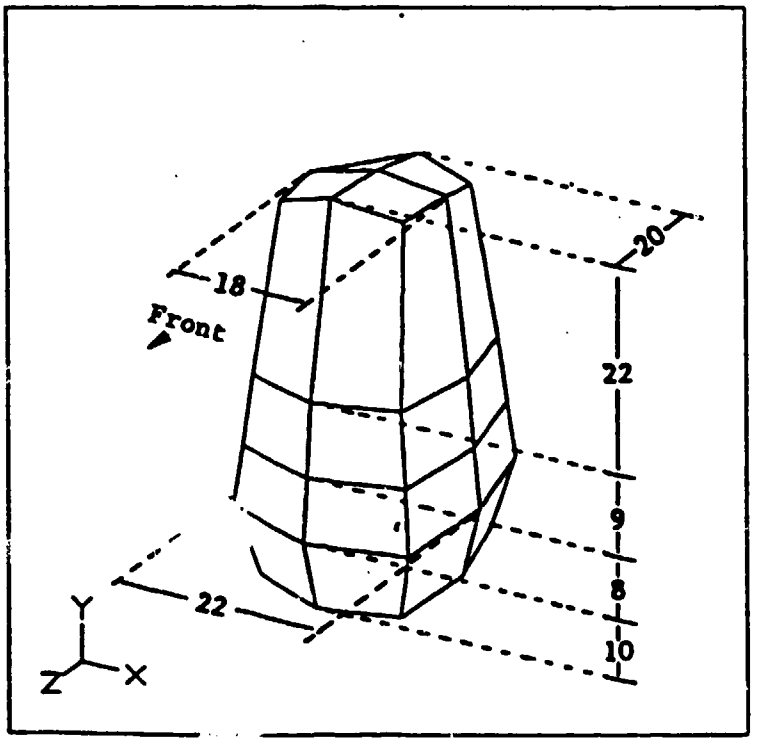

(b) Major dimensions of sheep torso model (cm)

Figure 4-1. Sheep torso model (head up posture).

of 3.5 cm. The density is assumed to be 1 gm/cm^3. The total mass of a muscle layer patch is to be shared by the four nodal points defining the bordering surface. Therefore, one-quarter of the mass of this muscle patch is added to the corresponding diagonal term of the mass matrix M in Eq. (16). In the computer program, this is done at the element level before the assembly of the global equation.

Rib Cage - The estimation of lumped mass due to rib cage is done by first considering that only a portion of the external surface of lung elements borders the rib cage. This effective bordering surface is hypothetically assumed to be one-third of the surface. In other words, for a lung external surface, one-third of the area is under the bony rib which has a thickness of 1 cm and mass density of 2.8 gm/cm^3. Its total mass is then added to the four nodal points defining the external bordering surface. Computationally, one-quarter of this mass is added to the corresponding diagonal term of the mass matrix M in Eq. (16).

When the body is under external surface loading, the stiffness of the whole rib cage arises from the stiffness of the connecting ligaments and the bending rigidity of individual bony elements. To study the global characteristic responses of the lung under blast wave loadings, a detailed analysis accounting for the bending, compression, and shear deformations of the rib cage does not seem to be beneficial at this stage.

Similar to the treatments of lumped mass for the muscle layer and rib cage, the structural rigidity of the rib cage is lumped to the finite element stiffness representation of the surface internal organs. The procedure is to lump a structural frame, which consists of bars of high stiffness in its direction of axial compression and angular rotation, such that edges defining the lung elements in the sheep model move in conjunction with the "rib cage" under any external force loading (see Fig. 4-2). The stiffness of bars constituting the rib cage is chosen to be 1.7×10^{11} dyne/cm^2. The contribution of stiffness due to this lumped rib cage is added to the corresponding force-deflection constants K_{ij} and DK_{ij} of Eq. (16).

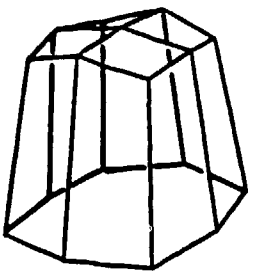

(a) Structural frame representing rib cage. This frame consists of high axial stiffness bars and will cap the torso.

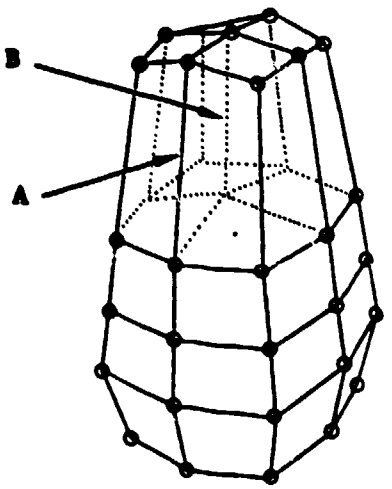

(b) View of torso model with circles denoting lumped mass.

Figure 4-2. Lumped rib cage model.

4.1.2 Material Properties of the FEM Model

The most crucial factor in determining the structural response under mechanical loading is the constitutive relationships of the various material components. Investigation of the material properties of the lung was carried out at UCSD as part of the BOP program [6]. For the abdominal organs we have referenced the experimental data from Strength of Biological Material by Yamada and Evans [12]. Bulk modulus as defined in this literature comes from expansion or bursting experiments performed in a way similar to "open airway" experiments on the lung [6]. Bulk moduli for stomach, small intestine, large intestine (dogs) are in the range of 10^4-10^6 dynes/cm^2 and shear moduli are estimated to be in the same range. A gross bulk modulus of 10^{10} dyne/cm^2 (that of water) should be a better choice when the water content is taken into account. Table 4-1 lists the material properties used in the 3-D model presented in this section. The constitutive relationship used is described in Section 3.1.4.

4.2 COMPARISON WITH EXPERIMENTAL DATA

To validate the model in the simulation of sheep's intrathoracic responses to external blast overpressure we have compared the numerical results with experimental measurements under the same loading conditions. The experiments were performed by WRAIR and Lovelace ITRI during 1981 and 1982. Experimental raw data supplied to us by WRAIR [Appendix C] are time recordings of external blast, sheep's esophageal pressure taken at the level of the seventh or ninth intercostal, and the "intrathoracic pressure" taken from an anthropomorphic dummy (VICTOR). For convenience we have divided the comparison into two groups, single peak and double peak studies. The external blast overpressure recordings are digitized and then applied to the body surface of the model. To account for the increased loading at the body surface directly facing blast arrival due to reflection we multiply the recorded side-on blast pressure by a factor of 2. The predicted intrathoracic pressures (ITP) were taken from the center of the four elements representing the lungs (point B on Fig. 4-2). These ITP predictions are then compared with the experimental measured esophageal pressures.

Table 4-1. Material Properties of Various Organs Used in the Simplified 3D Finite Element Model

Organ	Property	Value	Source
Lung	K_o	1.4×10^6 dyne/cm^2	Ref. 6
	G_o	1.0×10^4 dyne/cm^2	computed from $[3K(1-2\nu)]/[2(1+\nu)]$
	ν_o	0.30	Ref. 6
	K_1	0.7×10^6 dyne/cm^2	assumed
	G_1	0.5×10^4 dyne/cm^2	assumed
	λ_1	1 msec	assumed
	β_1	1 msec	assumed
	ρ	0.37 g/cm^3 (small animal)	Ref. 5
		0.19 g/cm^3 (large animal)	Ref. 5
Rumen	K_o	1.0×1.0^{10} dyne/cm^2	assumed
	G_o	1.0×10^4 dyne/cm^2	Ref. 12
	ν_o	0.50	assumed
	K_1	5×10^9 dyne/cm^2	assumed
	G_1	5×10^3 dyne/cm^2	assumed
	λ_1	1 msec	assumed
	β_1	1 msec	assumed
	ρ	1.0 g/cm^3	assumed
Omasum	K_o	1.0×10^{10} dyne/cm^2	assumed
	G_o	1.0×10^4 dyne/cm^2	Ref. 12
	ν_o	0.50	assumed
	K_1	5×10^9 dyne/cm^2	assumed
	G_1	5×10^3 dyne/cm^2	assumed
	λ_1	1 msec	assumed
	β_1	1 msec	assumed
	ρ	1.0 g/cm^3	assumed
Small intestine	K_o	1.0×10^{10} dyne/cm^2	assumed
	G_o	2.6×10^5 dyne/cm^2	Ref. 12
	ν_o	0.50	assumed
	K_1	5×10^9 dyne/cm^2	assumed
	G_1	1.3×10^5 dyne/cm^2	assumed
	λ_1	1 msec	assumed
	β_1	1 msec	assumed
	ρ	1.0 g/cm^3	assumed
Large intestine	K_o	1.0×10^{10} dyne/cm^2	assumed
	G_o	7.5×10^4 dyne/cm^2	Ref. 12
	ν_o	0.50	assumed
	K_1	5×10^9 dyne/cm^2	assumed
	G_1	3.8×10^4 dyne/cm^2	assumed
	λ_1	0.5 msec	assumed
	β_1	0.5 msec	assumed
	ρ	1.0 g/cm^3	assumed

4.2.1 Single Peak Exposure

Four cases of single peak loading are demonstrated in Figure 4-3. The four experiments were performed on different animals under different amounts of TNT free-field explosion at various distances from the explosive center.

Each of the experimental esophageal pressure recordings shows the local lung tissue is under compression phase during the first 10 ms with peak pressure occurring at 4-7 ms from the onset of the blast arrival at the model body surface. Approximately 10 ms after the onset the local lung tissue starts experiencing tensile phase with slower response and reduced amplitude. Reduction in amplitude and changes in frequency may be due to the damping occurring inside the body.

The 16-element body representation is certainly a simplified model. The purpose is to capture the main body response characteristics. For that consideration ITP predictions of different cases (Fig. 4-3) demonstrate reasonably good agreement with experimental measured esophageal pressures when the blast is less than 10 psi.

4.2.2 Double Peak Exposure

Blast pressure recordings taken from the double peak study of Lovelace ITRI during October 1981 and May 1982 are also applied on the 3-D model to study its intrathoracic pressure responses. Figure 4-4 shows comparisons of ITP prediction and experimental measured esophageal pressure for three cases with different time duration between two blast peaks. These comparisons shows that:

1. For Δt = 3.6 and 7.6 ms the two humps of the calculated ITP response to double peak blast are not distinct as are the data.

2. For Δt = 9.7 ms the timing and low frequency response of model prediction are comparable to those of experimental measurements. But as in the other two cases, the wave form of the experimental measured esophageal pressure has a faster rise and larger peak pressure.

For these cases the peak blast rises to 40 psi in 0.5 ms; it also falls off to 0 within 2 to 3 ms. It appears that a more refined model is needed to provide both spatial and temporal resolution under these ranges of loading.

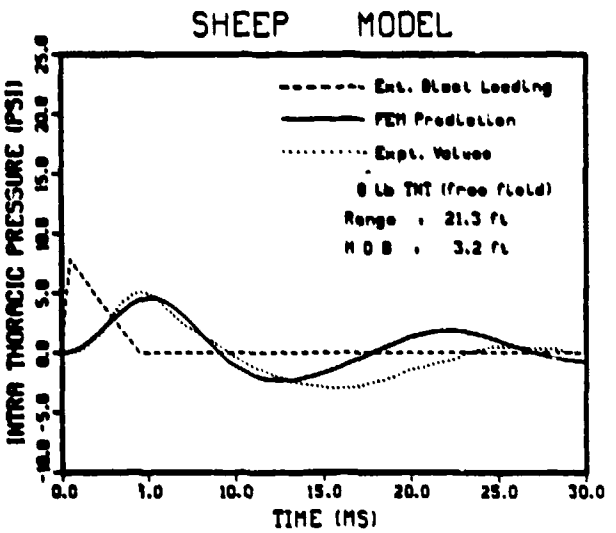

(a) 8 lb TNT (free field), range 21.3 ft, HOB 3.2 ft

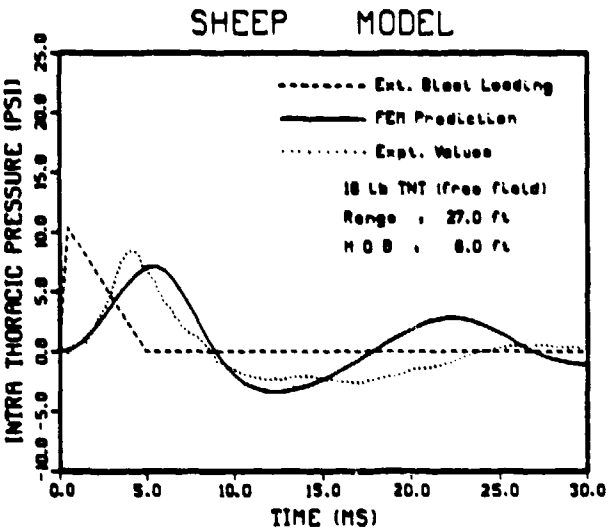

(b) 16 lb TNT (free field), range 27.0 ft, HOB 6.0 ft

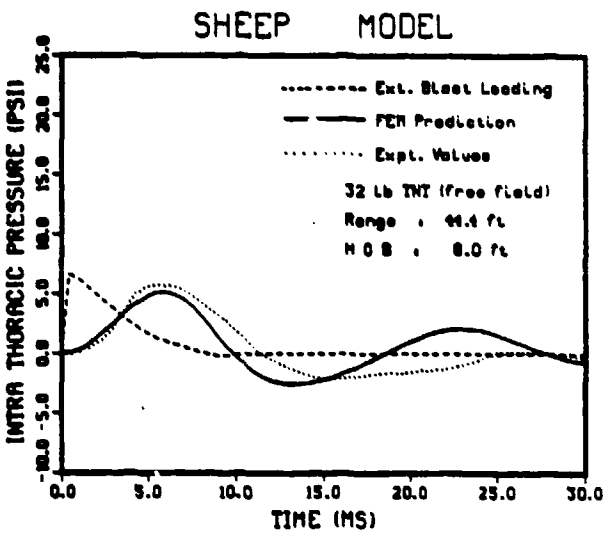

(c) 32 lb TNT (free field), range 44.4 ft, HOB 8.0 ft

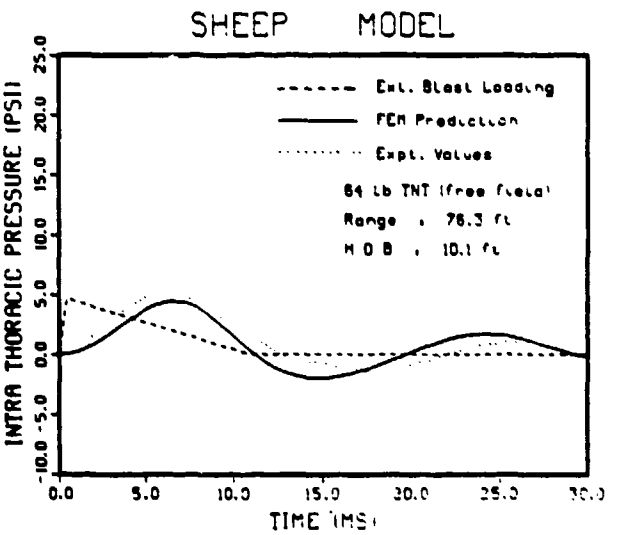

(d) 65 lb TNT (free field), range 76.3 ft, HOB 10.1 ft

Figure 4-3. Comparisons of FEM predictions and experimental ITP under different single-peak blast loadings.

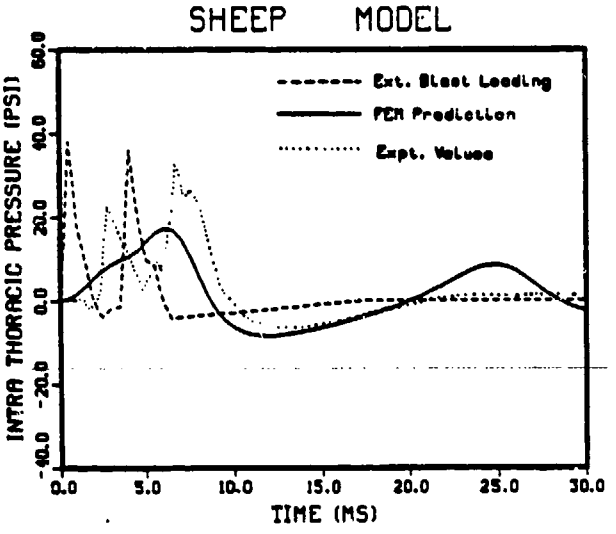

(a) Δt = 3.6 ms

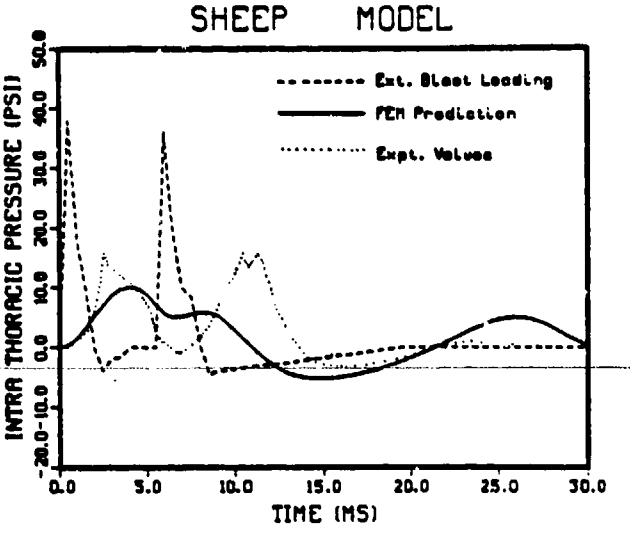

(b) Δt = 7.6 ms

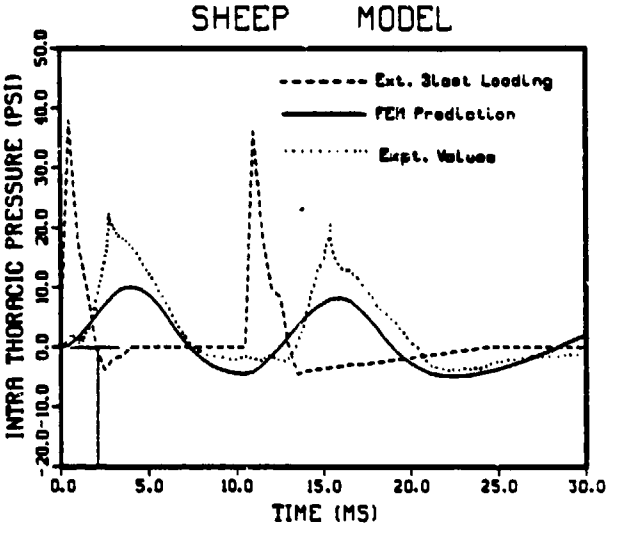

(c) Δt = 9.7 ms

Figure 4-4. Comparisons of FEM predictions and experimental ITP under different double-peak blast loadings. Δt is the time duration between two blast peaks.

4.3 SENSITIVITY STUDIES

4.3.1 Influence of Abdominal Air on ITP Response

Sheep are used as experimental subjects at WRAIR and Lovelace ITRI in order to correlate the external blast parameter with injury map. Sheep, however, have large amounts of air in their GI tracts. The question of how much influence this trapped air has on ITP response, therefore, needs clarification.

As an attempt to answer this question, the simplified 16-element sheep model with different degrees of abdominal air-filling, was exposed to blast loading. Figure 4-5 shows the results of ITP response for various cases. In case (a) the model does not have any air in its abdomen. In cases (b)-(d) the models are given increasing amounts of air in the rumen. Case (d) has half of the rumen/small intestine region filled with air. Compared with case (a), the peak ITP increase is less than 10%. It indicates that the ITP response is relatively insensitive to the abdominal air. The ITP response is primarily caused by loadng on the chest wall.

This supports the experimental work of Zuckerman [14] and Clemedson and Jönsson [2,3] in which they demonstrate with rabbits, dogs and other species that lung injuries are caused primarily by blast loading on the chest wall. It is noted that this does not exclude the possibility of increased GI injury occurrence and severity on sheep due to abdominal wall blast loading when there is an excess amount of air trapped in the GI tract.

4.3.2 Isoimpulse Studies

To further examine the behavior of the current version of the model, isoimpulse studies have been done in the following two ways (rabbit size model):

1. Isoimpulse blast of 10 psi-ms with different dP/dt is applied on the surface of the model. It appears that the larger the dP/dt on its rise to peak pressure, the sooner the peak pressure is reached. The peak pressure also decreases but in an insignificant magnitude in these comparisons. Figure 4-6 shows the ITP response to varying dP/dt.

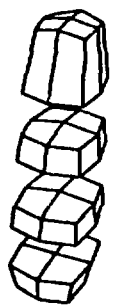

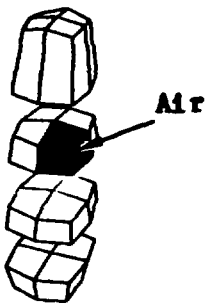

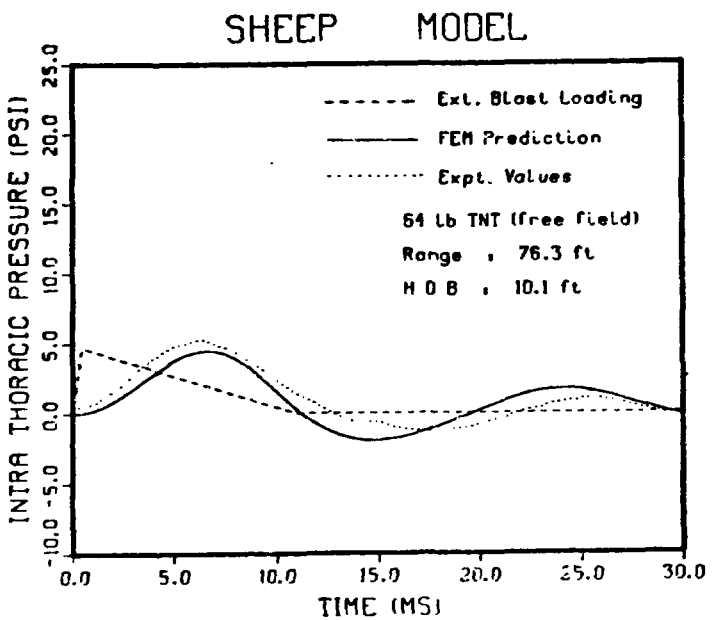

(a) Model without air in the abdomen

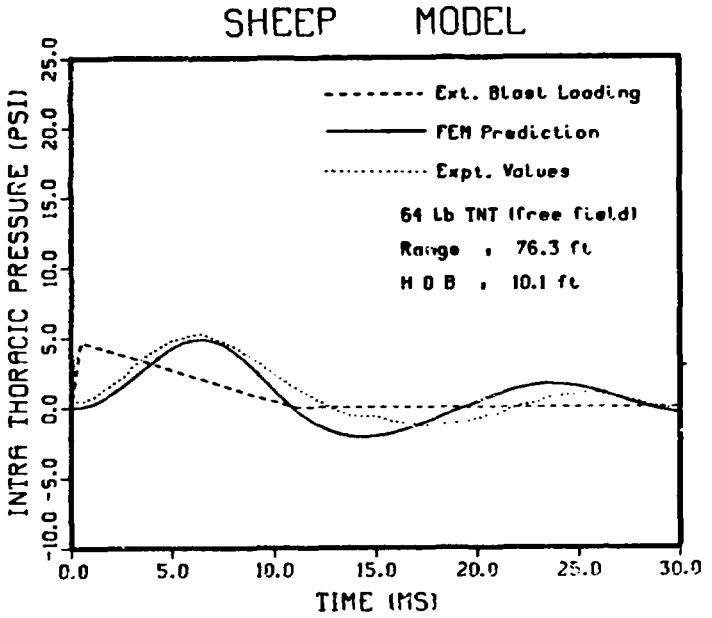

(b) Model with one of the rumen elements replaced by air

Figure 4-5. Influence of abdominal air on ITP responses.

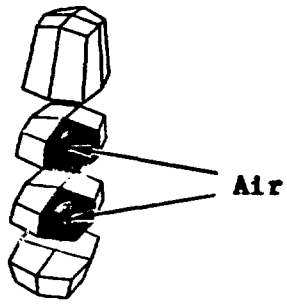

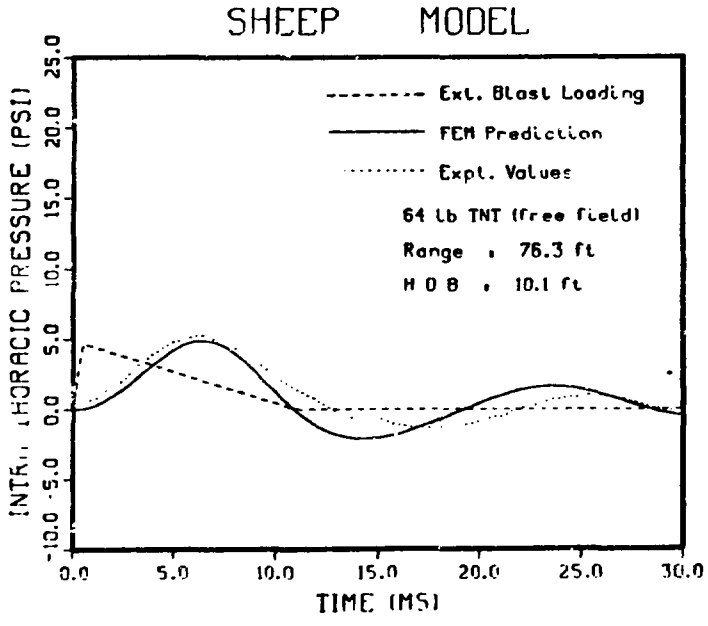

(c) Model with two of the rumen elements replaced by air

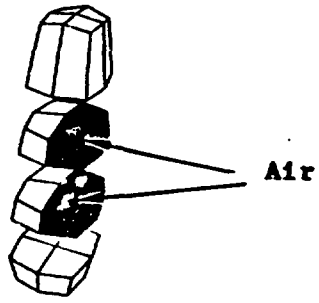

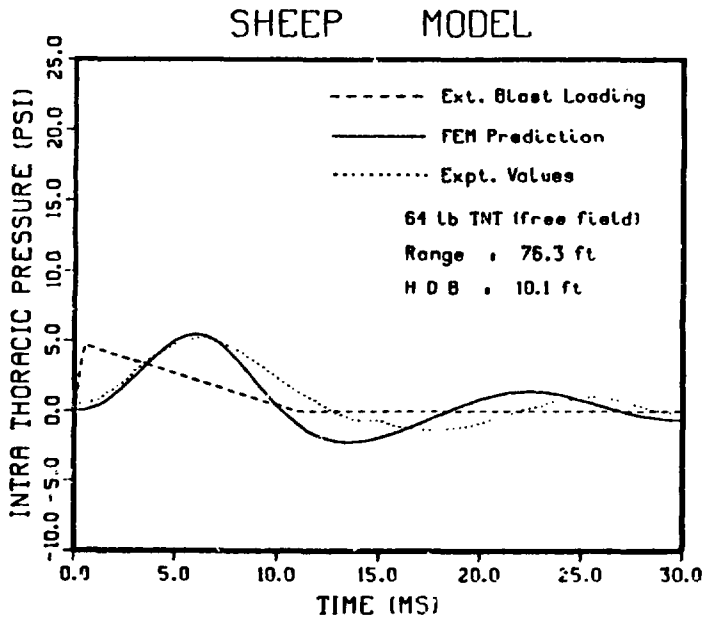

(d) Model with four of the rumen elements replaced by air

Figure 4-5. (Cont'd).

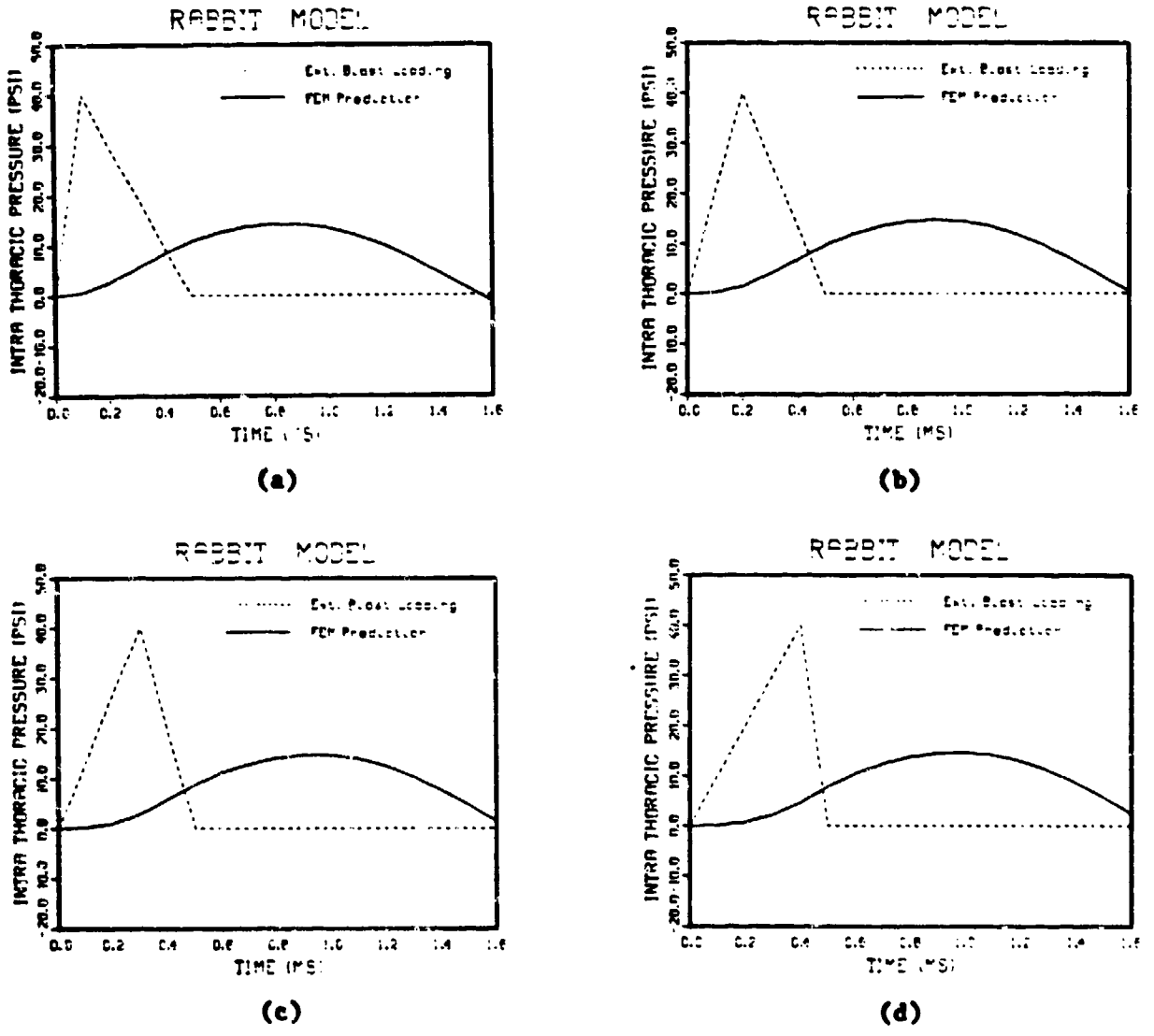

Figure 4-6. Isoimpulse blast loadings on rabbit model with different dP/dt.

2. Isoimpulse blast loading (10.5 psi-ms) of square waves at different durations were also applied on the surface of the model. The higher the magnitude of the peak external blast and the shorter the loading duration the faster the [d(ITP)]/dt and the higher that peak ITP occurs. Also note the peak ITP occurs at earlier time (Fig. 4-7). This suggests that for the impulse loading of 10.5 psi-ms the higher peak external blast and shorter duration could incur more risk. Experimental results of Richmond, et al. (Fig. 4-8) showed that the probability of lethality (LD_{50}) becomes much higher at higher external blast pressure and shorter duration for a given impulse (dashed lines). This was also demonstrated in the iso-impulse study of WRAIR on sheep.

4.3.3 Effects of Geometric Size

Keeping the shape of the model the same and retaining the same material properties, we vary the size of the model from a "sheep" to a "rabbit" to observe the effect of animal size on various physical parameters under the same "short duration" blast. Figure 4-9(a) shows different ITP responses due to different geometric sizes. The curve labeled 1.0 corresponds to that of a sheep considering the longitudinal length of the sheep torso to be 50 cm. The curve labeled 0.4 corresponds to that of a rabbit with 20 cm torso length. Comparison of the curves shows that the smaller size animal is affected by a larger disturbance. Namely, the higher ITP, [d(ITP)]/dt and higher oscillation frequency. Figure 4-9(b) and (c) show comparisons of normalized chest wall displacement and front chest velocity, respectively. Similar tendencies are seen on displacement and velocity histories. For a given blast overpressure loading the small animal is under greater disturbance. The ITP responds at higher amplitude and higher rate of pressure rise. The whole body vibrates at a faster frequency.

4.3.4 Effects of Varying Lung Bulk Modulus

By varying the bulk modulus of the lung (but keeping the same Poisson ratio, $\nu = 0.40$) we observe its effect on animal response under the "short duration" blast. Figure 4-10(a) shows the ITP histories for different cases. It appears that for larger bulk modulus the ITP rises faster and a higher ITP can be attained. The frequency response is also higher under the same external blast. We also vary the bulk modulus of the abdominal contents, rumen,

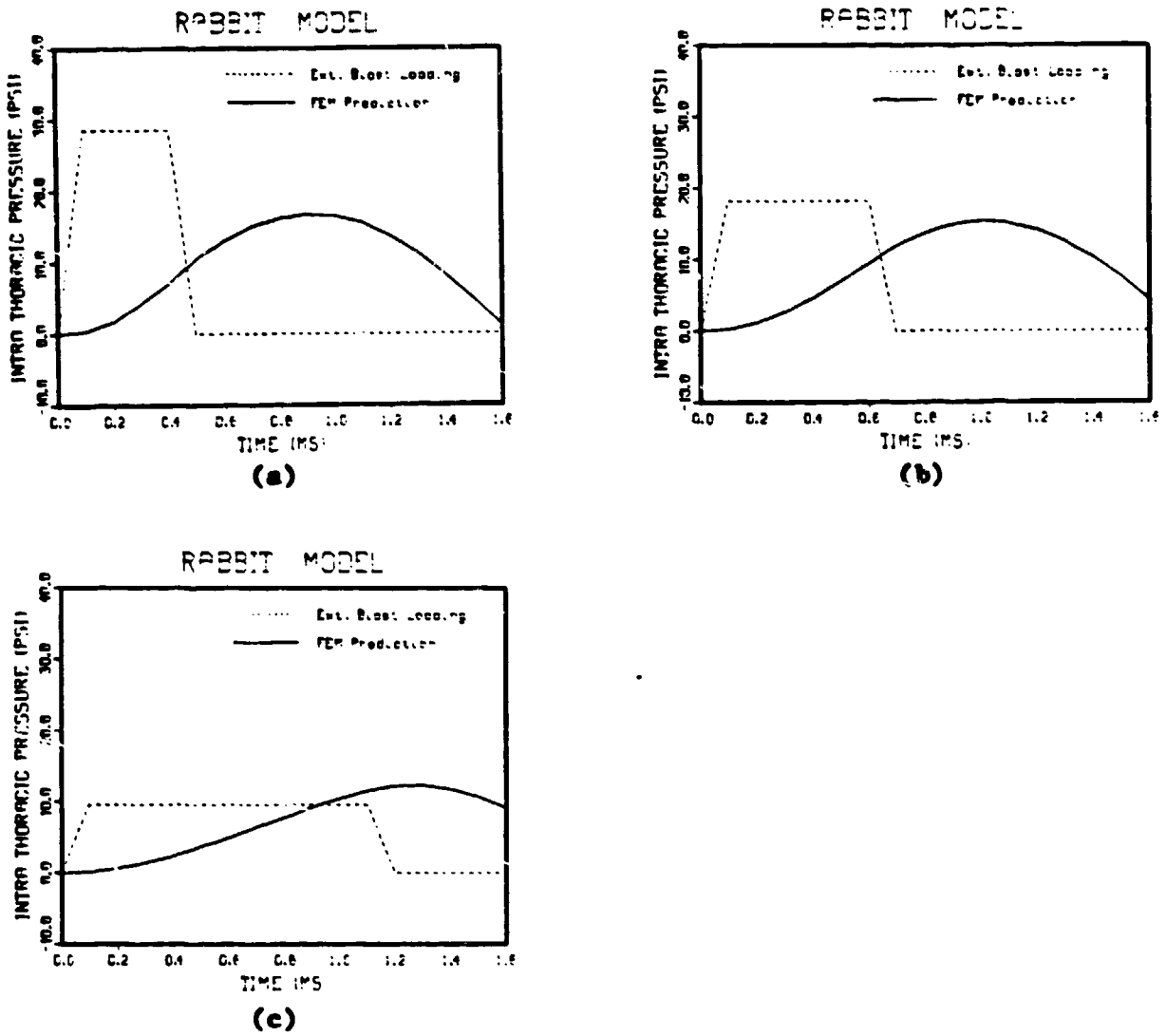

Figure 4-7. Isoimpulse loadings of square waves on rabbit model with different loading durations.

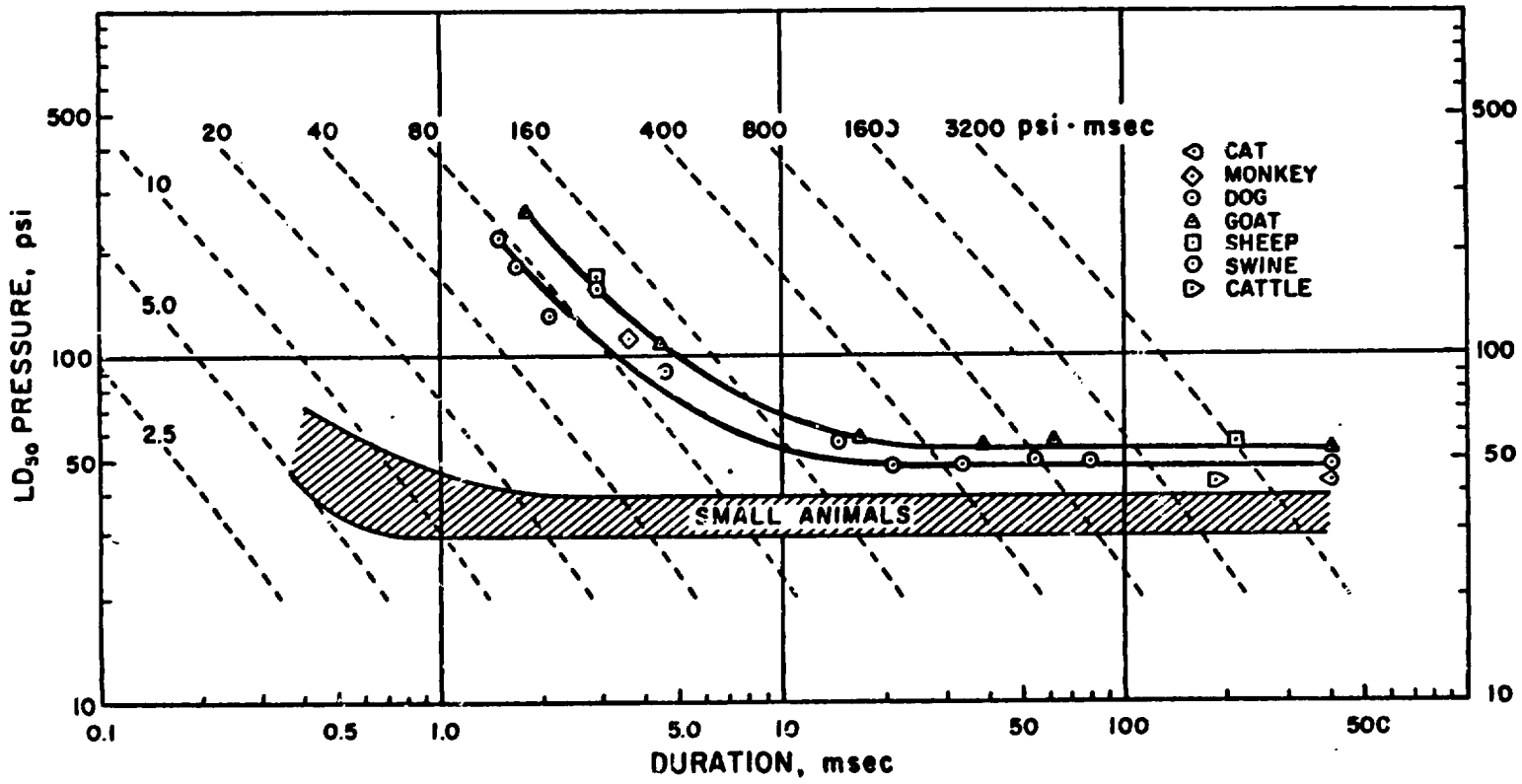

Figure 4-8. Pressure-duration relationship and lethality at 24 hours for large and small animals (mice, rats, hamsters, guinea pigs, and rabbits). All measurements were made at an ambient pressure of 12 psi. Reproduced from Richmond et al. (Ref. 10).

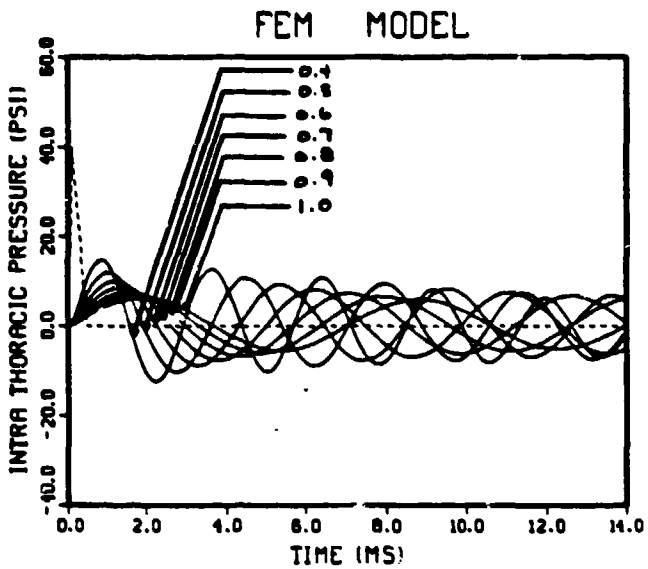

(a) ITP

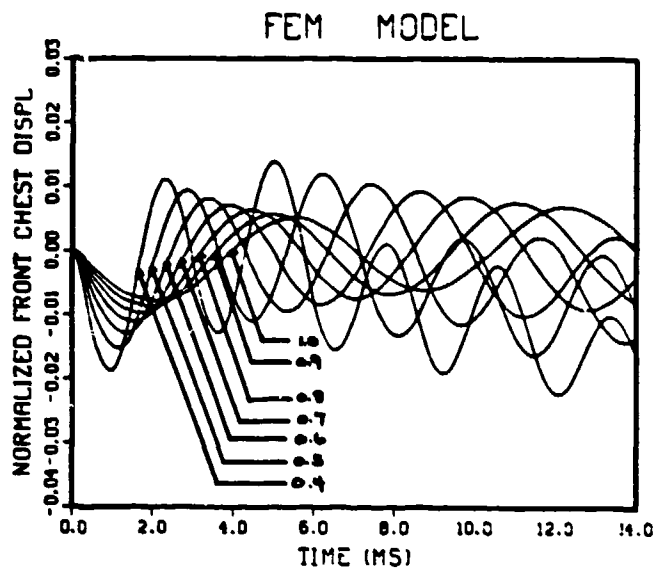

(b) Normalized displacement

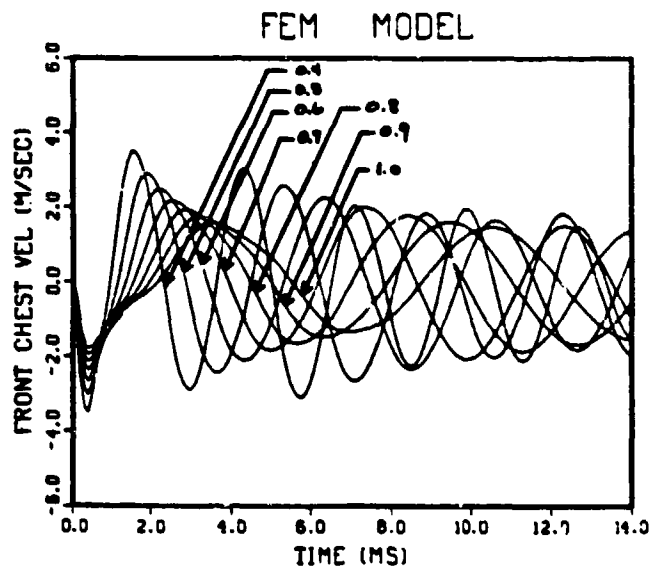

(c) Velocity

Figure 4-9. Variation of response parameter histories with changes in geometric dimensions of the model. Sizes represented range from sheep (labeled 1.0) to rabbit (labeled 0.4). The geometric shape and material properties are kept constant.

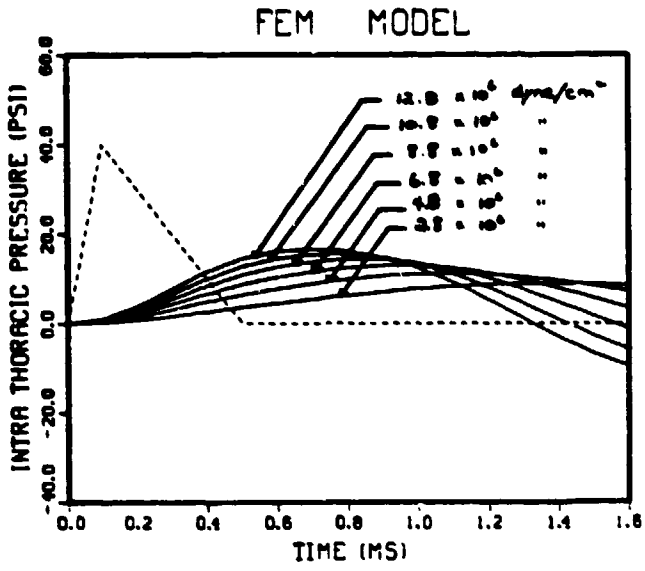

(a) ITP

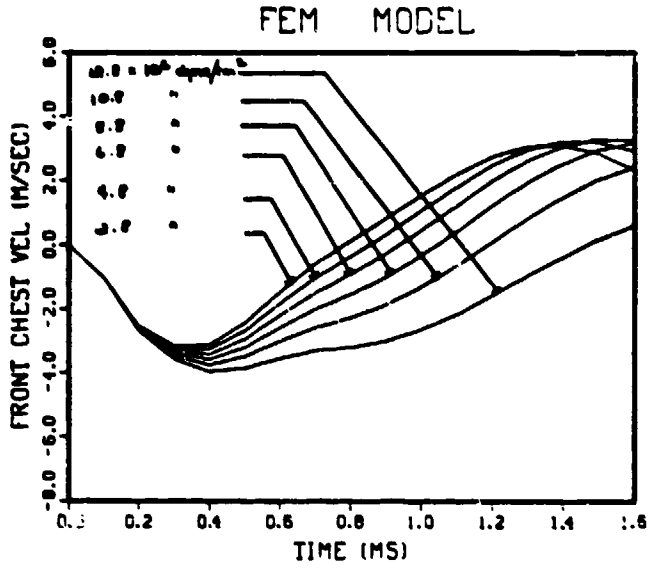

(b) Normalized displacement

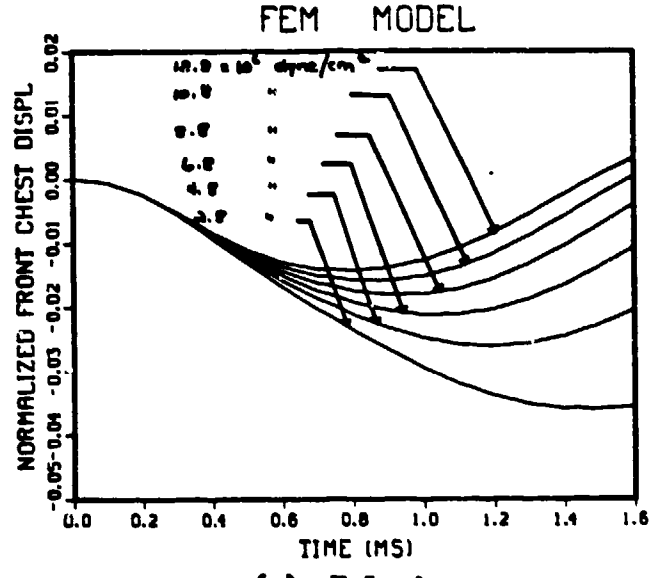

(c) Velocity

Figure 4-10. Variation of response parameters with changes in the bulk modulus of the lung.

intestines, etc. The observation is that it makes a slight change on ITP for a wide range variation of abdomen bulk modulus. Figure 4-10(b) and (c) shows the normalized chest displacement and velocity, respectively. The phenomena is similar to that in ITP histories. The larger the bulk modulus of the lung the faster and higher the response is.

5. A CROSS-SECTIONAL TWO-DIMENSIONAL MODEL

5.1 INTRODUCTION

A three-dimensional finite element model of sheep torso has been constructed as described in the previous section. This model is used to predict the intrathoracic pressure response when a sheep is exposed to external blast loadings. The prediction was compared with experimental measured esophageal pressure history as described previously. The existing experimental data mainly comes from overpressure taken at one or two depths in the animal esophagus. Jönsson et al. [8] also measured lung overpressures directly by introducing transducers through the trachea into the right and/or the left lung in rabbit impact experiments. Their measurements indicated that different overpressure histories were experienced by different parts of the lung in response to the impact loading delivered at one side of the body surface. Examination of the lung trauma following incidences of blast waves or high velocity impact [8,14] reveal that gross hemorrhage on the pleural surface, in particular the area near the impact side and the area near the heart. It suggests that wave dynamics may play a role in determining the injury site and severity. The complex phenomena of wave reflection at boundaries and wave focusing at geometric focal points may cause different types of injury at different regions. To understand the injury mechanism associated with the lung under blast exposure we need to follow the incident wave as it propagates across the body. We need to know how different parts of the body respond to external disturbance and how mechanical stress or energy is built up at different regions of the lung. With this knowledge we can proceed to correlate the injury map and injury severity from animal experiments. An injury criterion is expected to be established in terms of local tissue mechanical response parameters.

To supply this greater detail, a two-dimensional FEM model was constructed. This model is complementary to the three-dimensional model in providing both temporal and spatial resolution. Characteristics of wave propagation across different parts of the body can be monitored.

5.2 DESCRIPTION OF THE MODEL

5.2.1 Geometry

A two-dimensional model is still a simplification of the actual three-dimensional body. To justify the two-dimensional model it has been demonstrated by Clemedson and Jönsson [2,3], by using protective layers covering either chest or abdomen (rabbit), that lung injuries are caused primarily by chest loading. The effect of mouth airflow and the indirect abdominal loading through the diaphragm were found to be insignificant for lung injuries. Based on the sheep thorax cross section at the level of the seventh thoracic vertebra [9], a two-dimensional plane strain model was constructed (see Fig. 5-1). The model consists of four major organs - skeletal muscle, rib, lung and heart. The objectives are (1) to understand the underlying mechanics of wave dynamics in biological bodies during blast exposures and (2) to predict the overpressure occurrences at different parts of the lung when a sheep is under blast wave incidence.

Following the FEM formulation of Section 3.1, the two-dimensional discretization mesh is defined by 133 nodes and 122 four-node isoparametric continuum elements. Two degrees of freedom (displacement) are assigned to each node. Bilinear interpolation functions are used for element approximation. Implicit integration scheme with Newmark approximation is employed for the temporal discretization. Analysis is performed for 30 ms from the onset of wave arrival at the body surface, since experimental measured esophageal pressures become diminishing after 30 ms in response to the loadings of interest in this program. For most of the analysis a time step of 0.5 ms is chosen.

5.2.2 Modeling of the Rib Cage

The geometrical structure and the kinematic motion of the rib cage is three-dimensional by nature, so we must find a two-dimensional equivalent representation to account for its rigidity and kinematic degrees of freedom. Considering its role in resisting as well as delivering the external impluse loading from body surface to the internal organs, it is obvious that a closed-ring of bony rib overexaggerates its rigidity. Yet a closed-ring of muscle also underestimates the global stiffness of the whole body structure. In order

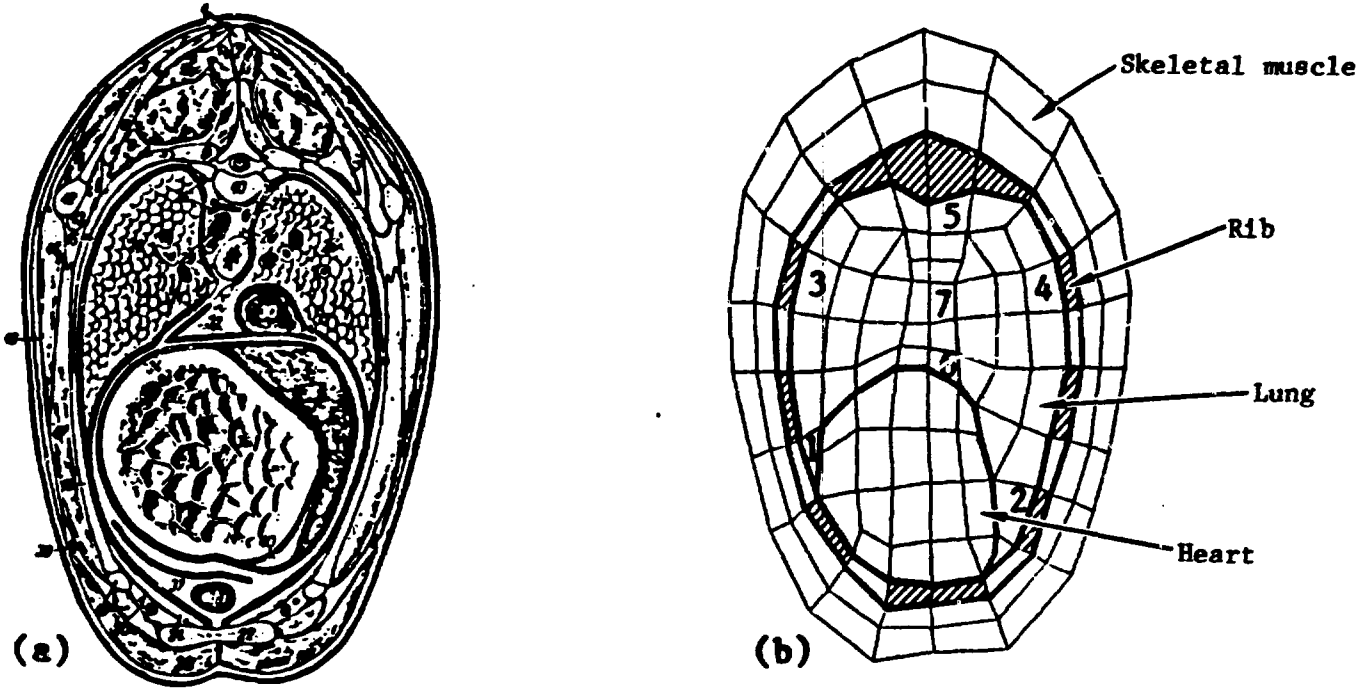

Figure 5-1. The anatomical cross-sectional view and the two-dimensional finite element model.

to understand the influence of rib cage representation on the ITP response to blast wave a parametric study with different rib cage representation has been carried out.

Figure 5-2 (a) and (b) shows the closed-ring and segmental type rib representations, respectively. For the segmental type rib cage three kinds of materials are used, namely, bony rib, muscle, and cartilage. The elastic moduli of the cartilage are hypothetically chosen to be ten times that of muscle. Figure 5-3(a) shows the intrathoracic responses for various rib cage representations. Curve 1 is the response with closed-ring bony rib. Curve 2 is the case with segmental rib composed of muscle and bone. Curve 3 is the case with closed-ring representation, but with cartilage as material. Case 4 is of segmental representation of muscle and cartilage. Case 5 is a closed-ring representation of muscle only. It appears that, except for curve 1, all the rest respond in similar frequencies, but with varying amplitudes. The response of case 1 is not reasonable due to the overexaggerated rib cage strength. Among the rest, case 5 responds most similarly to experiments measured with clear sequential oscillation (compression → tension → compression at reducing amplitude). It appears that modeling with bone material deviates the ITP prediction from experimental measurements. This could imply that at an early transient period most of the wave loading entered the lung through muscle layers.

The corresponding displacement histories of the chest wall (point A of Figure 5-2) is also shown as Figure 5-3(b). The inward displacement of case 5 reaches 0.7 cm at 12 ms. For cases 2, 3, and 4 the displacements fall in the range of 0.4-0.6 cm at 7-10 ms. For case 1 the closed ring rib structure is equivalent to a very effective protective shell. Its rigidity probably well protects the lung inside. Therefore, the lung appears to be only slightly disturbed as compared to other cases.

5.2.3 Material Constants

Measurements of esophageal pressure responses to blast wave loading indicates that there is strong damping. It first rises to a peak pressure value (compression) then falls to a negative phase (tension) with much smaller amplitude and increased period time duration. Viscoelastic material

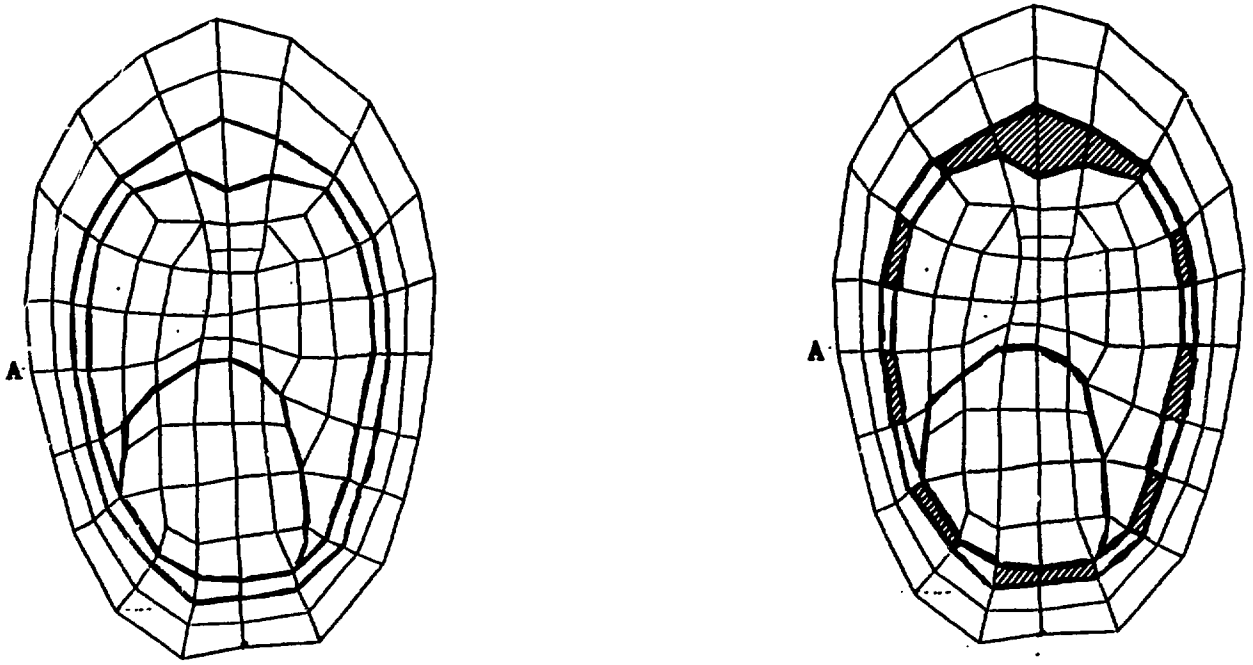

(a) Closed-ring type rib cage

(b) Segmental type rib cage

Figure 5-2. The two-dimensional rib cage representation

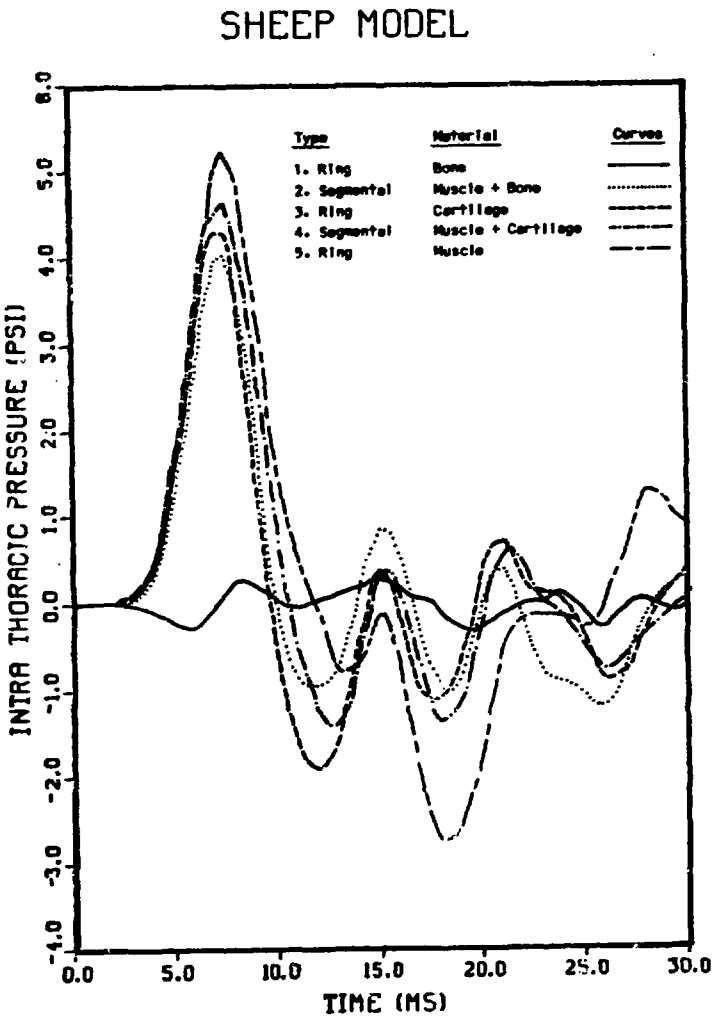

(a) ITP responses (Station 7) of various rib cage representation

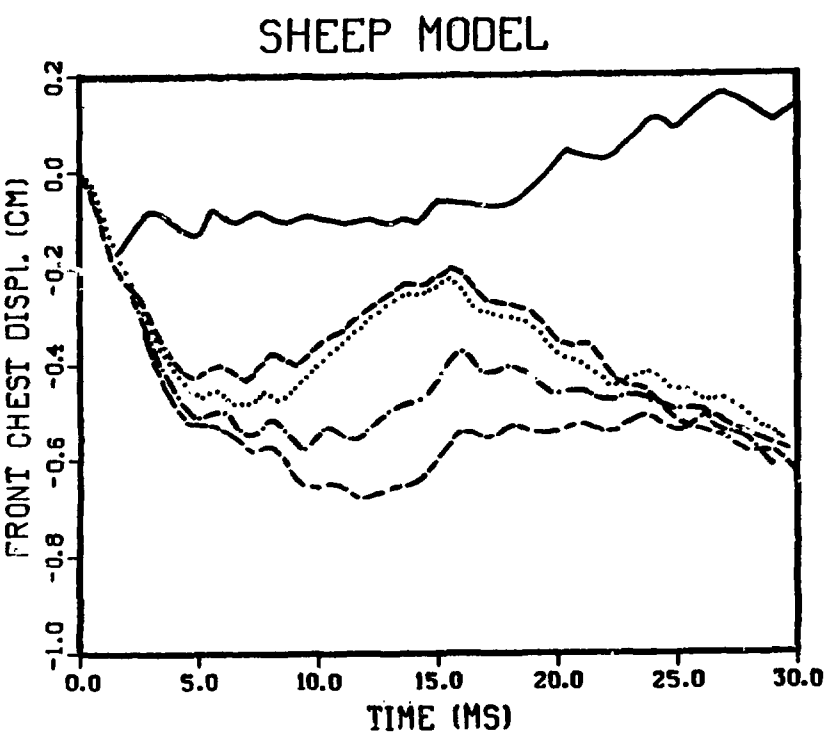

(b) Front chest displacement of various rib cage representation

Figure 5-3. Responses of the two-dimensional model with different rib cage representation.

description is one of the damping mechanisms causing such responses. The 2-D model consists of four major organs. For each organ material, to describe its stress-strain relationship, however, six constants are needed even for the simplest representation. They can be written [by choosing NG = NK = 1 in Eqs. (21) and (22) of Sec. 3] as:

$$K(t) = K_0 + K_1 \exp(-t/\lambda) \qquad (1)$$

$$G(t) = G_0 + G_1 \exp(-t/\beta) \quad . \qquad (2)$$

In Eq. (1), K(t) represents the bulk modulus at the current time t, K_0 represents that when time becomes infinity, and $K_1 \exp(-t/\lambda)$ denotes the exponentially relaxing part of the bulk modulus. For a given strain applied at normalized time $(t/\lambda) = 0$, it is K_1. This term approaches 0 as normalized time (t/λ) becomes infinite. Similar notations are used for the shear modulus of Eq. (2). For the four major organs used in the 2D model, some of these quantities have been measured, but many have not. Before undertaking new experiments to determine the missing quantities, we will parametrically vary them to see which are important.

5.2.4 Sensitivity Studies of the Material Constants

The major purpose of these sensitivity studies is to determine, among the total of 28 material constants, which ones are important and which ones are insensitive. Through these studies the number of material constants is reduced to the minimum. Only the important parameters will be retained and their influences justified.

To make these studies the case of double peak blast loading with Δt = 7.6 ms (time duration between two blast peaks) is chosen. It is chosen because double peak loading provides a sensitive test on the model. This test allows us to justify the model response sensitivity in both spatial and temporal sen[illegible]ese comparisons, however, are relative in the sense that the muscle, bone, and heart are assumed to have the same material constants.

Viscoelastic Description of Muscle, Bone, and Heart - Figure 5-4 shows the two model ITP response curves under the given double peak blast loading. The two very close response curves show that the model is insensitive to the

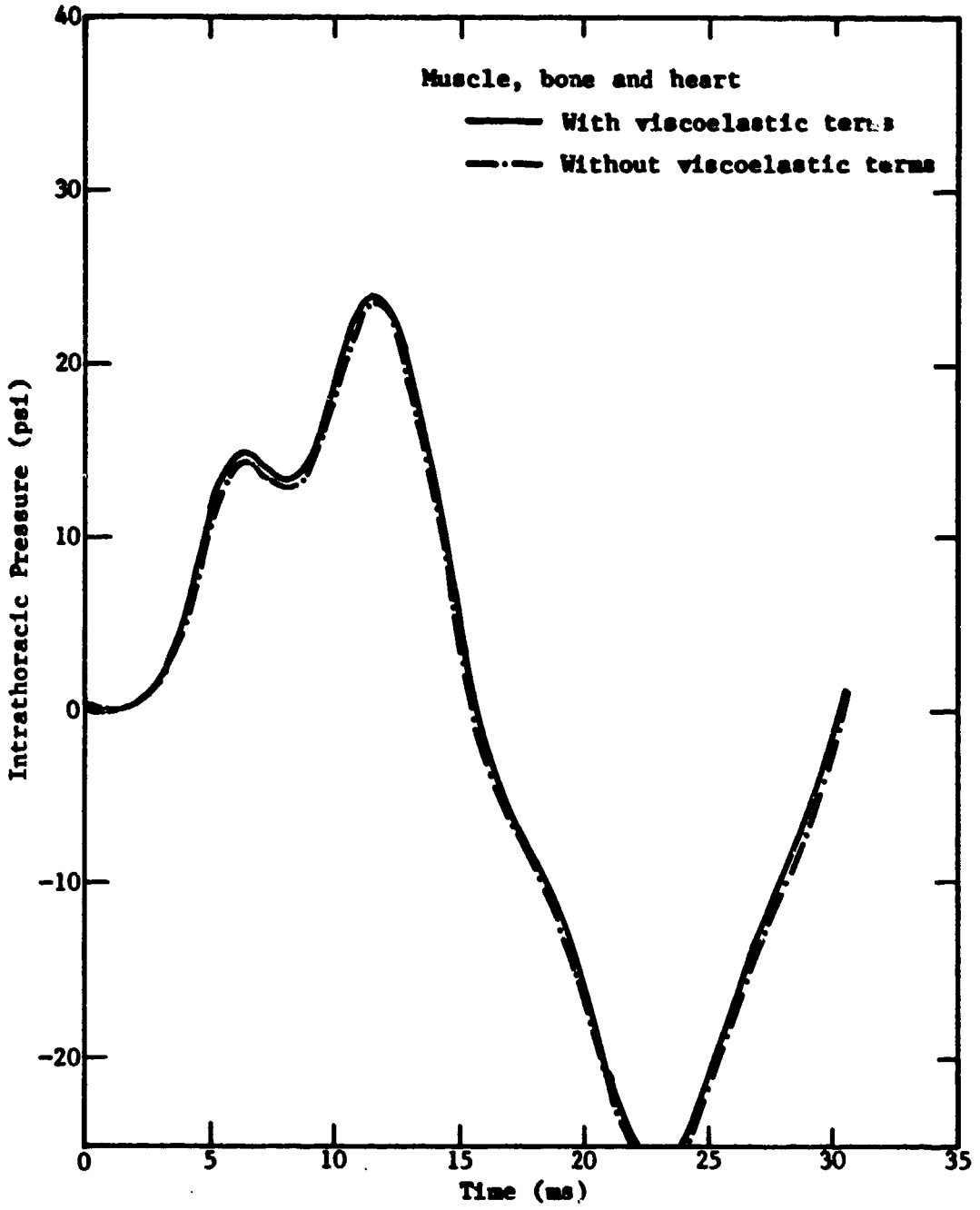

Figure 5-4. ITP response curves for cases with and without viscoelastic terms for muscle, bone, and heart.

viscoelastic description of the three surrounding organs. Compared to the lung material, these three have bulk moduli close to that of water. Whereas the lung has a bulk modulus close to that of air. These three materials are incompressible when compared to the lung. Therefore, contribution from the viscoelastic description of these three surrounding organs in the decaying feature of the lung ITP response could be minimal.

Shear Moduli of the Muscle, Bone, and Heart - Magnitude of shear moduli of these three organs are varied to compare the effect on the model ITP response. It appears to be an important parameter. Figure 5-5 shows these comparisons. Among these comparisons, bulk moduli K_0 are kept at 1.0×10^{10} dyne/cm^2. The case with $G_0 = 1.0 \times 10^4$ dyne/cm^2 is the baseline case. The case with $G_0 = 1.0 \times 10^5$ dyne/cm^2 shows little difference from the baseline case. But as we keep increasing G_0, the difference in the model ITP response becomes evidient. These cases show smaller amplitude and increased frequency. This is due to the model becoming less flexible.

Bulk Moduli of the Muscle, Bone, and Heart - Magnitude of bulk moduli of these three organs are varied to understand their effects on the model ITP responses. In this study shear moduli of these three organs are kept constant at 1.0×10^4 dyne/cm^2. Bulk moduli of $K_0 = 1.0 \times 10^{10}$ dyne/cm^2 are used as the baseline case. There is no significant change in the ITP response as we reduce the bulk moduli down to 1.0×10^8 dyne/cm^2 (see Fig. 5-6). Further reduction of K_0 results in slower ITP responses and larger amplitudes. The extreme case with $K_0 = 1.0 \times 10^6$ dyne/cm^2 represents the case when bulk moduli of these three organs are of the same size as that of the lung.

Bulk Modulus of the Lung - Bulk modulus K_0 of the lung is varied to study its influence on the ITP response, while the shear modulus G_0 is kept constant at 1.0×10^4 dyne/cm^2. For muscle, bone, and heart the baseline values of 1.0×10^{10} and 1.0×10^4 dyne/cm are used for the bulk and shear moduli, respectively. Figure 5-7 demonstrates these changes. It appears that bulk modulus of the lung K_0 is a crucial parameter. Decrease by one order of magnitude results in smaller amplitude and slower starting time in the ITP response curve, while increase by one order of magnitude results in very pronounced amplitude and earlier starting time in the ITP response curve. Increased bulk modulus means a stiffer lung with higher wave propagation speed ($c = \sqrt{K/\rho}$ for

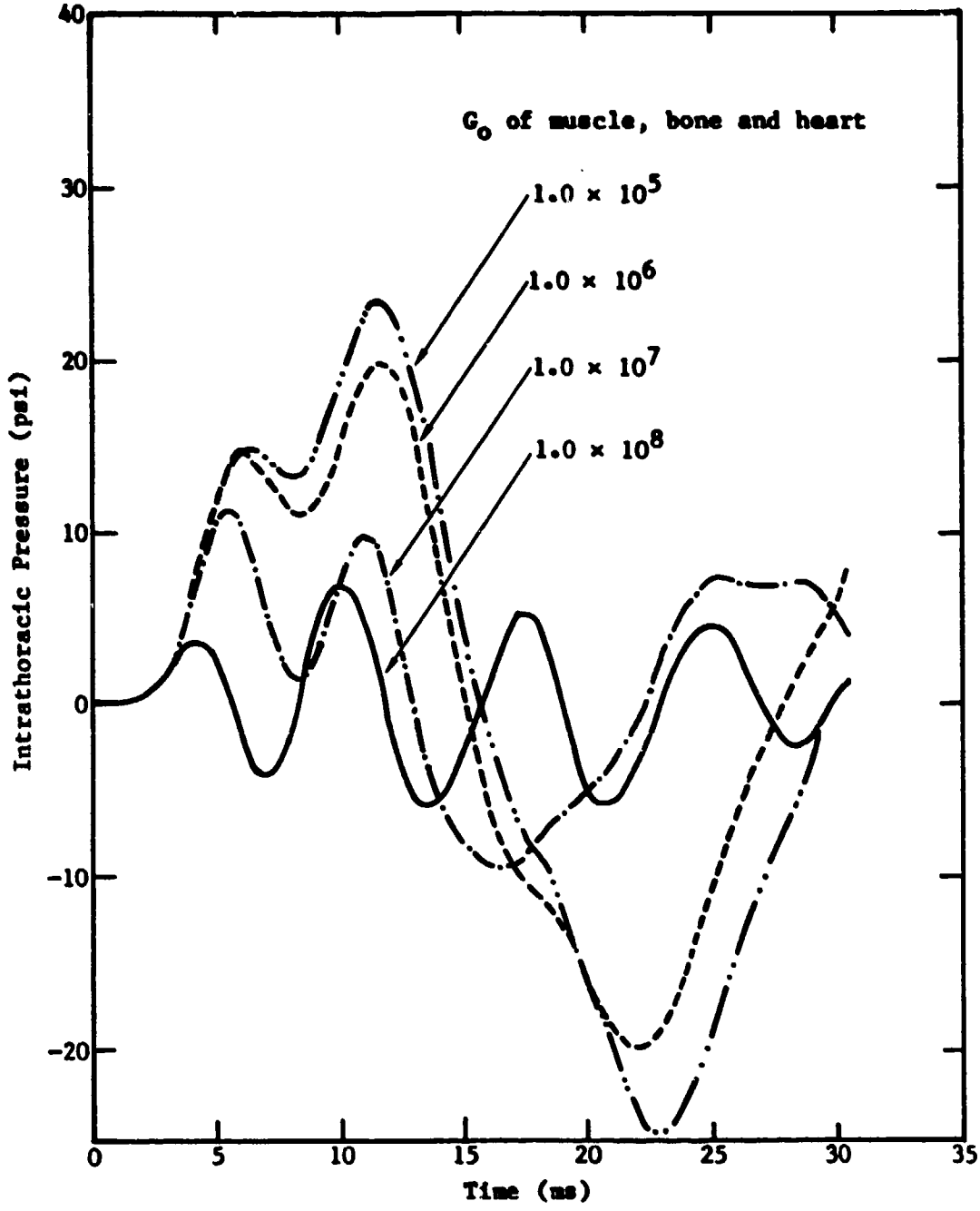

Figure 5-5. ITP response curves at varying shear moduli for muscle, bone, and heart.

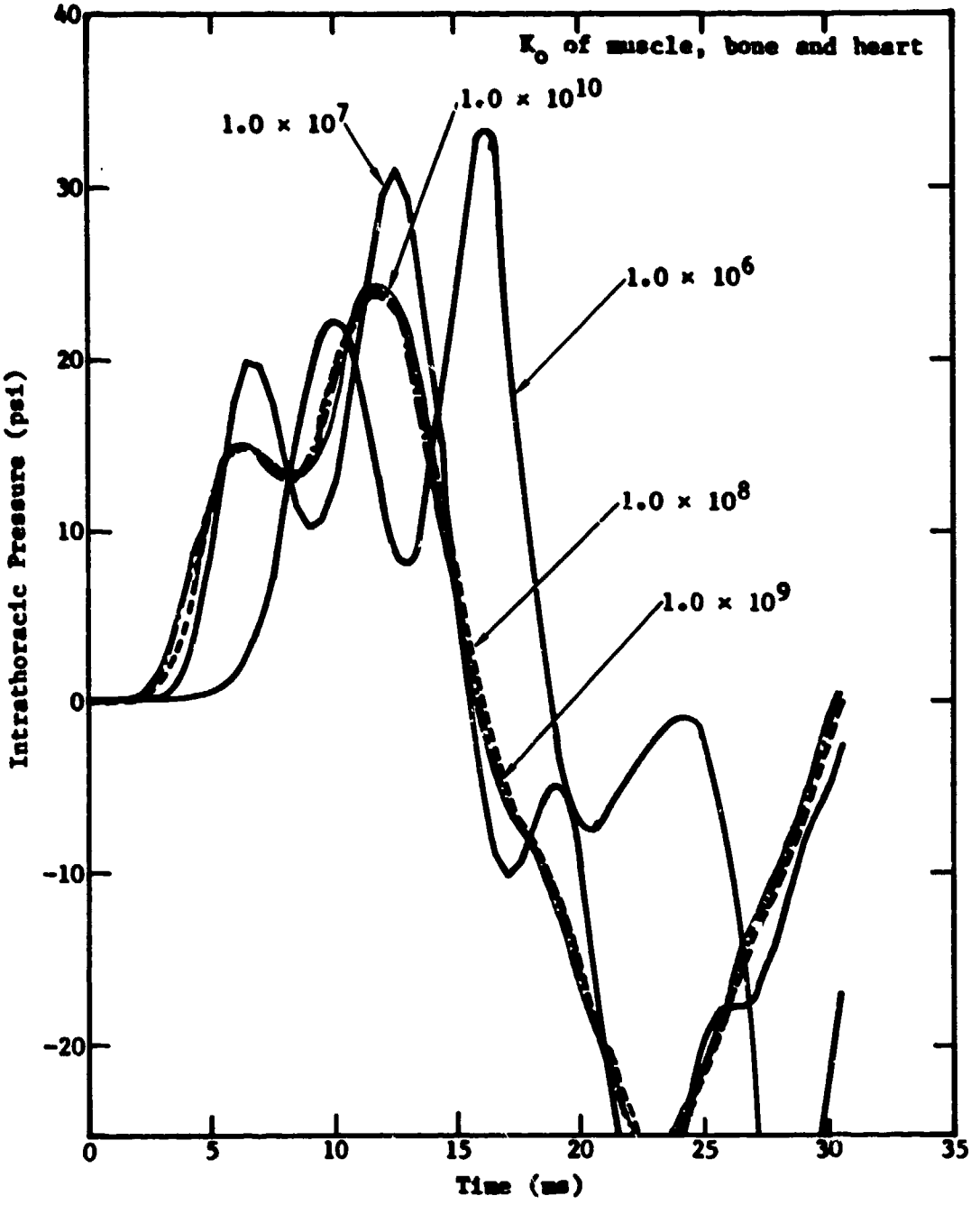

Figure 5-6. ITP response curves at varying bulk moduli for muscle, bone, and heart.

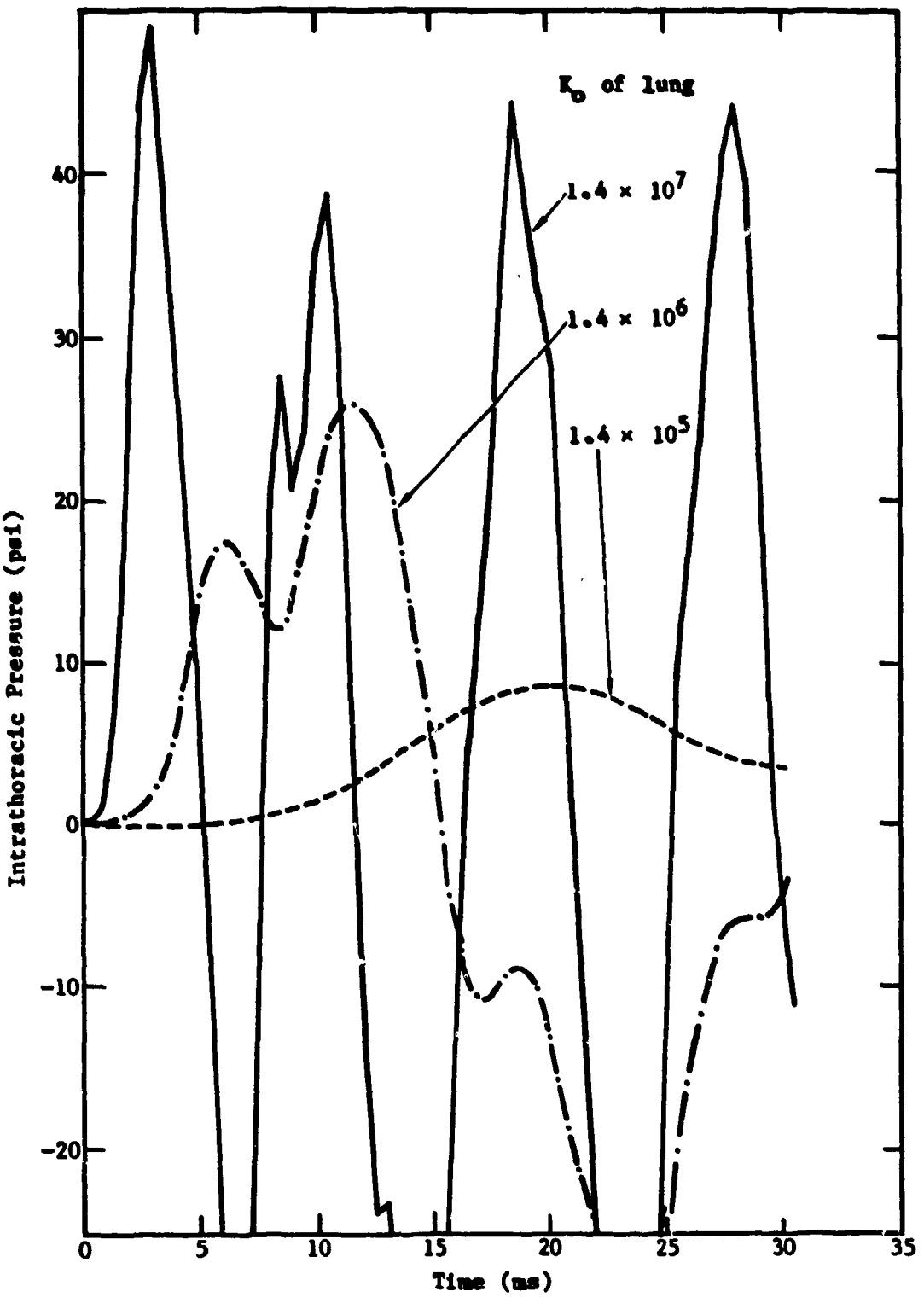

Figure 5-7. ITP reponse curves at varying bulk moduli for the lung.

compression wave). Under a given disturbance, the lung responds in a more vigorous way, while the decreased bulk modulus results in an opposite w...

Viscoelastic Description of the Lung - Experimental esophageal pressure measurement shows strong damping in the lung overpressure response curve during air blast exposure. Damping came from different sources. From the material point of view, the viscoelastic nature of the lung material could contribute to the damping of lung overpressure response.

The specific viscoelastic description of the lung under dynamic blast wave loading is unknown at this time. Assumed values are used for the relaxation moduli to understand their effect on the ITP response of the lung under dynamic blast wave loading. Unlike the muscle, rib, and heart, the viscoelastic description of the lung has been shown to reduce the peak ITP and the rarefaction of the response that follows (see Fig. 5-8). There may be other damping mechanisms associated with the intrathoracic pressure responses to blast wave incidence.

Effective Muscle/Rib and its Calibration by Static Loading Experiments - The structure and geometry of the lung and rib cage are three-dimensional in nature. Under blast loadings the kinematics and deformation dynamics of the rib cage and the body are expected to be three-dimensional as well. To account for the structural rigidity of the rib cage in a two-dimensional model we have lumped its rigidity to the material property of the muscle layer and call it the effective muscle/rib. The value of this effective property can be obtained from static loading experiments.

At the present time a system parameter identification scheme is used. Within the context of the sensitivity study, various combinations of bulk and shear moduli have been tried to determine the set of parameters which makes the best ITP prediction when compared with a group of experimental measurements. In other words, the mechanical description for the effective muscle/rib is obtained through a series of numerical experiments. Shear modulus of 1.0×10^7 dyne/cm^2 and bulk modulus of 1.0×10^9 dyne/cm^2 have been found to be the pair from this comparison study. Their values, in conjunction with other elastic properties, are listed in Table 5-1.

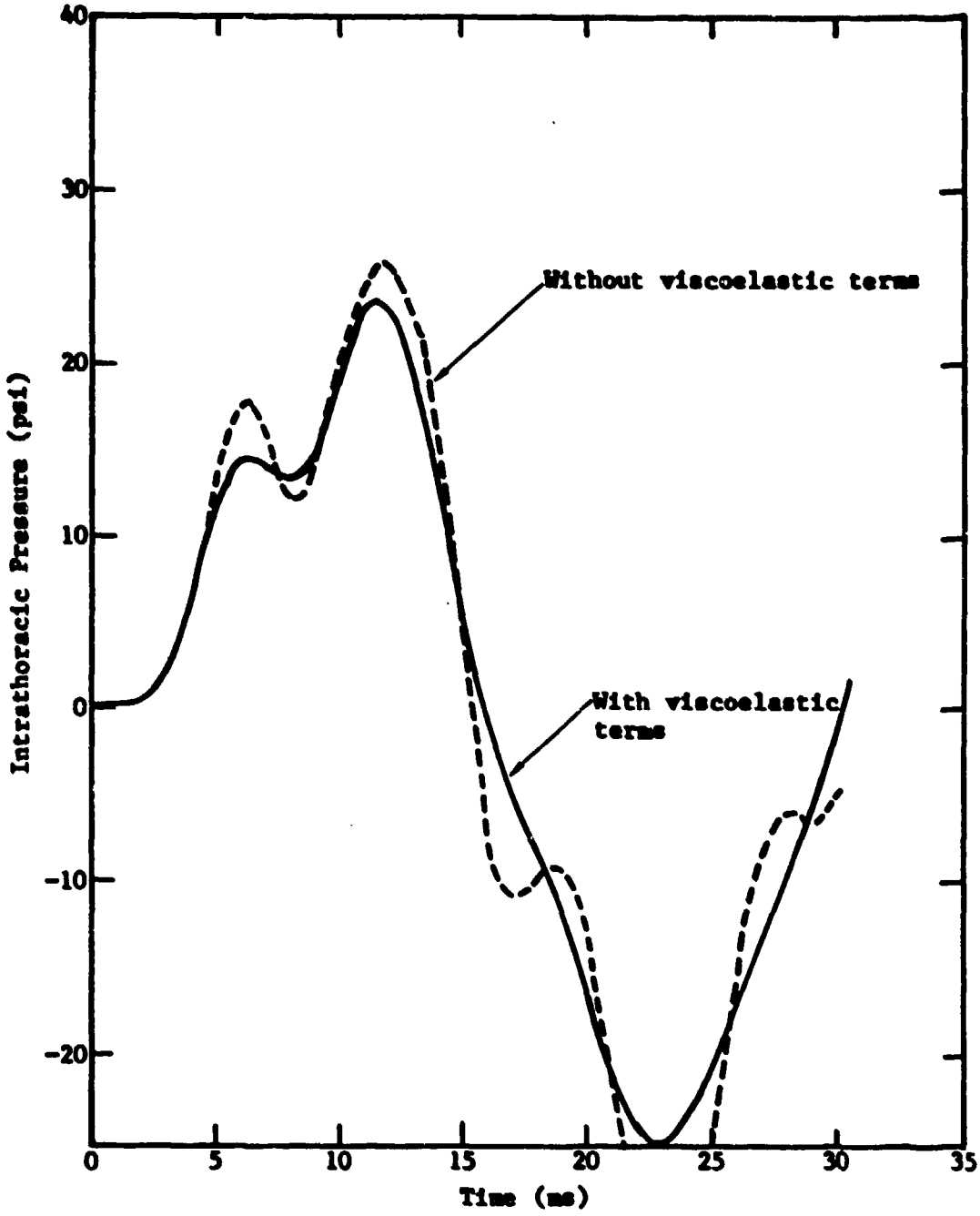

Figure 5-8. ITP response curves for cases with and without viscoelastic terms for the lung.

Table 5-1. Material Properties Used in Cross-Section Model

Organ	G_0 (dyne/cm^2)	K_0 (dyne/cm^2)	ρ (gm/cm^3)
Lung	1.0×10^4	1.4×10^6	0.2
Muscle	1.0×10^7	1.0×10^9	1.0
Rib	1.0×10^7	1.0×10^9	2.0
Heart	1.0×10^6	1.0×10^{10}	1.0

Static loading experiments can be done to confirm the effective muscle/rib description. At this time, preliminary work is done on the model to justify this type of experiment. Static loading is applied on the model chest wall with the back constrained and the chest wall deflection is predicted.

Figure 5-9 shows the body configurations of the unloaded and loaded states at various degrees of static pressure. The deflection of point A under different static loadngs is plotted in Figure 5-10(a). The normalized deflection of point A (with respect to the cross-section dimension of AB) is plotted in Figure 5-10(b). The result shows that for low pressure static loading (below 4 psi) the deflection is in a reasonable range.

5.3 COMPARISON WITH EXPERIMENTAL DATA

5.3.1 Blast Loading Description

When an incident blast wave front (compression) reaches the body surface a sequence of subtle interactions can follow. Depending on the relative impedance, a portion of the wave energy transmits into the body and the other portion reflects from the interface. The reflected component is added to the newly arriving blast wave to result in increased loading strength. At the same time different types of waves (shear, surface) can be set into motion. In accordance with the dynamic equilibrium among external forces, system inertial, elastic and damping forces the body deforms and the body surface moves. At a given instant, the blast loading on the body surface, in fact, depends on the entire past blast-body interaction history.

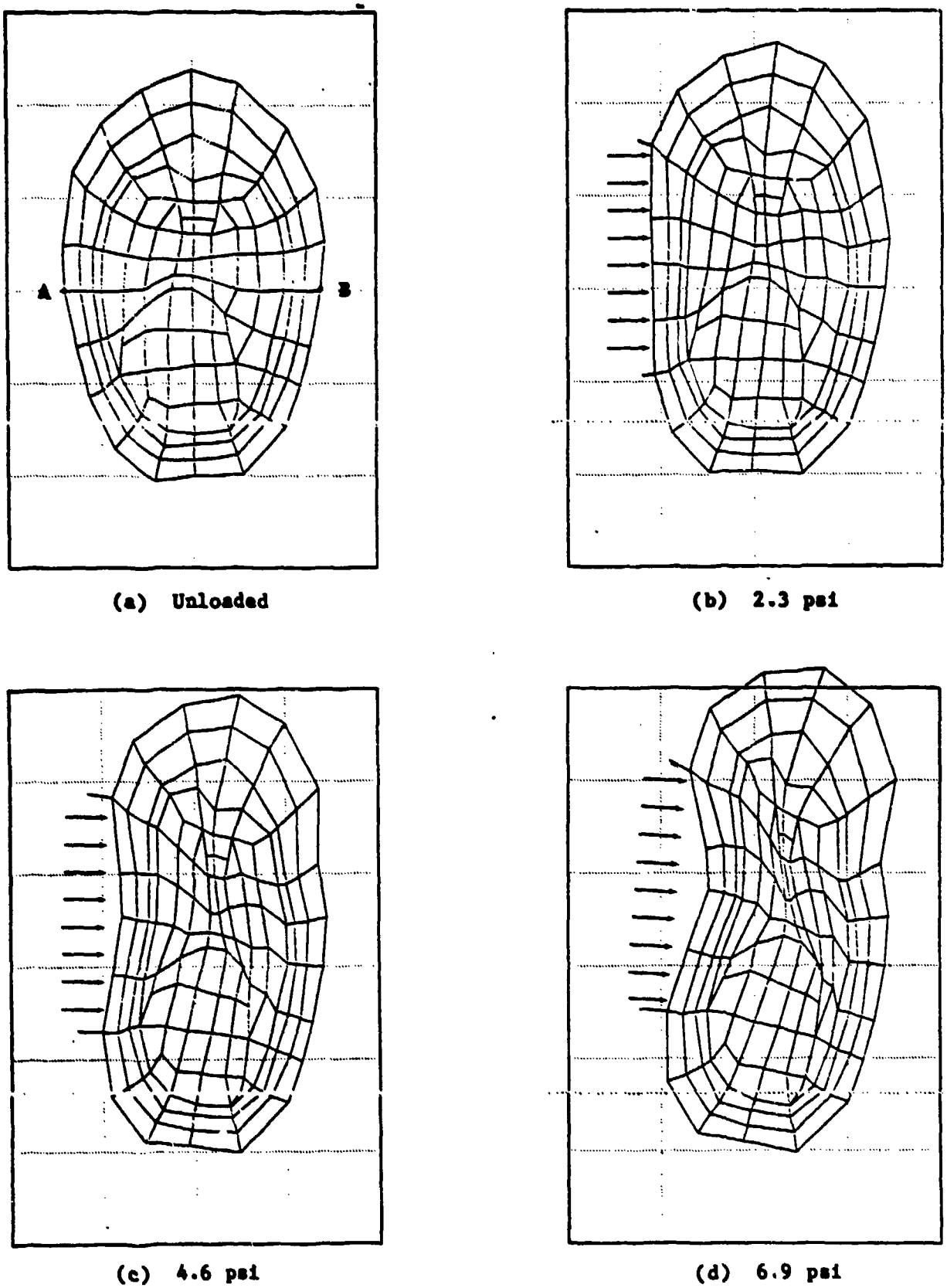

(a) Unloaded

(b) 2.3 psi

(c) 4.6 psi

(d) 6.9 psi

Figure 5-9. Deformed configuration of the two-dimensional FEM model under prescribed static loadings.

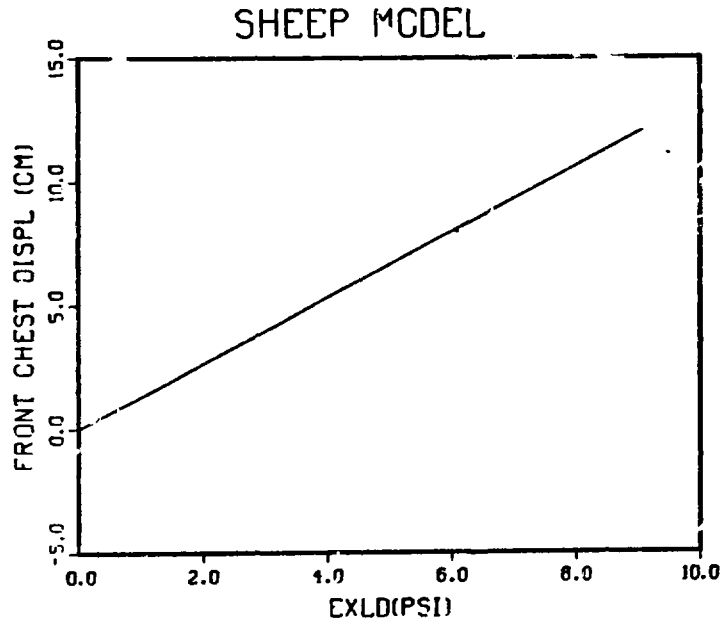

(a) Displacement - external static pressure loading

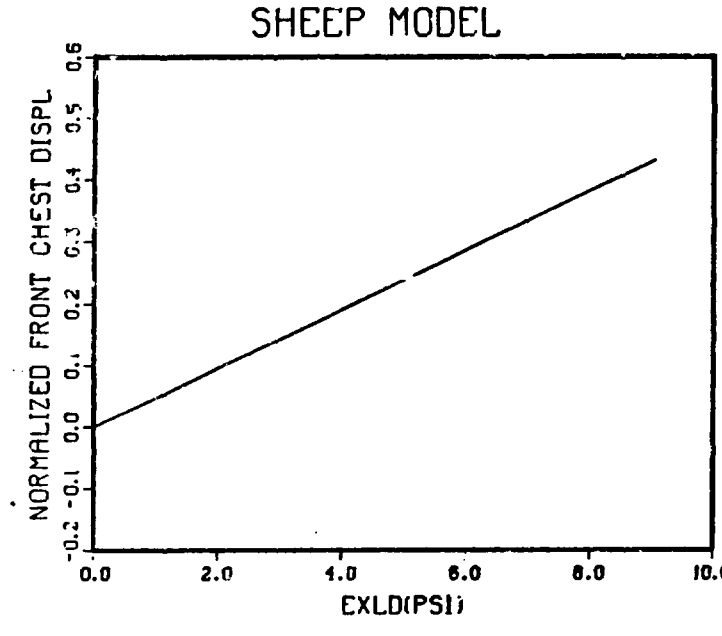

(b) Normalized displacement -external static pressure loading

Figure 5-10. The chest wall displacement and external static pressure loading relationship.

The blast loading description is best described in terms of an impulse ratio. The impulse ratio is defined to be the factor by which impulse (time integration of pressure history) is increased at the body surface over that of the free field value. Based on the experimental data reported in Reference 20, it is assumed that the impulse ratio at the body surface can be expressed as a function of external peak blast pressure. Figure 5-11(a) illustrates the derived values from experimental data and the hypothetically assumed linear relationships between impulse ratios and external peak blasts. Data from the experiments are marked with X. The hypothetical linear relationship is obtained by extrapolating the two experimental values. Division of zones A, B and C are illustrated in Figure 5-11(b).

Zone A is the portion of the body surface directly facing to the incident wave. Between 0 and 45 psi blast peak pressure the impulse ratio varies linearly from 1 up to 2.8. The increased impulse ratio accounts for the effect of wave reflection from body surface and the resulting higher loading. Zone C is at the back side of the body away from the direction of wave arrival. When the free field blast pressure is 3 psi the impulse ratio derived from experimental data is found to be 0.75. In Zone C it is assumed that the ratio is 0.75 for peak pressures less than 10 psi and 1 for blast pressure higher than 10 psi. Zone B is the body surface normal to the direction of wave arrival. The impulse ratio in Zone B is assumed to be the average values between Zone A and Zone C. This body surface blast loading is used in all the studies in this report.

5.3.2 Spatial Variation of Overpressure Histories

Figure 5-12(a) is reproduced from experimental results performed at the Lovelace ITRI. A sheep is exposed right side on to blast waves generated with 32 lb. of TNT charge at 44.4 ft range and 8.0 ft height of burst. The free field blast pressure and the intraesophageal pressure taken at the seventh intercostal are shown as chain-dotted and chain-dashed lines, respectively.

Figure 5-12(b) shows the resulting lung overpressure responses as predicted by the two-dimensional sheep thorax model. Each of the seven curves denotes overpressure history occurred at a different location in the lung [see Fig. 5-11(b)]. It is clear that the incident wave arrives at different

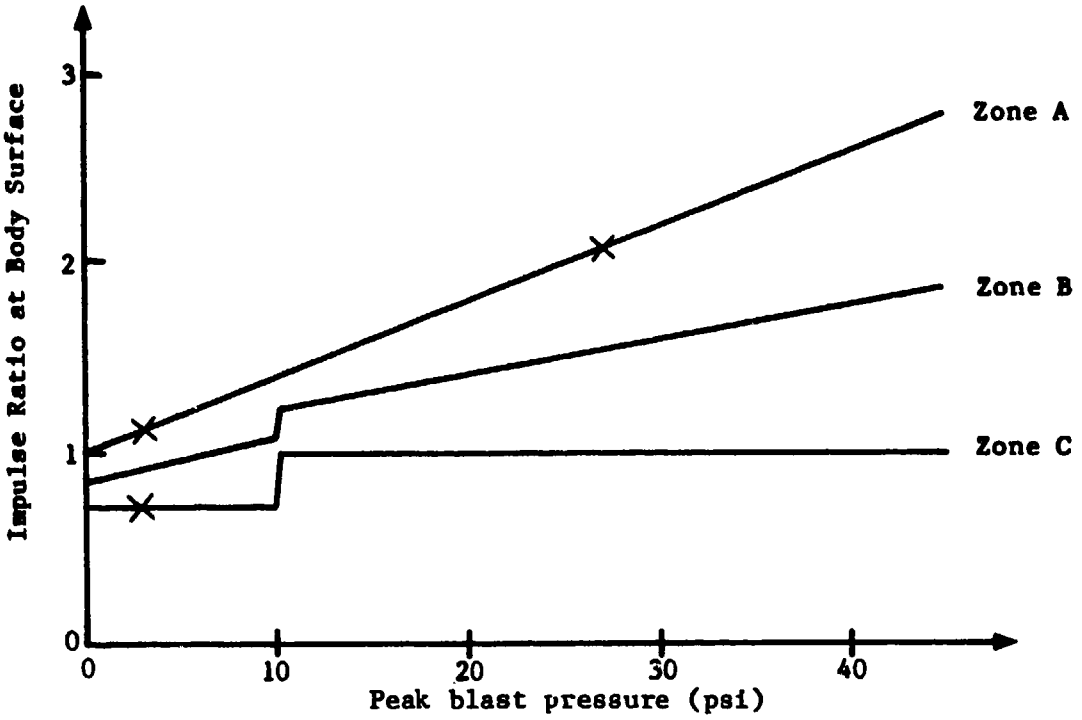

(a) Effect of experimental derived and hypothetical impulse ratios at various peak blast pressures on Zones A, B and C

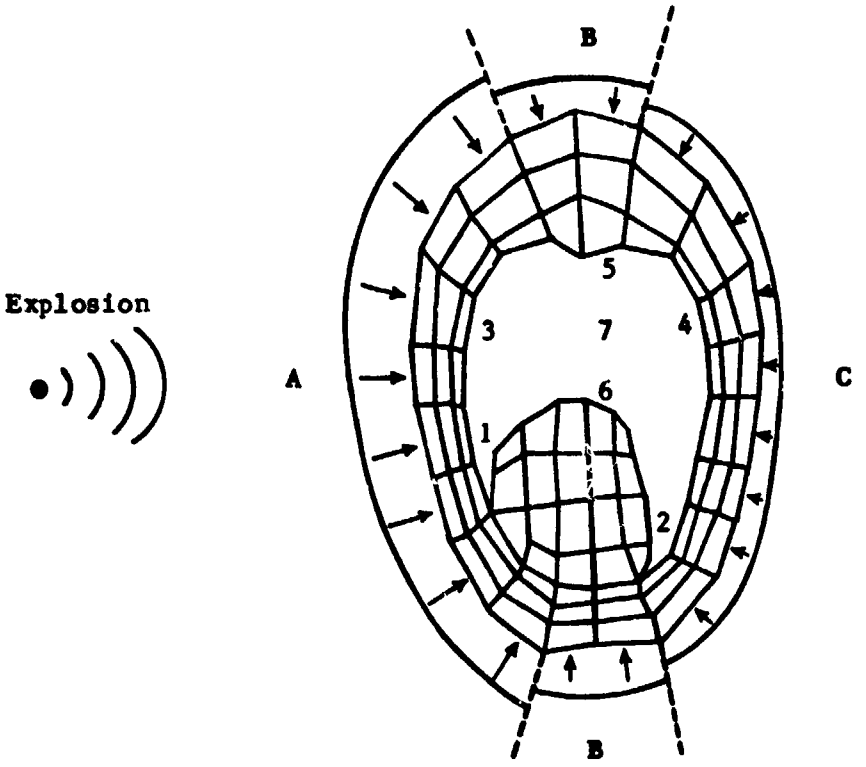

(b) Division of body surface into Zones A, B and C with respect to the explosion center

Figure 5-11. Experimental derived and hypothetical impulse ratios at various peak blast pressures.

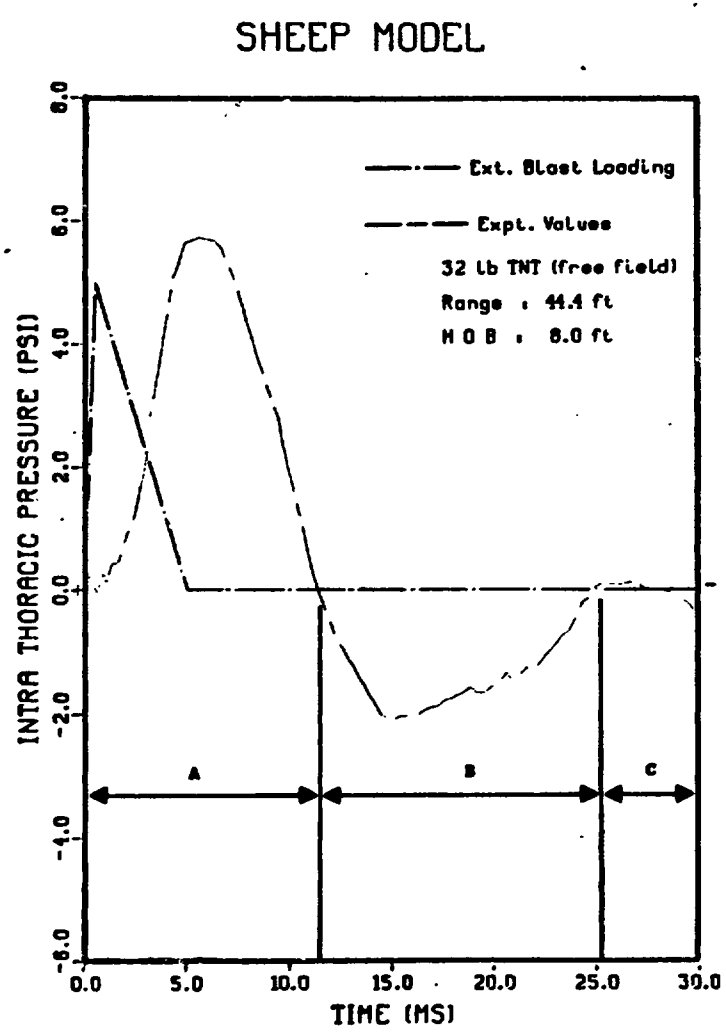

(a) Experimental measured free field blast pressure and sheep's esophageal pressure history taken at the seventh intercostal

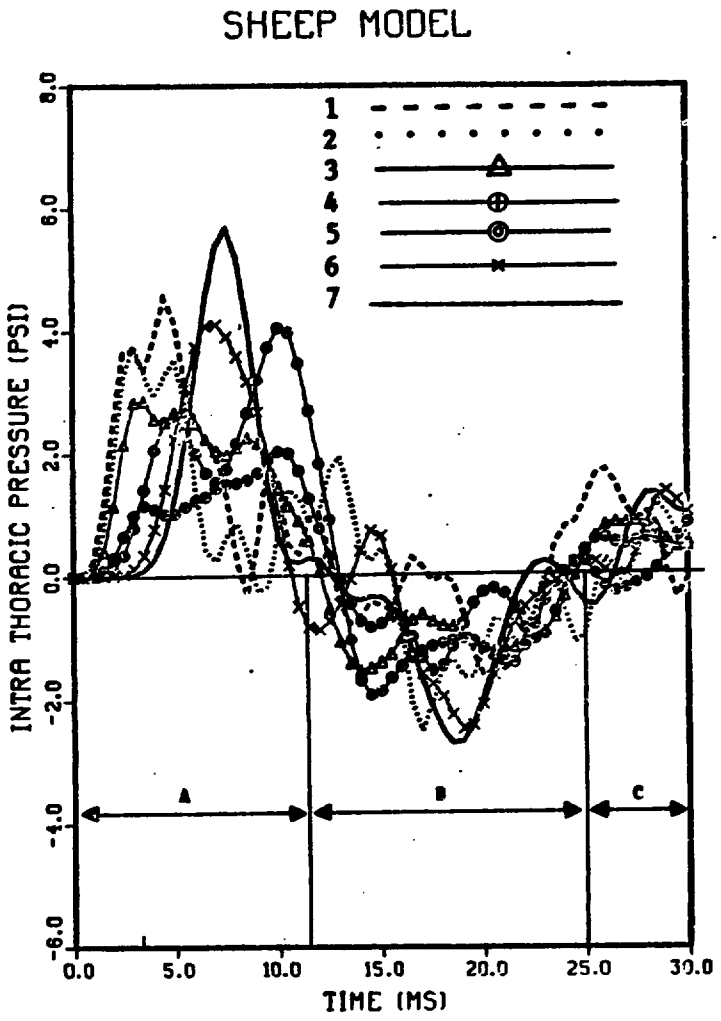

(b) Prediction of lung overpressure history at various stations

Figure 5-12. Experimental free field blast pressure, esophageal pressure and overpressures predicted by the two-dimensional FEM model.

stations at different times. The overpressure experienced by different parts of the lung is also different in its temporal variation on account of the irregular geometry, complex structure, as well as the dynamical behavior. It is seen that station 1 is the first to "feel" the disturbance followed by station 2. The station 1 is able to experience a higher overpressure and a wider time span due to the fact that higher impulse is delivered to its neighborhood. Station 3 is the third to "feel" the incident wave. Compared with station 1, station 3 experiences a wider time span, but lower peak pressure, although both are near the right body surface under increased loading. This is because station 1 is located in a narrow corner between skeletal muscle and the heart. When the reflected component from the heart is superimposed to the incident wave, a higher overpressure can occur at this region. Most of the wave passing by station 3 is, however, able to penetrate into the lung easier.

Station 4 is the fourth, among the seven, to know the pressure wave incidence. It rises to 1 psi at 4 ms yet experiences a second peak of 4 psi at 10 ms. This second peak is caused primarily by the arrival of the pressure wave which already passed stations 3 and 7. Station 5 is the fifth to "know" due to the fact that it is deeper from the body surface and also has a lower pressure applied at that surface. Station 6, which is located behind the heart, is the next to respond. Station 7, at a location approximating the center of the lung where the esophagus sits (we have neglected the mediastinum, blood vessel, and soft tissue there), is the last one to know the pressure arrival yet reaches a maximum value of 6 psi at 7 ms.

Figure 5-12(a) also shows the intraesophageal pressure history taken at the seventh intercostal from sheep experiments. Compare with this experimental data, all prediction curves at seven stations show higher frequencies, but similar average response with the removal of high frequency components. To make the comparison we divide the first 30 ms into three time periods on both Figure 5-12(a) and (b):

1. Time period A: from 0-12 ms
2. Time period B: from 12-25 ms
3. Time period C: from 25-30 ms

It is seen that during the time period A all the seven stations experience overpressure due to the arrival and reflection of pressure waves in different ways at different times. During the time period B, however, almost all of the seven stations are under different degrees of dilation. The physical interpretation is that the whole lung is progressively under recoil tension after the compression in the period A. The decreased amplitudes and retarded oscillation frequencies are attributed to the damping in the lung. After 25 ms all the response curves in the time period C show their trend to bounce back to the compression phase with less available energy. Compared with esophageal pressure history measured from the experiments, prediction curves of Figure 5-12(b) show that there is spatial differences of lung overpressure responses to external blast incidence. Locally, different response history will result in different damage history. Therefore, the interpretation of esophageal pressure should be carefully justified as it is commonly used as an indication of the whole lung uniform response in experimental works as well as lumped-parameter model prediction.

5.3.3 Single Peak Exposure

Data of external blast loading taken from WRAIR/LOVELACE ITRI experiments are applied on the two-dimensional FEM model to predict lung overpressure responses. Prediction of lung overpressure histories at the center of the lung, approximately where the esophageal pressure is taken, are then compared with experimental measurements.

Figures 5-13 through 5-16 are comparisons of the four different loading cases from TNT free field experiments performed during September and October of 1981. In each case the model prediction is overlayed on the experimental esophageal pressure recording for easy comparison. The comparisons show that the two-dimensional model prediction and the experimental measurements are of good qualitative agreement. Similar to the case as demonstrated in Section 5.3.2 and in Figure 5-12, the overpressure responses are predicted to be different at different parts of the lung. Without the availability of experimental measurements the multiple prediction tracings are not shown on Figures 3-13 through 5-16.

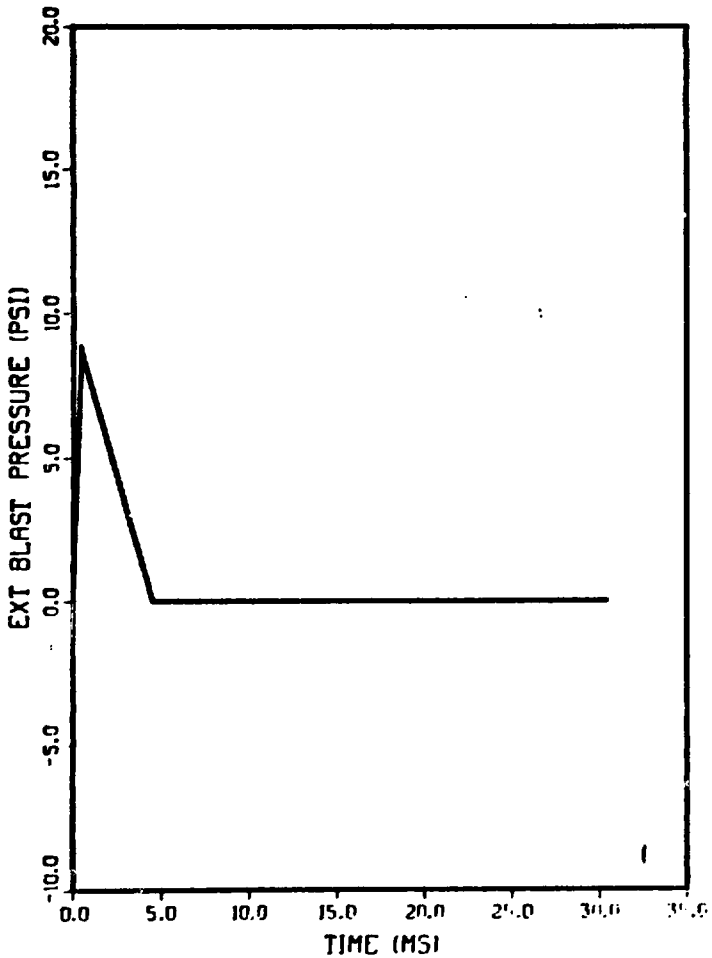

(a) Experimental measured free field blast pressure

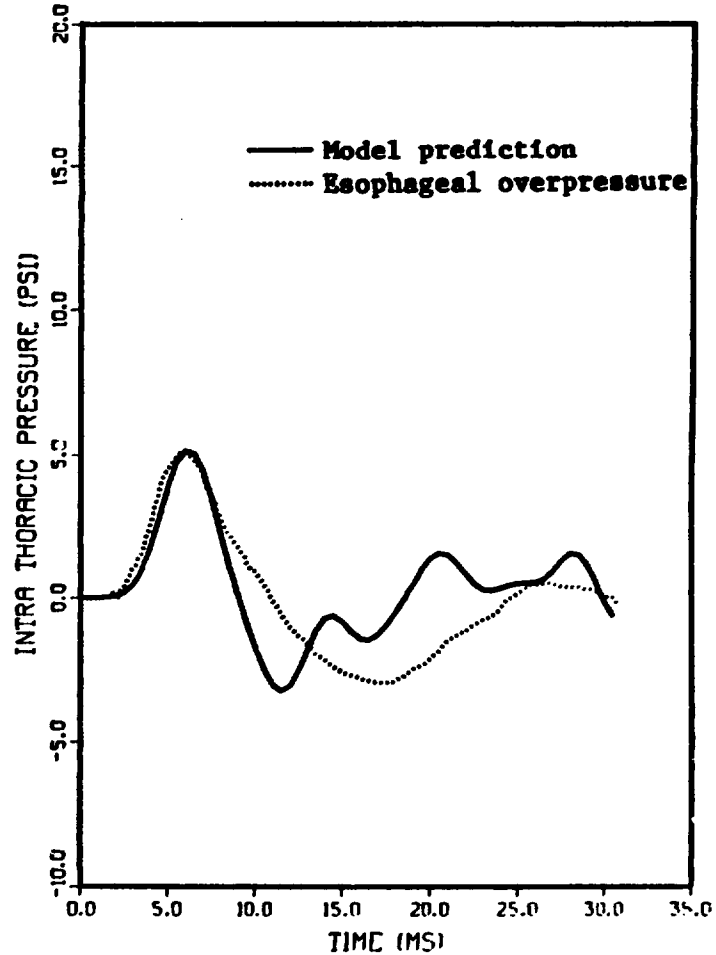

(b) Prediction of lung overpressure history and sheep's esophageal pressure history taken at the seventh intercostal

Figure 5-13. (Case 1) 8 lb TNT free field. Experimental free field blast pressure, esophageal pressure and overpressure predicted by the two-dimensional FEM model.

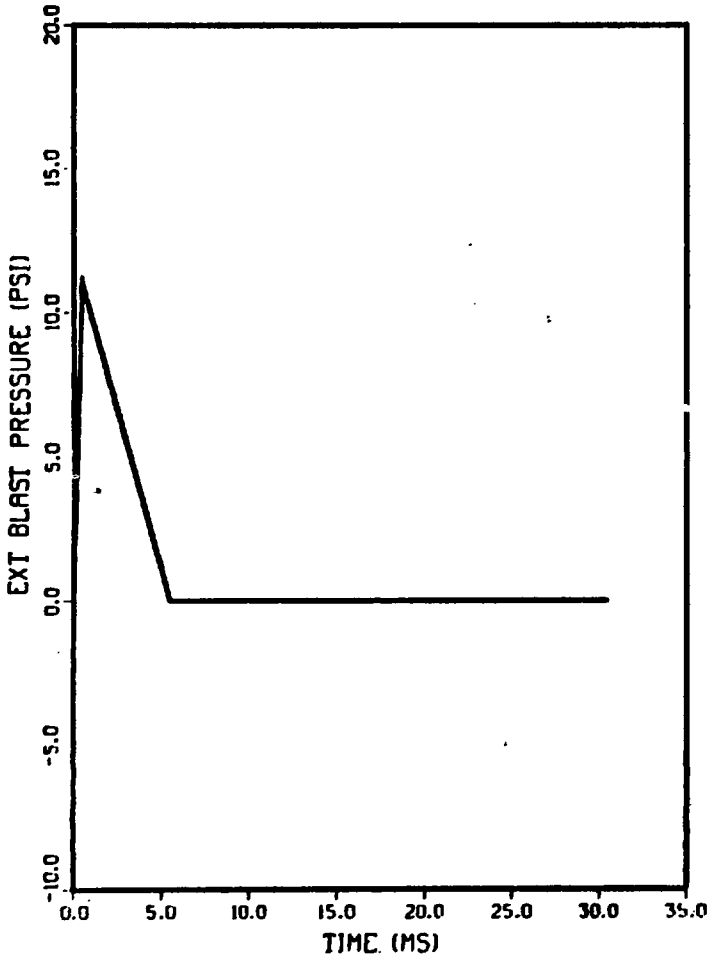

(a) Experimental measured free field blast pressure

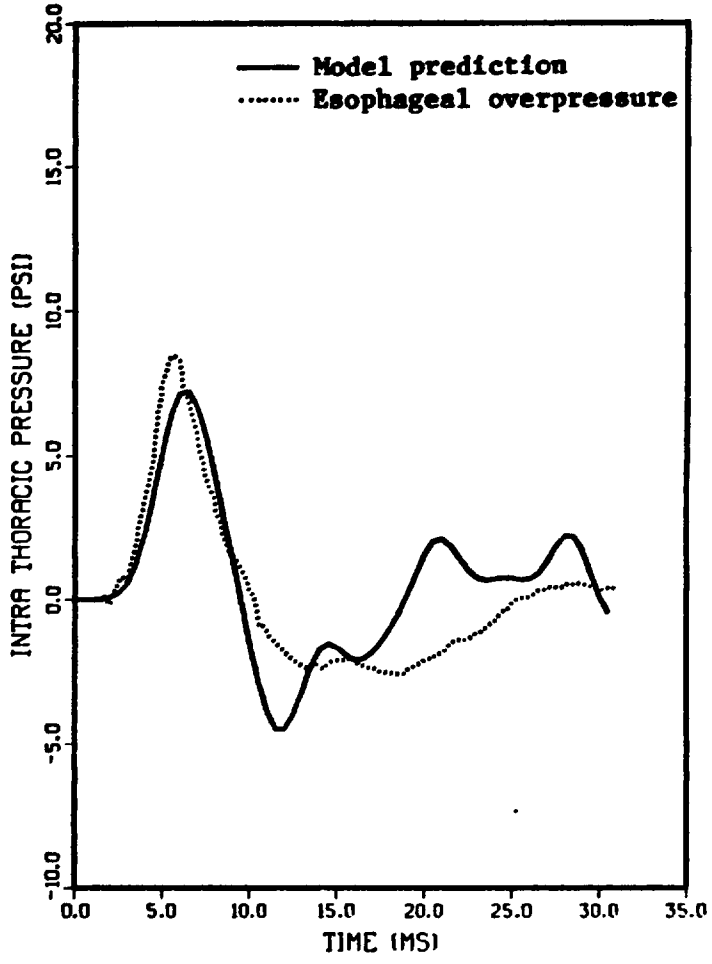

(b) Prediction of lung overpressure history and sheep's esophageal pressure history taken at the seventh intercostal

Figure 5-14. (Case 2) 16 lb TNT free field. Experimental free field blast pressure, esophageal pressure and overpressure predicted by the two-dimensional FEM model.

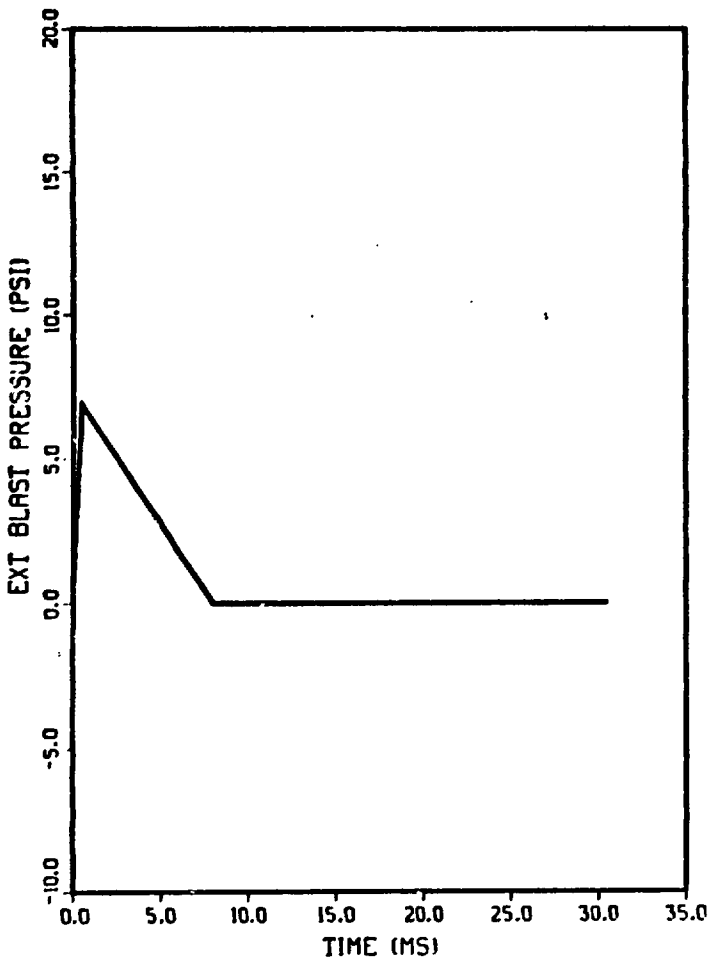

(a) Experimental measured free field blast pressure

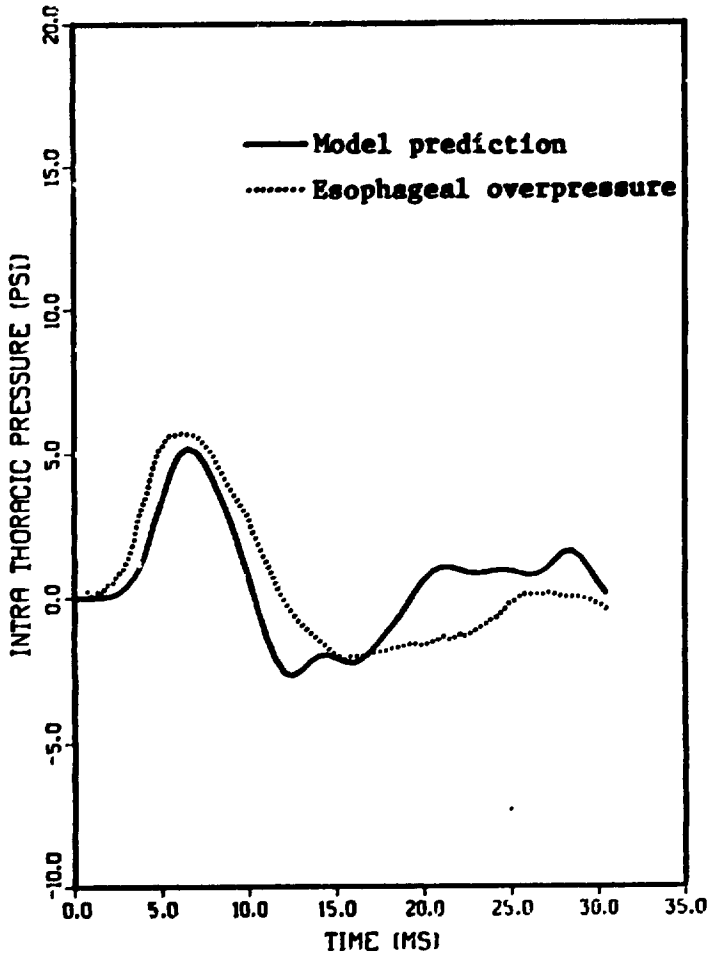

(b) Prediction of lung overpressure history and sheep's esophageal pressure history taken at the seventh intercostal

Figure 5-15. (Case 3) 32 lb TNT free field. Experimental free field blast pressure, esophageal pressure and overpressure predicted by the two-dimensional FEM model.

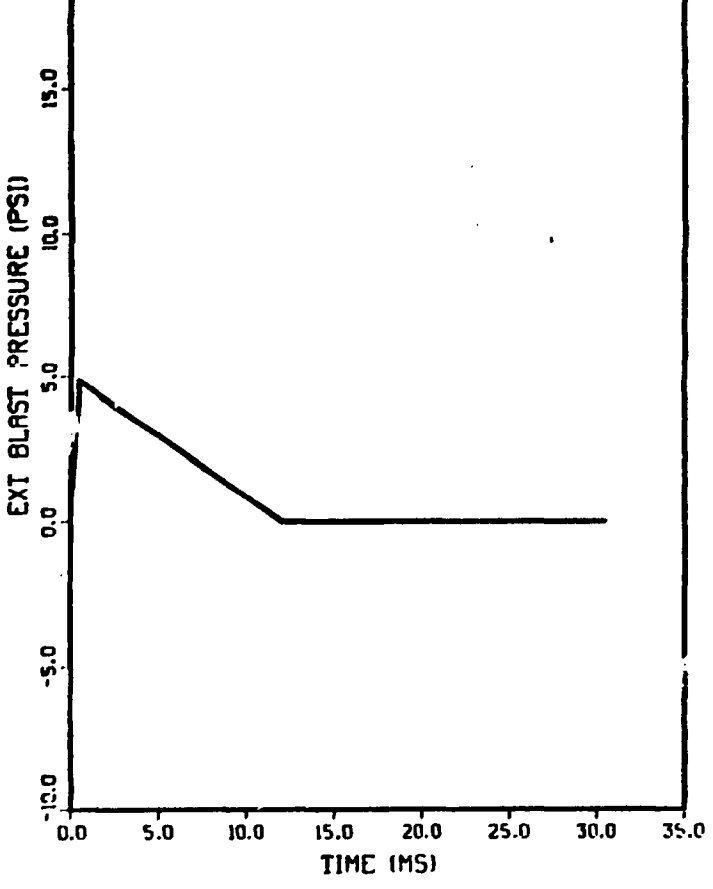

(a) Experimental measured free field blast pressure

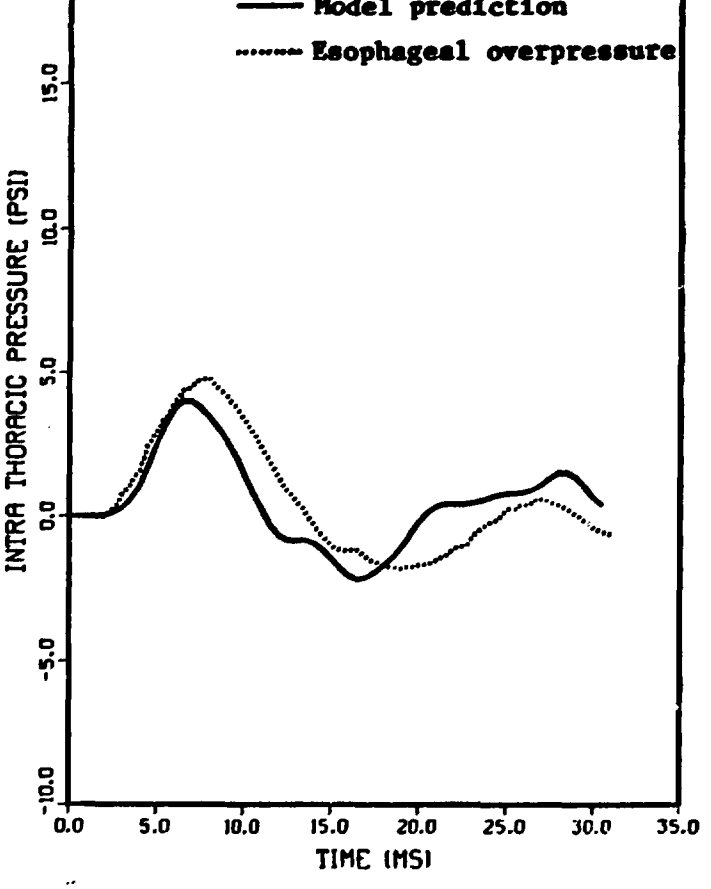

(b) Prediction of lung overpressure history and sheep's esophageal pressure history taken at the seventh intercostal

Figure 5-16. (Case 4) 64 lb TNT free field. Experimental free field blast pressure, esophageal pressure and overpressure predicted by the two-dimensional FEM model.

5.3.4 Double Peak Exposure

The double peak study was performed by the LOVELACE ITRI in October 1981 and May 1982. The purpose of the study was to investigate resonance effects when the time duration between two blast loading approaches that corresponds to the natural frequency of the structure. Experimental blast loading data with different time duration between two peaks are applied on the two-dimensional FEM model body surface to observe the lung overpressure responses. Figures 5-17, 5-18 and 5-19 are comparisons of the three cases with duration between two peak blasts Δt = 9.7, 7.6 and 3.6 ms, respectively. Similar to the previous discussion the overpressure histories at seven statons are plotted to compare with the experimental measured esophageal pressure.

In the third case (Fig. 5-19) with Δt = 3.6 ms, the model prediction does not clearly distinguish the two ITP peaks. Further refinement of the finite element mesh is needed. For the first and second cases with Δt = 9.7 and 7.6 ms (Figs. 5-17 and 5-18), model predictions compare favorably with experimental measurements. The model predictions do not seem to have enough rarefaction as experimental measurements. Typically, they have larger tension phase and continuous ripples. This is due to insufficient damping. This is to be improved in the next phase.

More comparisons of model prediction and experimental measurements are reported in Section 5.4.2 under "Isoimpulse with Different Peak Blast Pressure."

5.4 SENSITIVITY STUDIES OF THE MODEL

5.4.1 Effect of Loading Firing Sequence (temporal) and Doubling Effect Distribution (spatial)

The interaction between the incident blast wave and the deformable body is a rather complicated coupling. The incident blast wave front reaches different parts of the body surface at different times on account of its propagation in the air as well as the interaction with the deformable body. The reflection of the blast wave at the boundary also results in increased effective loading pressure. Experimental measurements and numerical simulations have been done with a solid torso model to study its interaction with the incident blast wave [20].

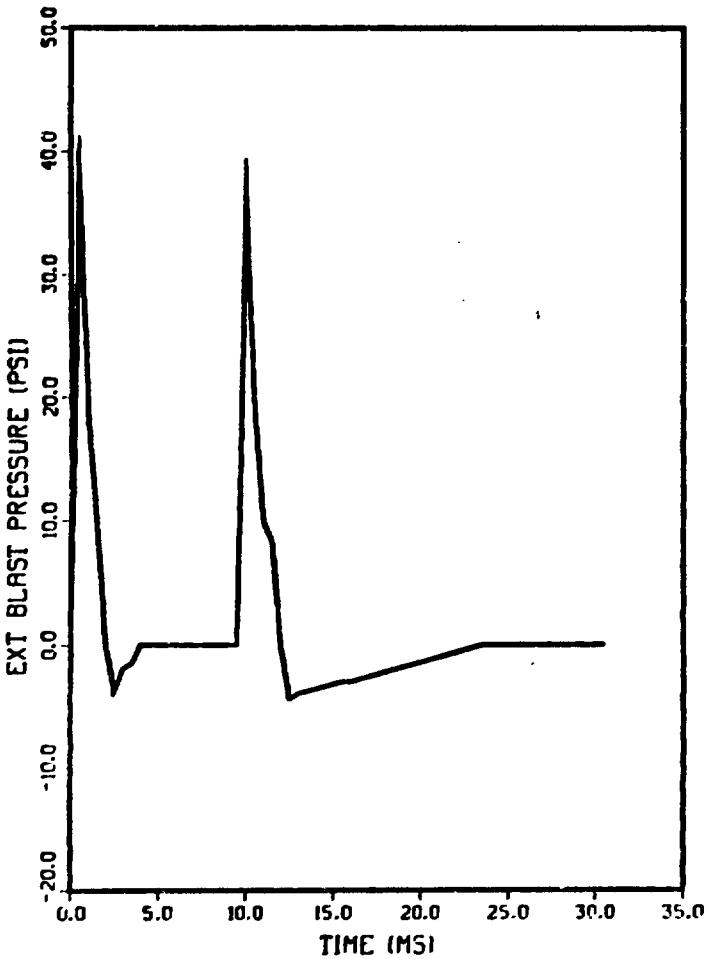

(a) Experimental measured free field blast pressure

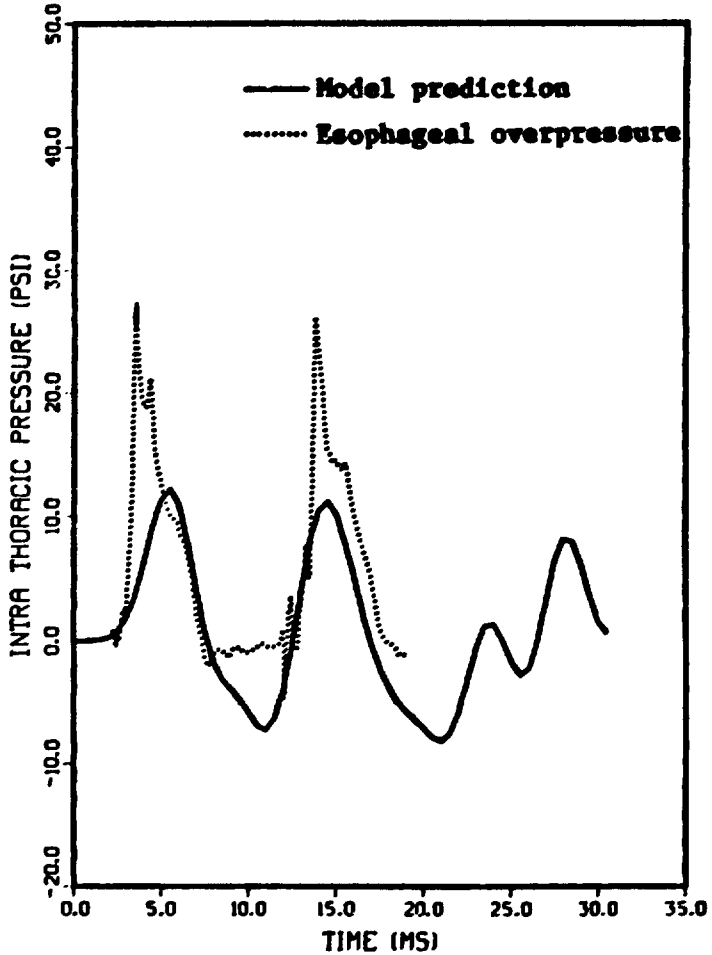

(b) Prediction of lung overpressure history and sheep's esophageal pressure history taken at the seventh intercostal

Figure 5-17. (Case 23) Double peak study, Δt = 9.7 ms. Experimental free field blast pressure, esophageal pressure and overpressure predicted by the two-dimensional FEM model.

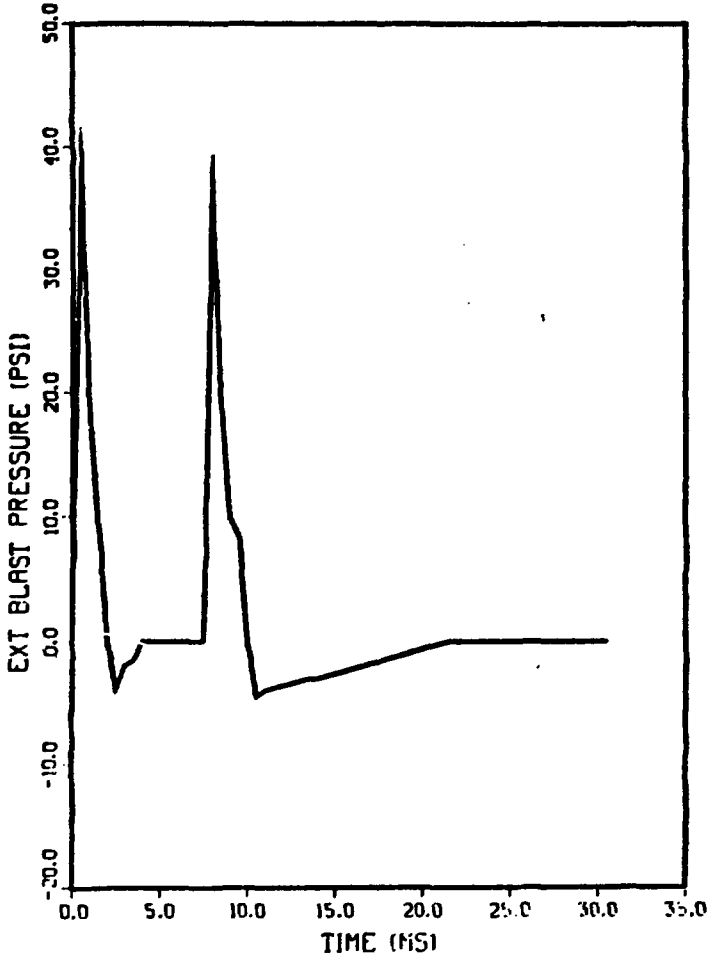

(a) Experimental measured free field blast pressure

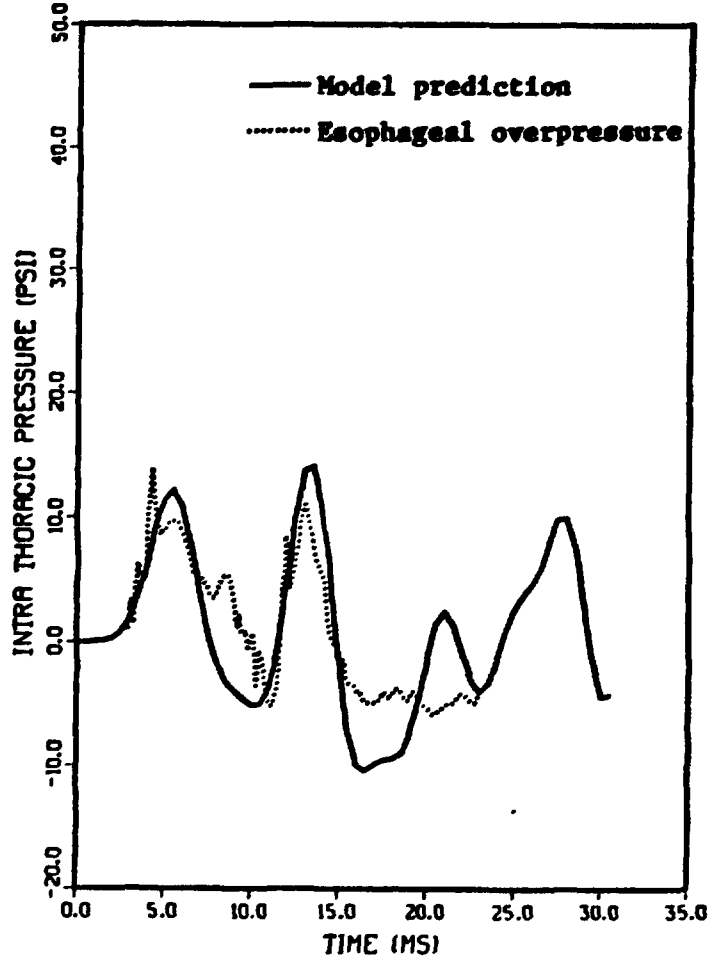

(b) Prediction of lung overpressure history and sheep's esophageal pressure history taken at the seventh intercostal

Figure 5-18. (Case 22) Double peak study, Δt = 7.6 ms. Experimental free field blast pressure, esophageal pressure and overpressure predicted by the two-dimensional FEM model.

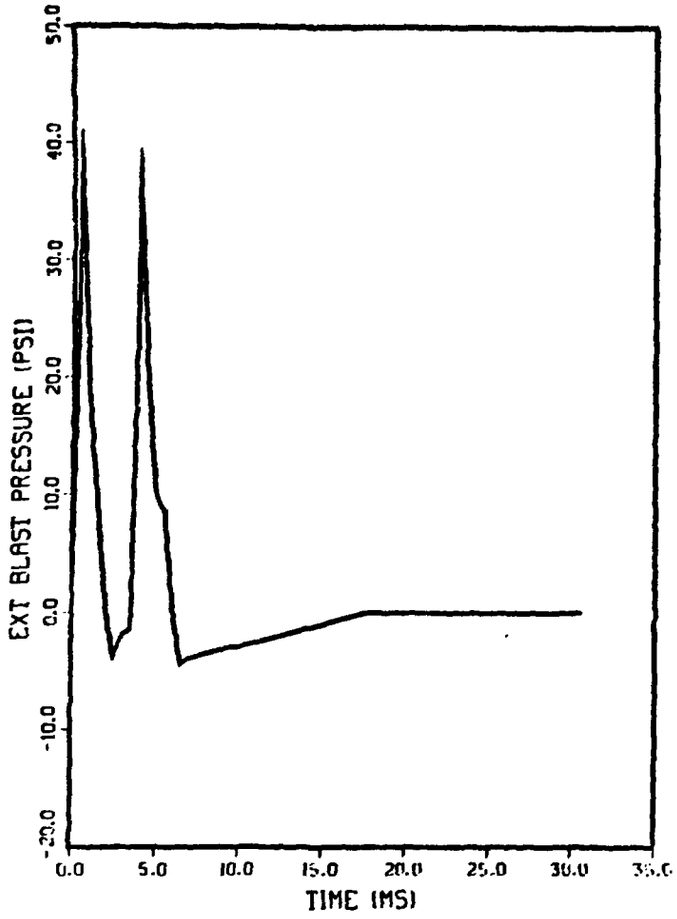

(a) Experimental measured free field blast pressure

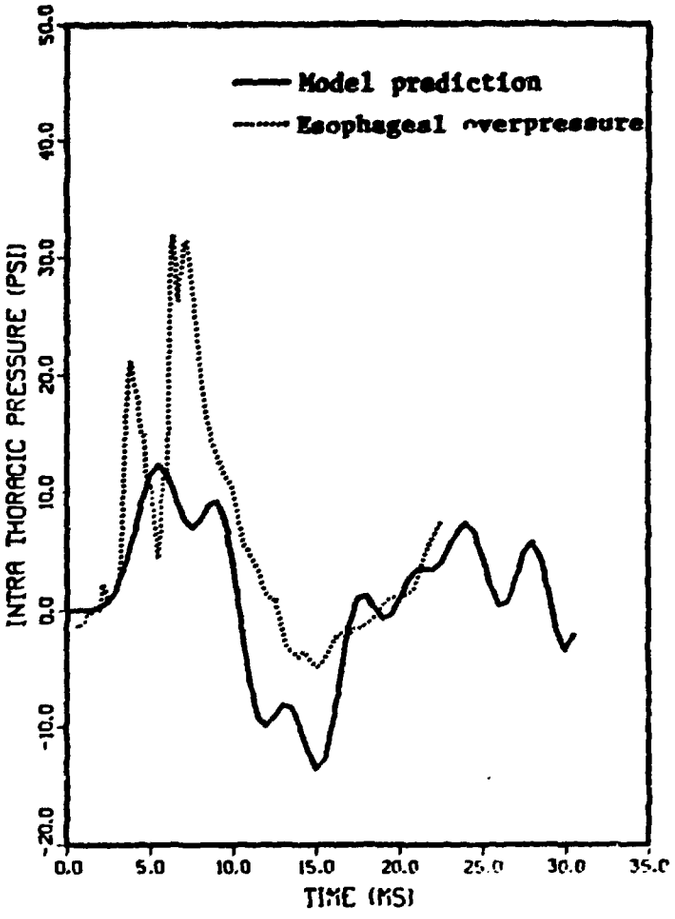

(b) Prediction of lung overpressure history and sheep's esophageal pressure history taken at the seventh intercostal

Figure 5-19. (Case 21) Double peak study, Δt = 3.6 ms. Experimental free field blast pressure, esophageal pressure and overpressure predicted by the two-dimensional FEM model.

In order to understand the effect of, (1) increased loading factor spatial distribution, and (2) temporal variation in the time of wave arrival on the animal response, the model is divided into five different zones, as illustrated in Figure 5-20(a). Directly facing the direction of wave arrival zone A is the first part of the body surface under blast wave incidence and is the part under the most extensive increased loading. Follow the order of B, C, and D different zone starts exposing to the incident wave at a sequentially delayed time and reducing loading factor of 1.8, 1.6 and 1.4, respectively. Body surface at zone E is the last to experience the wave and has no appreciable increased loading. Zone E is assumed to lag zone A by 2 ms. Histories of increased loading at different zones are depicted in Figure 5-20(b). Figure 5-20(c) shows the lung overpressure at seven stations under the prescribed loading distribution and timing sequences. Compared with Figure 5-20(d), in which the model is under the same spatial loading distribution but applied simultaneously, it is seen that only station 2 and station 4, which is located in the back side of the lung, start to respond to the incident wave at a delayed time. No significant difference is observed in the responses at the rest of the transducers.

5.4.2 Isoimpulse Studies

To further examine the responsive behavior of the two-dimensional model isoimpulse blast loading is applied to the model in the following three ways:

1. Isoimpulse with different dP/dt (triangular waves of the same duration, sample peak)

2. Isoimpulse with different peak blast pressure (isosceles triangular waves)

3. Isoimpulse with different loading frequencies (half sine waves)

Isoimpulse with Different dP/dt (triangular waves of the same duration, sample peak) - A constant impulse is applied on the body surface at different dP/dt (triangular wave at fixed peak blast pressure and loading duration). The ITP responses at station 7 are recorded for comparison. Figures 5-21 and 5-22 are results for impulse = 14 and 23 psi-ms, respectively. It appears that the steeper the dP/dt, the faster the ITP prediction rises up and resulting in an

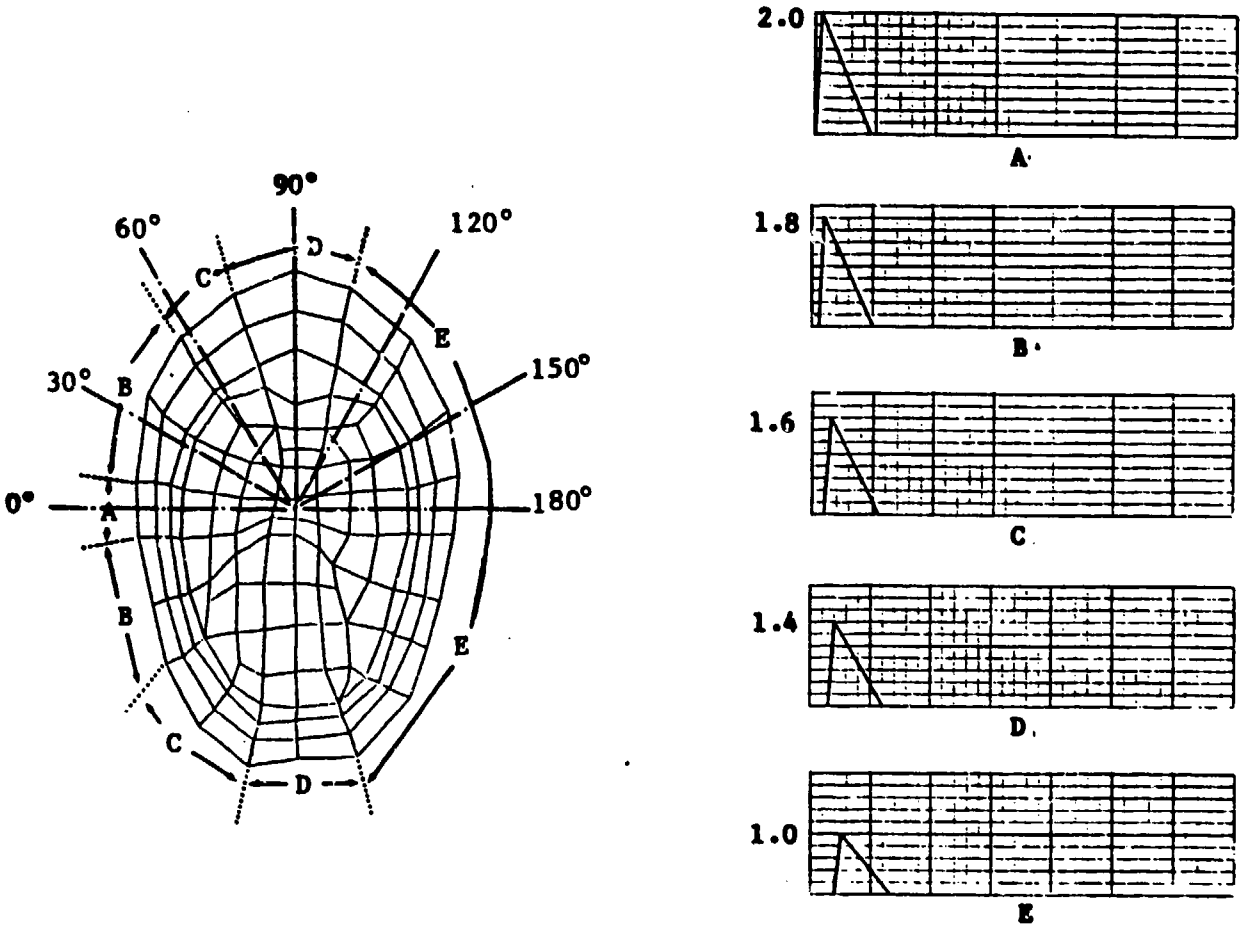

(a) Division of five different zones (labeled as A, B, C, D,E).

(b) Histories of increased loading factors at zone A, B, C, D, E, respectively. (Note: Follow the order of A,B,C,D,E. There is a reducing loading factor as well as a delayed starting time.)

Figure 5–20. Effects of varying firing sequences and loading factor histories on the lung overpressure responses.

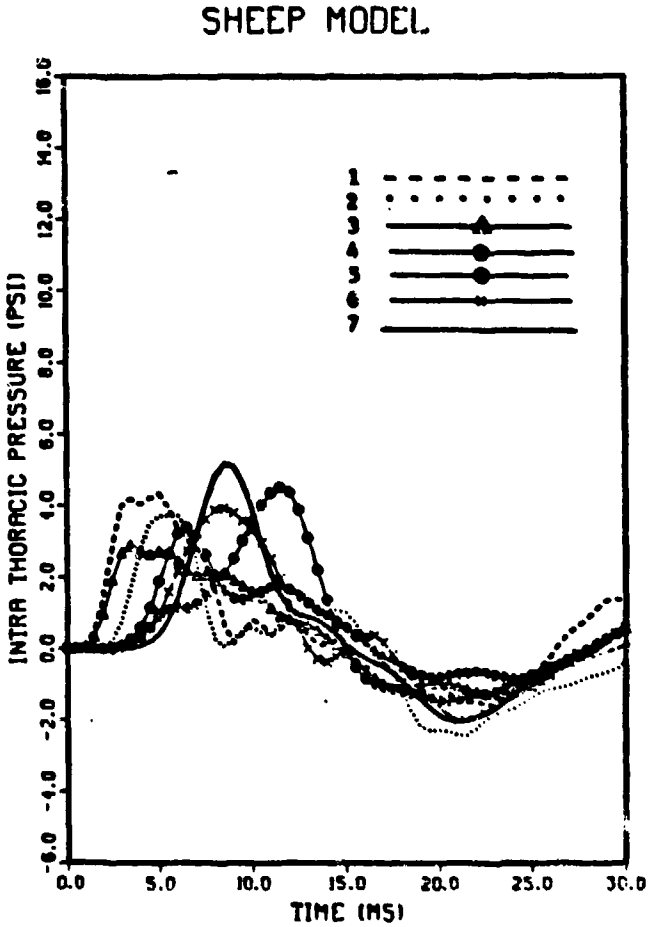

(c) Resulting lung overpressure histories with varying firing sequence.

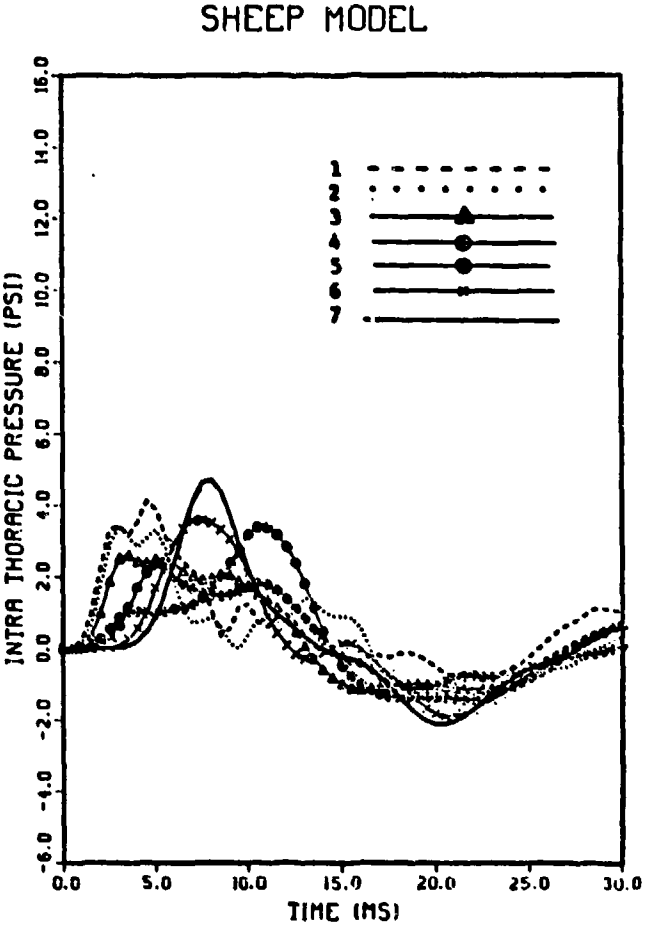

(d) Response curves with simultaneous loading

Figure 5-20. (Cont'd).

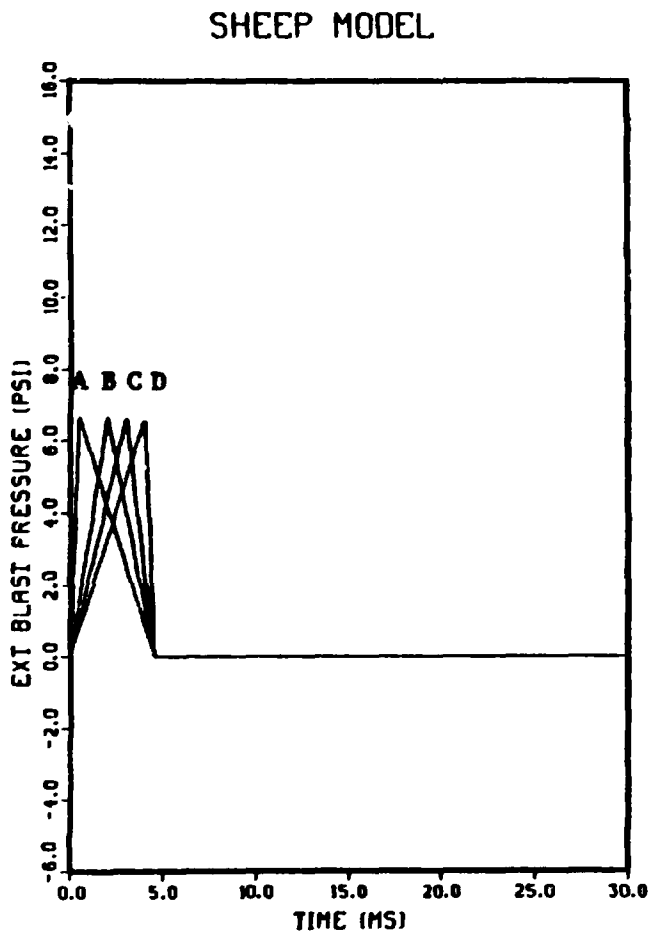

(a) Cases A, B, C, D with different dP/dt

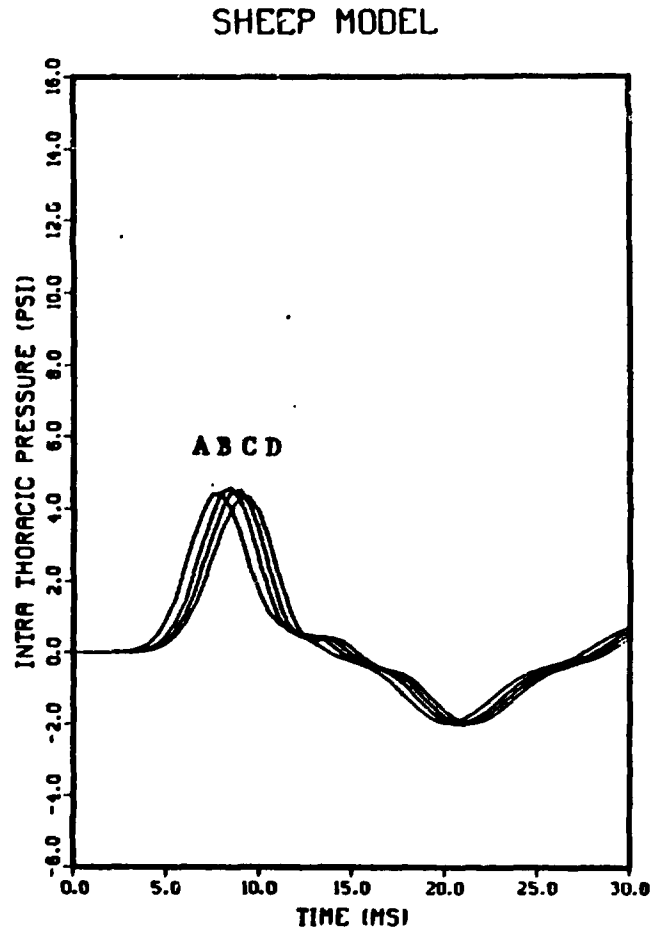

(b) The corresponding lung overpressure responses at the center (station 7 of Figure 5-3)

Figure 5-21. Isoimpulse (14 psi-ms) study with different dP/dt

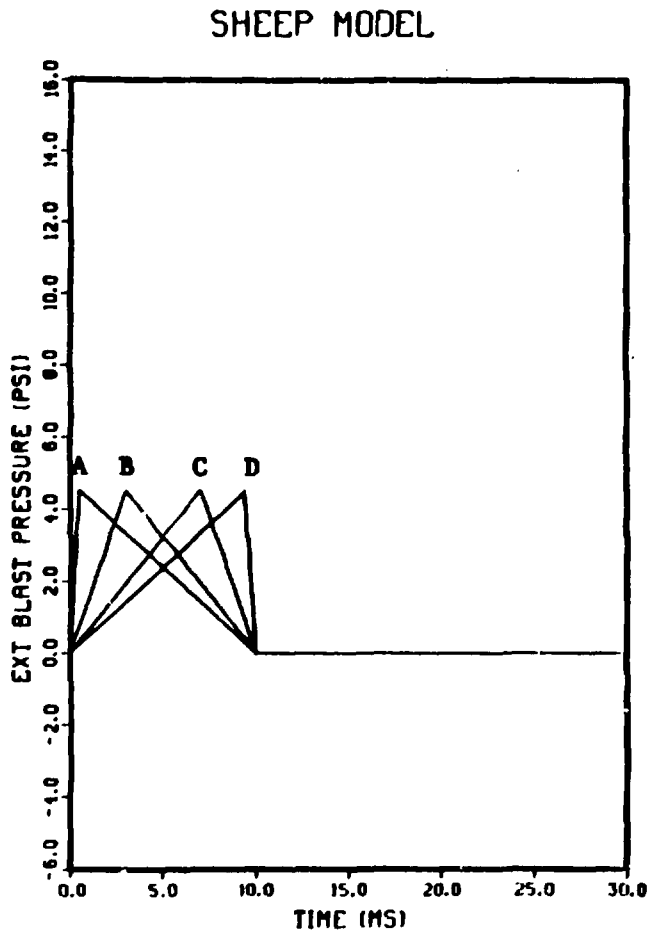

(a) Cases A, B, C, D with different dP/dt

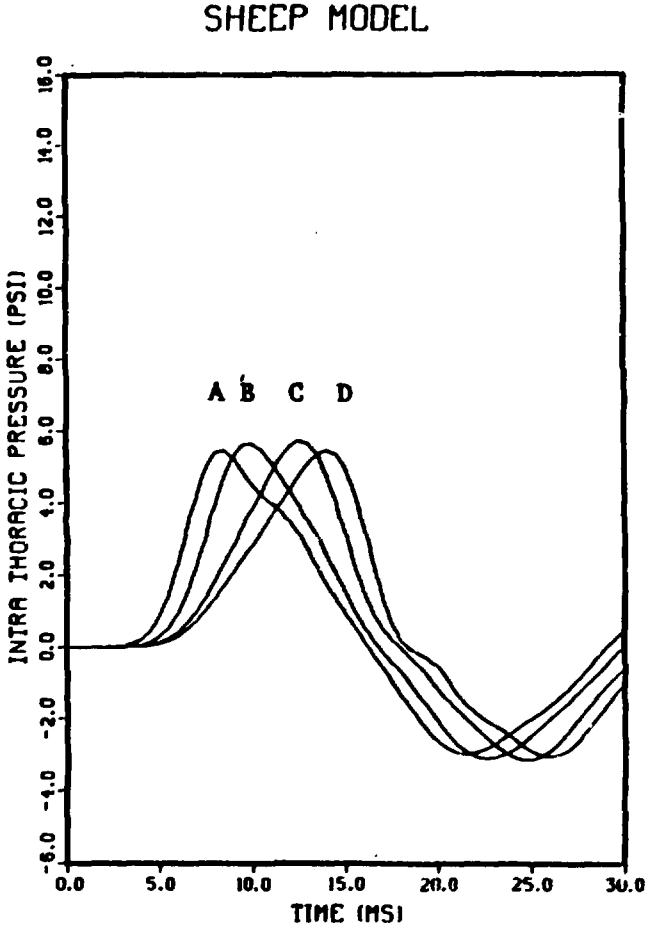

(b) The corresponding lung overpressure responses at the center (station 7 of Figure 5-3)

Figure 5-22. Isoimpulse (23 psi-ms) study with different dP/dt.

earlier peak overpressure time. The magnitudes of the peak ITPs, however, are approximately the same in these comparisons.

Isoimpulse with Different Peak Blast Pressure (isosceles triangular waves) - For short duration air blast waves, the impulse has been considered as an important parameter in causing body injury or even death. For a given impulse, however, the resulting injury also depends on the peak pressure. A fixed amount of impulse (22.1 psi-ms) was used in the WRAIR sheep exposure experiments. This isoimpulse is applied on the animal with different combinations of peak blast pressure and time course. The measured maximum ITP (the esophageal pressure) and the corresponding calculated maximum d(ITP)/dT (the ITP increasing rate) are plotted against the peak blast pressure on Figure 5-23(a) and (b), respectively. The resulting gross lung injury was divided into three different groups separated by two marks indicating borders of "no lung injury" and "severe lung injury".

In order to understand the effect of peak blast pressure and the resulting ITP responses at constant impulse, an impulse of 22.1 psi-ms is applied on the model at different peak blast pressure (isosceles triangular waves). Ten different loadings whose peak blast pressure varying from 2.46 up to 44.2 psi were applied on the model and the transient interaction are followed. To compare with the WRAIR experimental results under the same type of loading, the maximum ITP and the maximum d(ITP)/dT from model prediction are plotted as dotted lines on Figure 5-23(a) and (b) of WRAIR previous results for comparison. The model prediction at the center of the lung (the subplots at the upper right) is taken for this comparison. Since it is at a comparable location where the esophageal pressure was measured.

Detailed ITP responses of six representative cases are shown in Figure 5-24(a) through (f). For each case the upper left subplot shows the external blast pressure history. The rest of the nine subplots show the ITP responses at various locations in the lung as indicated by arrows.

A study of the responses at various loading cases suggests that:

a. At higher blast pressure and shorter duration, the wave feature becomes important. Wave focusing at the geometrical focal point and wave reflection from a neighboring "firm organ" can lead to local high overpressure response.

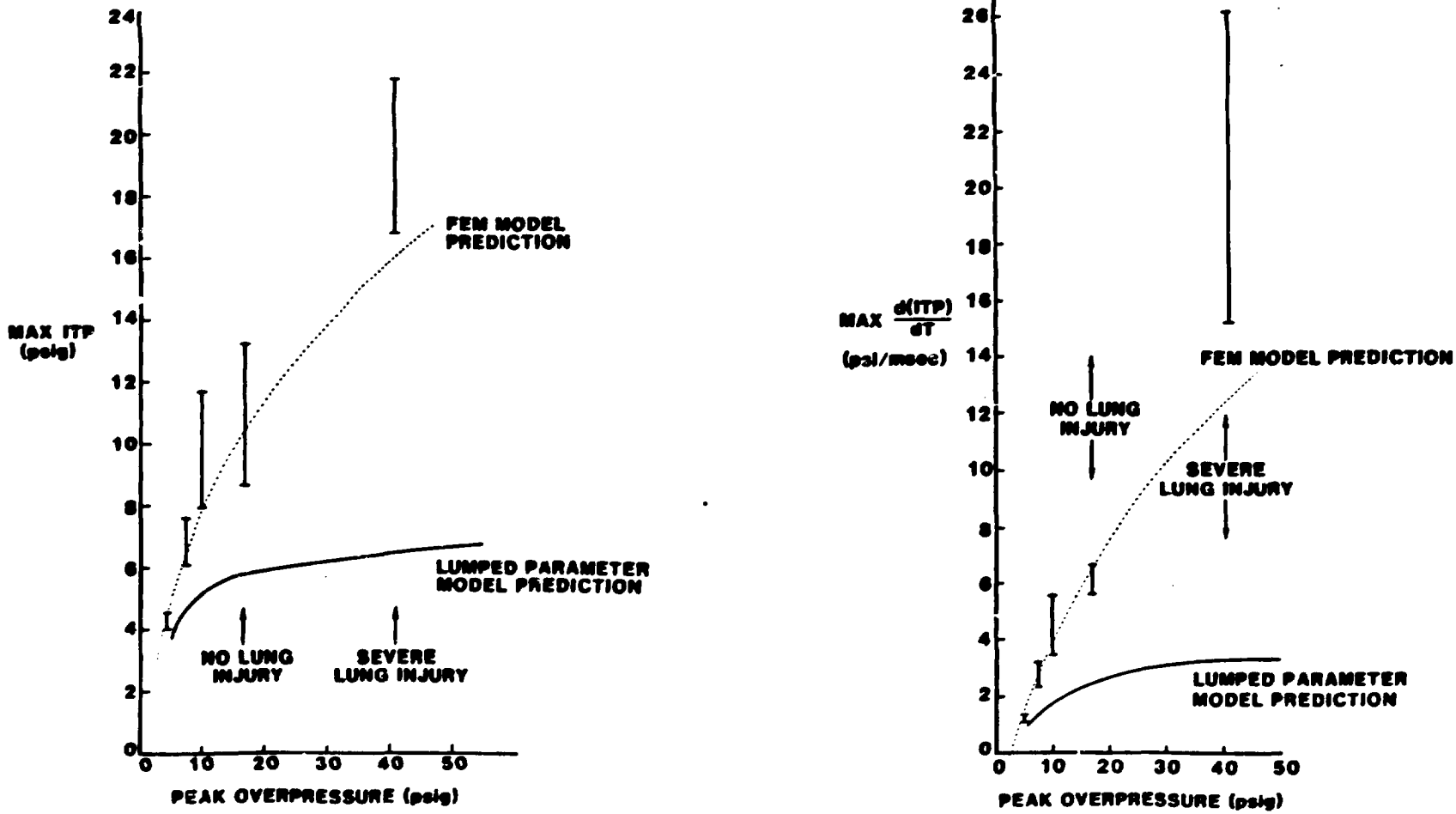

Figure 5-23. Comparison of two-dimensional FEM prediction with previous WRAIR experimental results and lumped-parameter predictions.

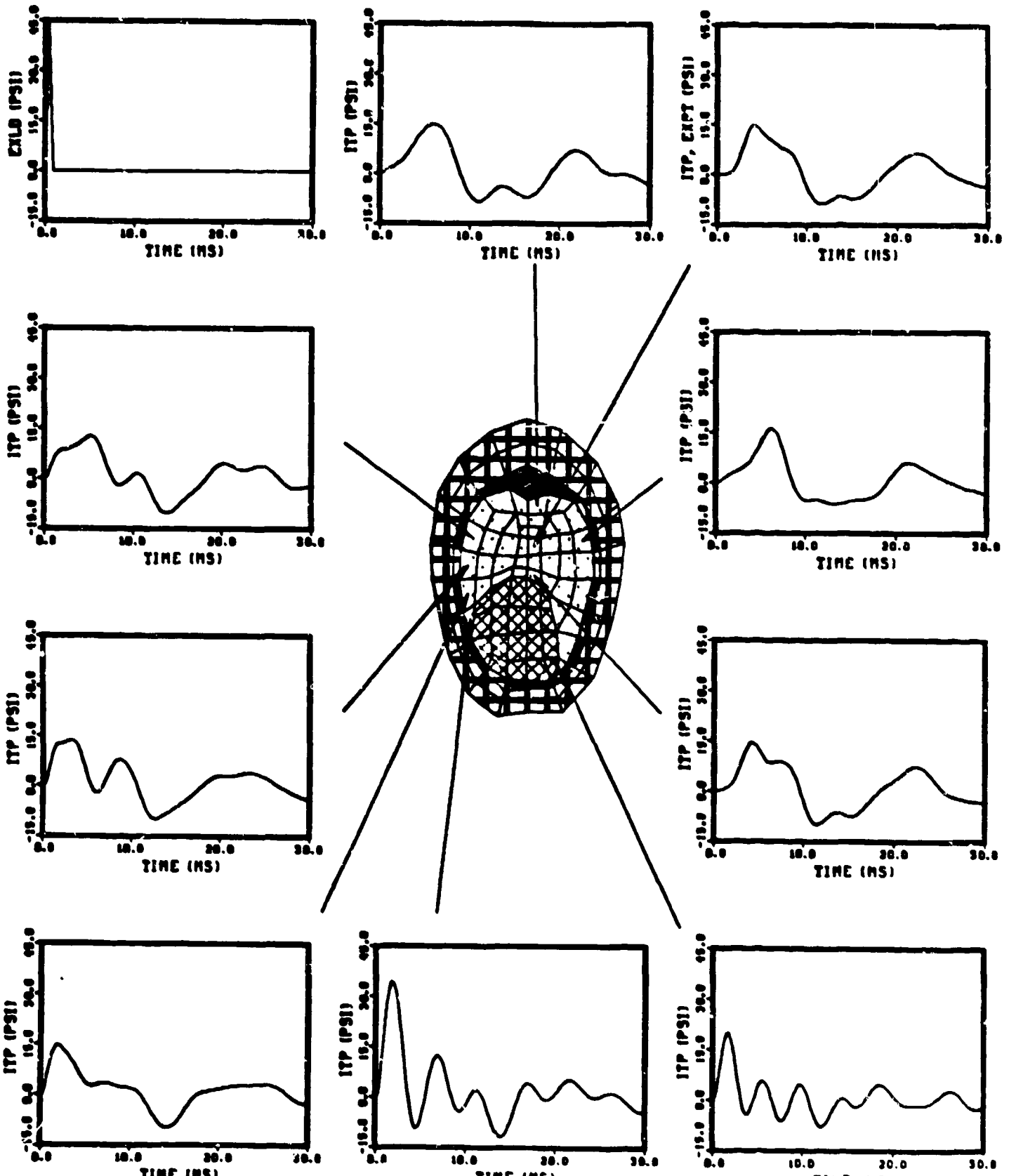

(a) Peak pressure = 44.2 psi

Figure 5-24. Isoimpulse loading (22.1 psi-ms) with different peak blast overpressures (isosceles triangular waves).

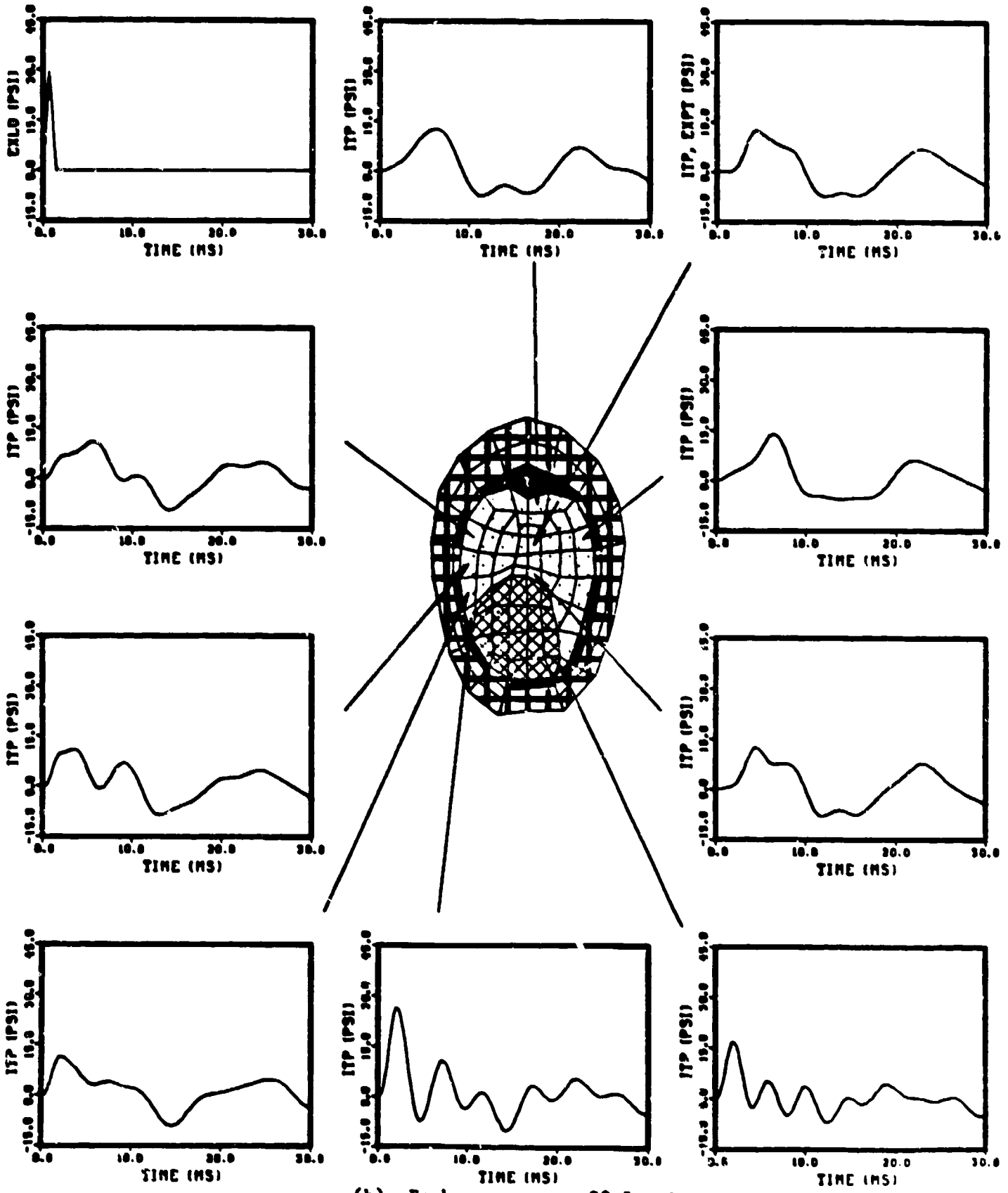

(b) Peak pressure = 29.5 psi

Figure 5-24. (Cont'd).

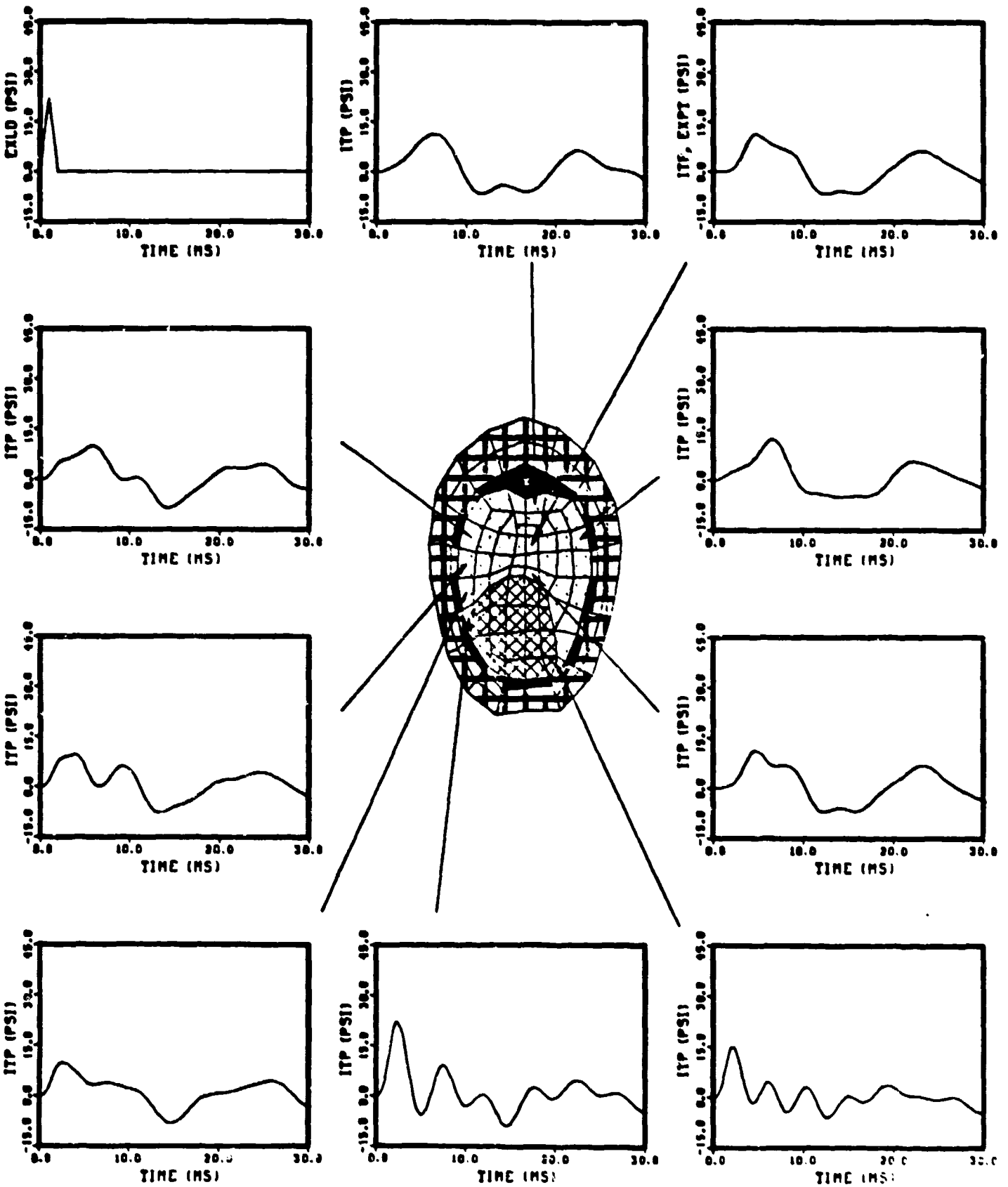

(c) Peak pressure = 22.1 psi

Figure 5-24. (Cont'd).

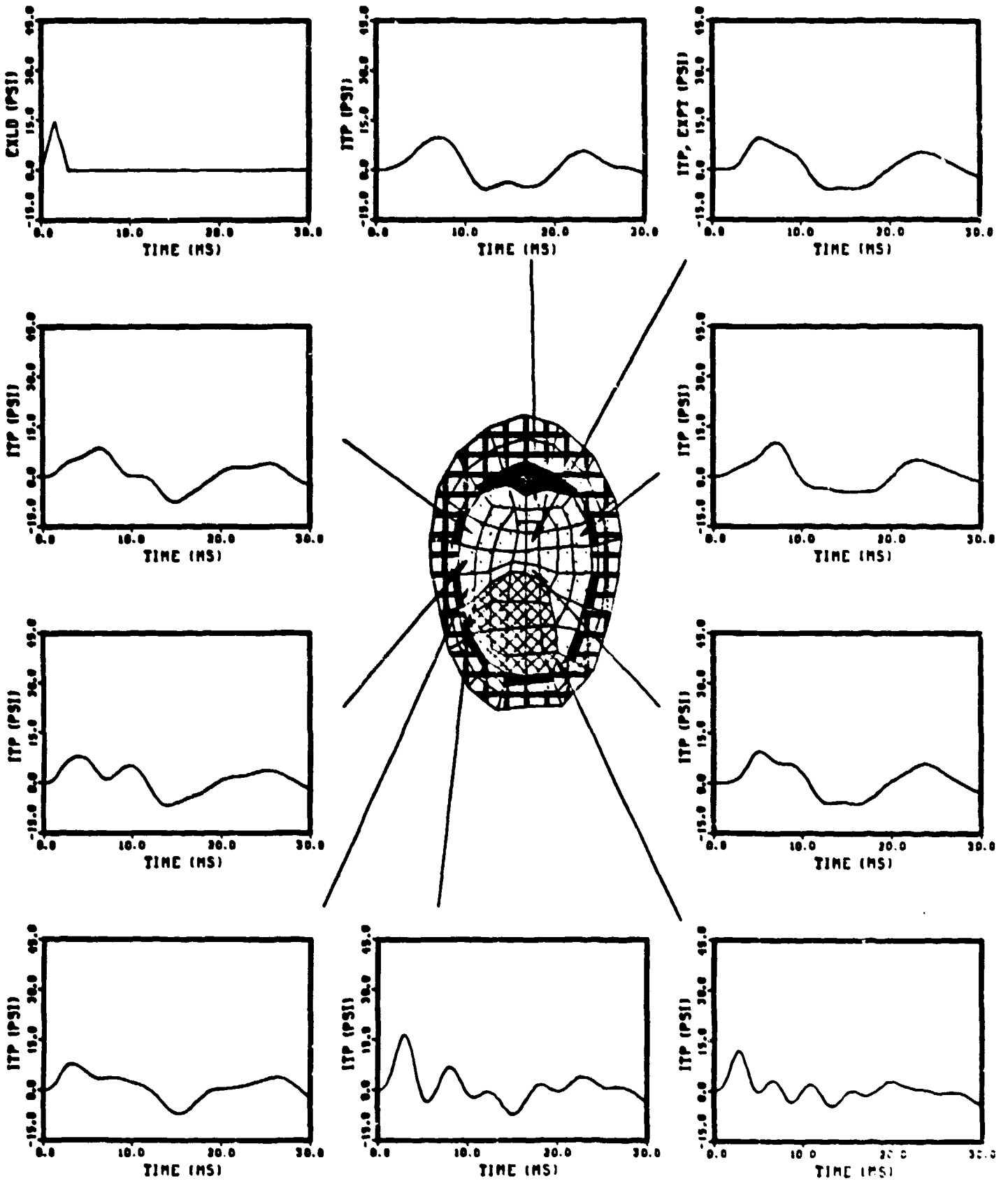

(d) Peak pressure = 14.7 psi

Figure 5-24. (Cont'd).

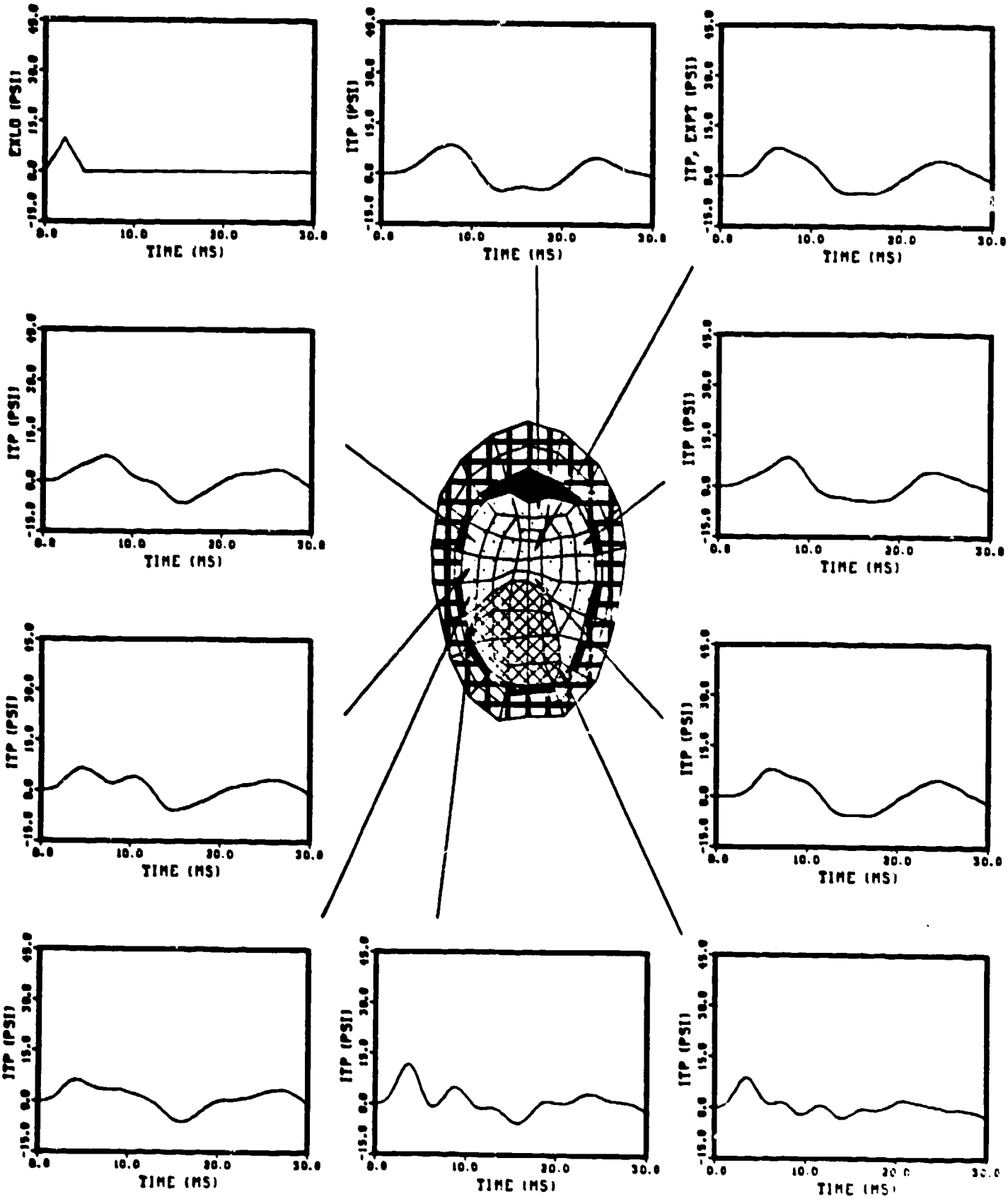

(e) Peak pressure = 9.82 psi

Figure 5-24. (Cont'd).

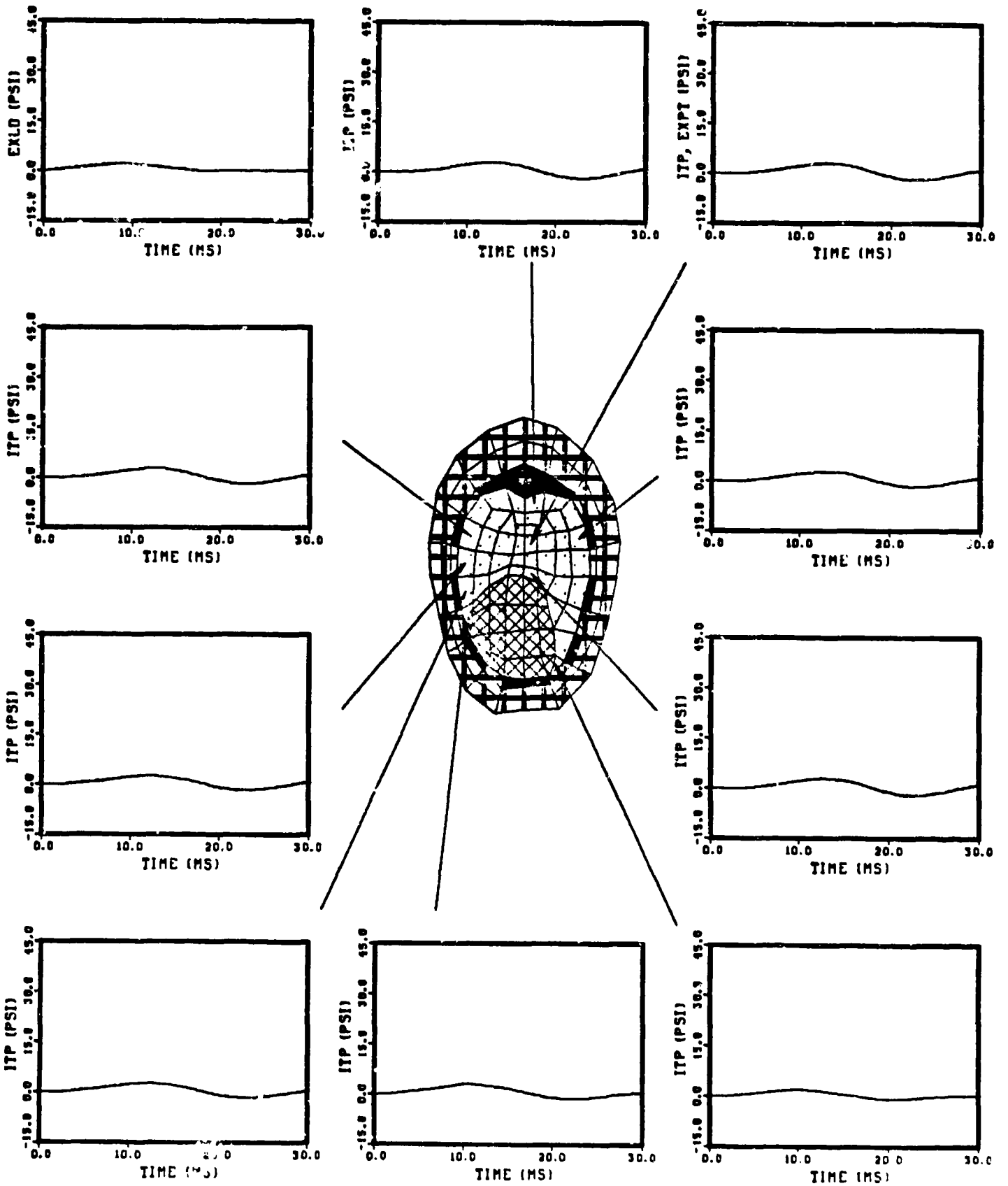

(f) Peak pressure = 2.46 psi

Figure 5-24. (Cont'd).

b. Probe 1 is located in the wave impact side at a corner between incompressible material, where wave reflection is likely to occur more frequently in a given time. Repetitive additive effect at such a narrow zone can result in very pronounced local loading. Probe 2 is also located at a corner between incompressible material but at the back side. Similar wave reflection results in high local pressure.

c. Probe 7 is located approximately at a geometric focal point. The results show the wave focusing at this point.

d. At low peak blast pressure and long duration a uniform response is expected in the whole lung [see Fig. 5-24(f)].

Isoimpulse with Different Loading Frequencies (half sine waves) - Isoimpulse blast loadings of half sine wave with varying frequencies and peak blast pressure are also applied on the model to see the variation in ITP predictions. Three cases with frequencies equal to 111, 56, and 28 Hz (the corresponding angular frequencies ω are 700, 350, and 175 radian/sec, respectively) were carried out, see Figure 5-25. In the first case with 111 Hz, the transient response in different parts of the lung is clearly seen. However, for the case of 28 Hz, even with the same amount of impulse loading, the whole lung responds in a nearly uniform way. This demonstrates that when under high frequency blast wave loading different parts of the lung experience different loading history on account of the wave propagation effects. For the low frequency loading, the external forcing function has enough time to become dominant to drive the whole lung to respond in a uniform way. If the local ITP history is an indication of the mechanical stress the local lung tissue experiences, the former case is likely to create more injury in terms of area (or volume) and degree of severity. And damages in the latter case are more due to gross body deformation. Jönsson et al. [8] indicate that severe hemorrhages in the lungs were produced at impact velocity exceeding 10 m/s. For velocities below 5 m/s accompanying large body deformation lethal injuries were produced without severe hemorrhages. For a given impulse short duration high peak blast is likely to create higher chest wall velocity and result in damages of the former category. An injury map in terms of area, penetration depth from pleural surface, and degree of severity with respect to geometric descriptions [curvature of the local pleural surface, bordering organs (ribs, heart, etc.)] and anatomical descriptions (hilar support, large vessel, airway, etc.) will assist in the assessment of damage mechanism.

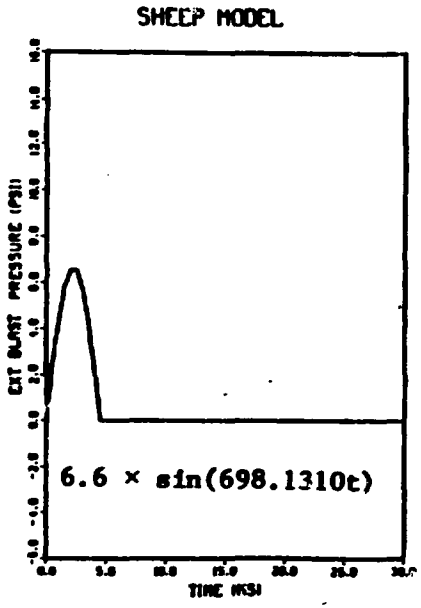

(a) Ext loading: 6.6 × sin(698.1310t)

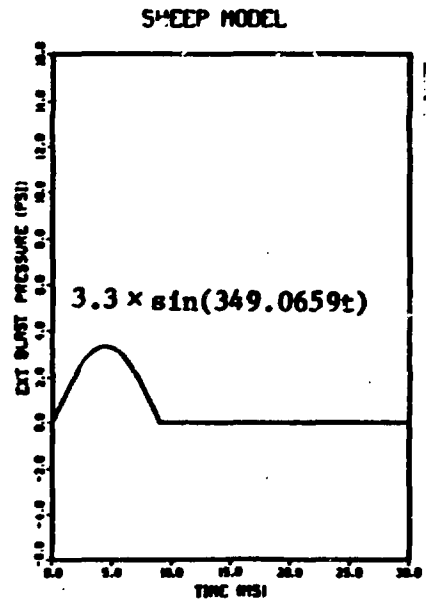

(c) Ext loading: 3.3 × sin(349.0659t)

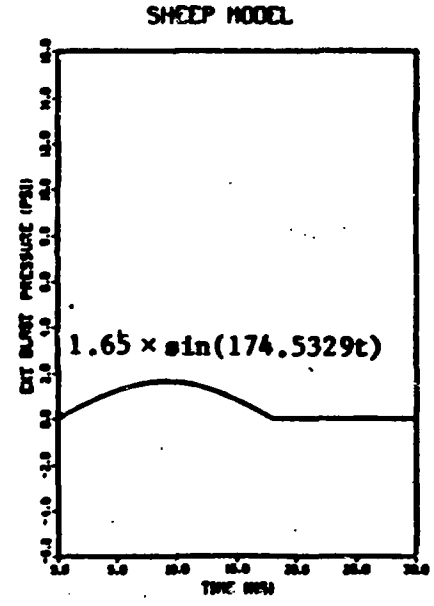

(e) Ext loading: 1.65 × sin(174.5329t)

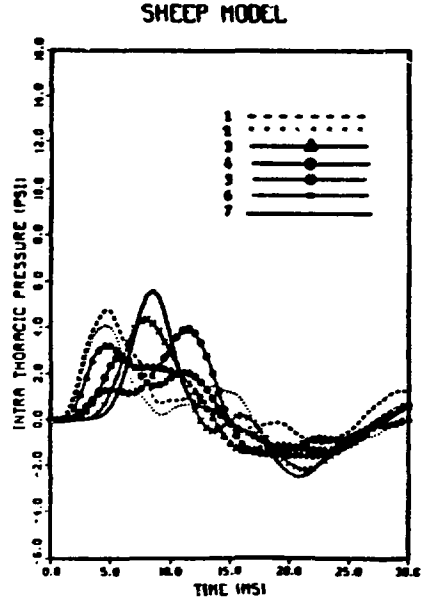

(b) The resulting lung overpressure at various stations

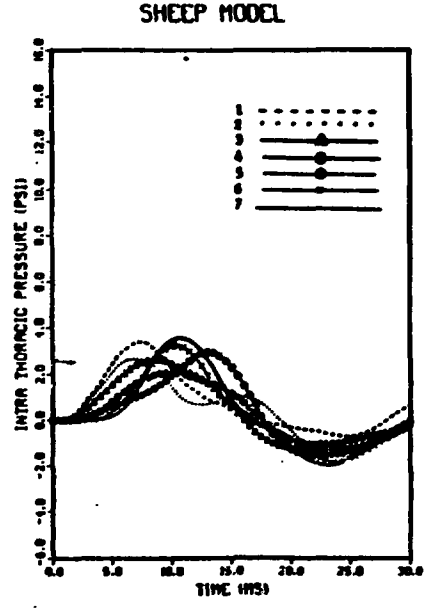

(d) The resulting lung overpressure at various stations

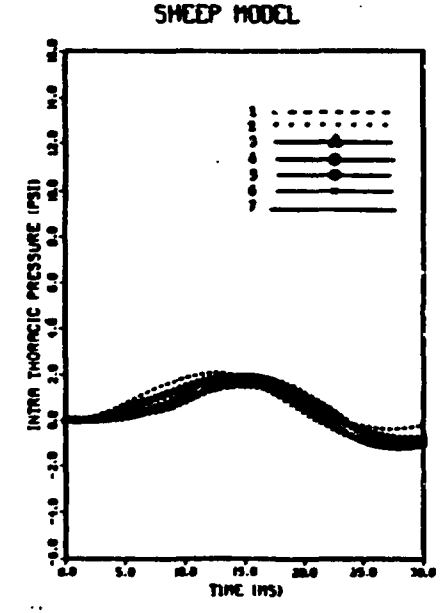

(f) The resulting lung overpressure at various stations

Figure 5-25. Isoimpulse study with varying loading frequencies and amplitudes. Case 1: (a) & (b), Case 2: (c) & (d), Case 3: (e) & (f).

5.4.3 Effect of Fat

In order to understand the effect of fat on the ITP responses when a sheep is under blast exposure, an additional layer representing fat is added to the body surface of the sheep model. The material is represented by an incompressible gel type material with density and bulk modulus the same as water. The thickness of the fat layer is increased up to 6 cm and the corresponding ITP histories at the center of the lung region are shown on Figure 5-26.

Due to the increased total weight, the added fat layer appears to reduce the peak ITP as well as to slow the ITP response. However, the degree of change (8% decrease in peak ITP for 6 cm increase in fat layer) does not seem to be very significant within the range of increase.

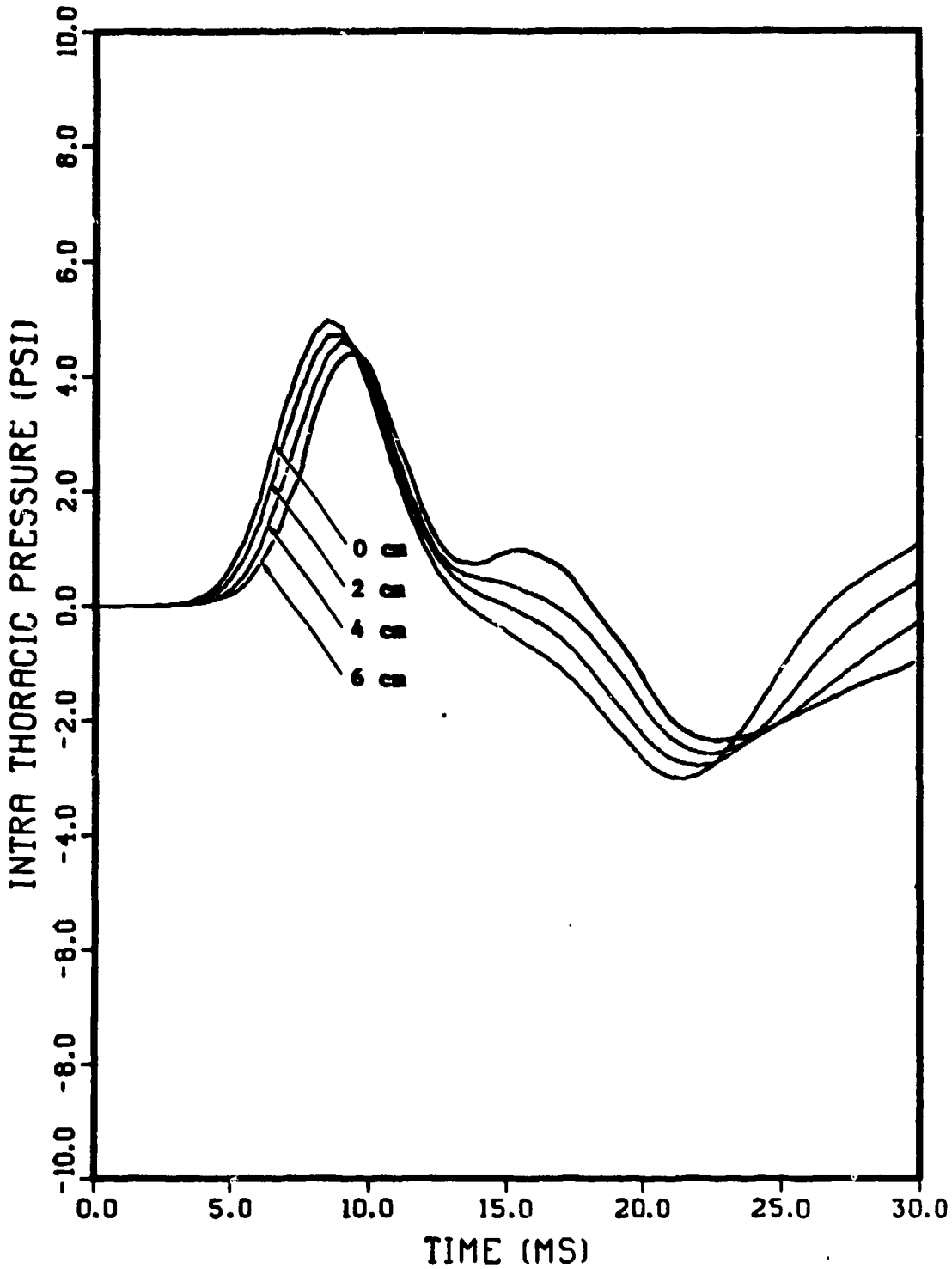

Figure 5-26. The model ITP responses (at the center of lung region) at varying fat thicknesses.

6. SUMMARY

A simplified 16-element three-dimensional model is constructed in Section 4. This model is shown to reproduce the major body response of a sheep under blast wave loading. To study the wave propagation characteristics inside the thorax in greater detail, a two-dimensional model is presented in Section 5. This model shows that different regions of the lung can experience different overpressure histories during exposure. It suggests that the interpretation of measured esophageal pressure should be carefully justified as progressive wave propagation could result in different response histories at different parts of the lung and thereby different damage mechanisms.

The model is validated with experimental results from various loading cases, e.g., 4 single-peak, 3 double-peak, and 10 cases from isoimpulse studies. Reasonably good agreement is obtained among comparisons made between the model ITP predictions and the experimental esophageal pressure measurement.

Material parametric study is carried out to identify the material parameters which are important in the body's ITP response to external blast wave. These include the density, the shear and bulk moduli of the effective muscle/rib, and the bulk modulus and the density of the lung.

More refinement and improvement on the current model is expected in the next phase. Refined spatial resolution will certainly reduce the numerical error in the solutions. At high blast loading pressure (P_{peak} > 25 psi) the ITP response does not have as high peak pressure as the experimental measurement. This is to be improved by using the ideal gas-type nonlinear stress-strain law of the lung. The insufficient rarefaction of the ITP responses, especially that at the tension side, can be improved by proper treatment of damping mechanisms. These improvements are tasked in the next phase.

REFERENCES

1. Amtmann, E. and H. P. Schmitt, Z. Anat., 127: 25-41 (1968).

2. Clemedson, C.-J., et al., "Dynamic Response of Thorax and Abdomen of Rabbits in Partial and Wholebody Blast Exposure," Am. J. Physiol. 216, 615-620 (1969).

3. Clemedson, C.-J. et al., "Effects on Extra- and Intrathoracic Pressure Pattern and Lung Injuries of Rigid and Soft Protection of Thorax in Air Blast Exposed Rabbits," Försvarsmedicin 7, 172-190 (1971).

4. Clemedson, C.-J. and A. Jönsson, "Effects of the Frequency Content in Complex Air Shock Waves on Lung Injuries in Rabbits," Aviat. Space Envir. Med. 47, 1143-1152 (1976).

5. Crossfill, M. L. and J. G. Widdicombe, "Physical Characteristics of the Chest and Lungs and the Work of Breathing in Different Mammalian Species," J. Physiol., 158: 1-14 (1961).

6. Fung, Y. C. and M. R. Yen, "Characterization and Modeling of Thoraco-Abdominal Response to Blast Waves - Volume 3: Lung Dynamics and Mechanical Properties Determination," Final Report to WRAIR under Contract No. DAMD17-82-C-2062 (1985).

7. Getty, R., Sisson and Grossman's The Anatomy of the Domestic Animals, 5th Ed., W. B. Saunder Co., 1975.

8. Jönsson, A. et al., "Dynamic factors influencing the production of lung injury in rabbits subjected to blunt chest wall impact," Aviat. Space Environm. Med. 50, 325-337 (1979).

9. Popesko, P., Atlas of Topographical Anatomy of the Domestic Animals, 2nd Ed., W. B. Saunder Co., 1979.

10. Richmond, D. R., et al., "The Relationship Between Selected Blast-Wave Parameters and the Response of Mammals Exposed to Air Blast," Annals N. Y. Acad. Sci., 152-1: 103-121 (1968).

11. Taylor, R. L. and J. L. Sackman, "Contact-Impact Problem," Report No. SESM 78-4, University of California at Berkeley, 1978.

12. Yamada, H., Strength of Biological Materials, The Williams and Wilkins Co., Baltimore, 1970.

13. Zienkiewicz, O. C., The Finite Element Method, 3rd Ed., McGraw-Hill, 1977.

14. Zuckerman, S., "The Problem of Blast Injuries," Proc. Roy. Soc. Med. 34: 171-188 (1941).

15. Bowen, I. G., et al., "Fluid-Mechanical Model of the Thoraco-Abdominal System with Applications to Blast Biology," NASA Report 1675 (1965).

16. White, C. S., et al., "The Biodynamics of Airblast," DNA Report 2738T (1971).

17. Fletcher, E. R., J. T. Yelverton, and D. R. Richmond, "The Thoraco-Abdominal System's Response to Underwater Blast," Lovelace Foundation, Albuquerque, New Mexico, Report LF-55 (1976).

18. Jönsson, A., "Experimental Investigations on the Machanisms of Lung Injury in Blast and Impact Exposure," Linköping University Medical Dissertations No. 80, Stockholm, Sweden (1979).

19. Clemedson, C.-J., "Blast Injury," Physiol. Rev., 36, 336-354 (1956).

20. Yu, J. H.-Y., et al., "Characterizaton and Modeling of Thoraco-Abdominal Response to Blast Waves - Volume 2: Blast Load Definition on a Torso Model," Final Report to WRAIR under Contract No. DAMD17-82-C-2062 (1985).

APPENDIX A

UTL. READ80/ASCII

```
UTL(1).READ80/ASCII.CBL(1)
            IDENTIFICATION DIVISION.
            PROGRAM-ID. READIT.
            ENVIRONMENT DIVISION.
            CONFIGURATION SECTION.
            SOURCE-COMPUTER. UNIVAC-1100.
            OBJECT-COMPUTER. UNIVAC-1100.
            INPUT-OUTPUT SECTION.
            FILE-CONTROL.
                SELECT  INFILE   ASSIGN TO INTERCHANGE Y.
                SELECT  OUT  ASSIGN TO PRINTER Z.
            DATA DIVISION.
            FILE SECTION.
            FD  INFILE   LABEL RECORD IS OMITTED  RECORDING MODE F
                         BLOCK CONTAINS    20    RECORDS.
            01  INREC   PIC X(80).
            FD  OUT  LABEL RECORD IS OMITTED.
            01  OUTREC  PIC X(80).
            WORKING-STORAGE SECTION.
            01  COUNTIT   PIC 99999  VALUE 0.
            PROCEDURE DIVISION.
            STARTIT.
                OPEN INPUT  INFILE WITH NO REWIND.
                OPEN OUTPUT OUT.
            LOOP.
                READ INFILE     AT END GO TO THEND.
                     ADD 1 TO COUNTIT.
                MOVE INREC   TO  OUTREC.
                WRITE OUTREC.
                GO TO LOOP.
            THEND.
                CLOSE INFILE   WITH NO REWIND.
                CLOSE OUT.
                     DISPLAY ' COUNT ' COUNTIT  UPON PRINTER.
                STOP  RUN.
```

LINK.MOVFEA

```
LINK(,).MOVFEA1(14)
      C     PROGRAM MOVFEA
      C     THIS PROGRAM READS OUTPUT (TAPE 18) GENERATED BY NEWUTILITY OF
      C     MOVIE.BYU .  DATA ON TAPE 18 IS IN MOVIE FORMAT.  PROGRAM MOVFEA
      C     WILL REARRANGE THE DATA IN FEAP FORMAT AND WRITE IT TO TAPE 19.
      C     ICOD ARRAY IN NODAL BLOCK IS TO BE SUPPLIED HERE.
      C     MAT  ARRAY IN ELEMENT BLOCK IS TO BE SUPPLIED HERE.
      C     THIS PROGRAM PREPARES THE FOLLOWING 3 BLOCKS :
      C                     FEAP
      C                     NODAL
      C                     ELEMENT
      C
            PARAMETER NUMMAP=5    ,   NUMNPP=85    ,   NUMELP=16
            DIMENSION NPL(2,NUMMAP), X(3,NUMNPP), IP(8,NUMELP),
           *          ICOD(NUMNPP),  MAT(NUMELP)
      C
      C     ---------- READ INPUT FROM NEWUTILITY ----------
      C
            READ(18,150)NUMMAT,NUMNP,NUMELT
            NUMMAT=IABS(NUMMAT)
            READ(18,150)((NPL(I,J),I=1,2),J=1,NUMMAT)
            READ(18,180)((X(I,J),I=1,3),J=1,NUMNP)
            READ(18,150)((IP(I,J),I=1,8),J=1,NUMELT)
      150   FORMAT(16I5)
      180   FORMAT(6E12.5)
      C
      C     ---------- WRITE INITIALIZATION CARDS ----------
            NEN=8
            NEXTRA=0
            IPEC=1
            MEAN=120
            WRITE(19,*)'      FEAPMR  ---  TEST RUN OF LINK.MOVFEA  ---  '
            WRITE(19,*)'    3    X    Y    Z'
            WRITE(19,*)'    3    U    V    W'
            WRITE(19,1010)NUMNP,NUMELT,NUMMAT,NEN,NEXTRA,IPEC,MEAN
      1010  FORMAT(7I5)
      C
      C     ---------- WRITE NODAL CARDS ----------
            ICOD( 1)=011000
            ICOD( 2)=011000
            ICOD( 3)=001000
            ICOD( 4)=001000
            ICOD( 5)=010000
            ICOD( 6)=010000
            ICOD( 7)=010000
            ICOD(12)=010000
            ICOD(13)=011000
            ICOD(14)=001000
            ICOD(15)=010000
            ICOD(17)=010000
            ICOD(18)=001000
            ICOD(20)=001000
            ICOD(25)=001000
```

```
      ICOD(28)=001000
      ICOD(29)=001000
      ICOD(34)=001000
      ICOD(37)=011000
      ICOD(38)=011000
      ICOD(39)=010000
      ICOD(40)=010000
      ICOD(41)=010000
      ICOD(42)=010000
      ICOD(43)=011000
      ICOD(44)=010000
      ICOD(45)=010000
      WRITE(19,*)'      NODAL'
      DO 100 J=1,NUMNP
  100 WRITE(19,1020)J,ICOD(J),(X(I,J),I=1,2)
      WRITE(19,1021)
 1020 FORMAT(I5,I15,2F10.3)
 1021 FORMAT(1H )
C
C     ---------- WRITE ELEMENT CARDS ----------
      MAT( 1)=1
      MAT( 2)=1
      MAT( 3)=1
      MAT( 4)=1
      MAT( 5)=2
      MAT( 6)=2
      MAT( 7)=2
      MAT( 8)=2
      MAT( 9)=4
      MAT(10)=4
      MAT(11)=5
      MAT(12)=5
      MAT(13)=4
      MAT(14)=6
      MAT(15)=6
      MAT(16)=6
      WRITE(19,*)'      ELEMENT'
      DO 200 J=1,NUMELT
      WRITE(19,1030)J,MAT(J),
  200 WRITE(19,1031)(IP(I,J),I=1,8)
      WRITE(19,1021)
 1030 FORMAT(4I5,2013)
 1031 FORMAT(2014)
C
      STOP
      END
```

LINK.FEAMOV

```
LINK(.).FEAMOV(11)
      C       PROGRAM FEAMOV
      C       THE PROGRAM FEAMOV READS OUTPUT (ON TAPE 20), E.G. DISPLACEMENT,
      C       AND STRESS COMPONENTS AT EACH TIME STEP, FROM FEAP AFTER FEM
      C       TRANSIENT ANALYSIS AND WRITES VECTOR AND/OR SCALAR FUNCTIONS
      C       IN MOVIE FORMAT TO TAPE 21.
      C
            DIMENSION XYZ(7,45),U(7,45),XIG(7,3,16)
            READ(20,1150)NTS,NDIM,NDF,NUMNP,NUMEL
      C     WRITE(21,1150)NTS,NDIM,NDF,NUMNP,NUMEL
      C
            DO 800 NI=1,NTS
            READ(20,1200)NT,TIME
      C     WRITE(21,1250)NT,TIME
               DO 700 N=1,NUMNP
               READ(20,1300)NNODE,(XYZ(I,N),I=1,NDIM),(U(I,N),I=1,NDF)
      700      CONTINUE
      C             WRITE(21,1349)
                    WRITE(21,1350)((U(I,J),I=1,NDF),J=1,NUMNP)
      C
               DO 400 N=1,NUMEL
               READ(20,1400)NELM,((XIG(I,J,N),J=I,NDIM),I=1,NDIM)
      400      CONTINUE
      C             WRITE(21,1449)
      C                   THE HYDROSTATIC PRESSURES ARE CONVERTED FROM
      C                   DYNE/(CM**2) INTO  PSI
                    WRITE(21,1450)((XIG(1,1,N)+XIG(2,2,N)+XIG(7,3,N))/3./
     .                              .7032E05,N=1,NUMEL)
      800   CONTINUE
      C
      C
      1150  FORMAT(5I8)
      1150  FORMAT(4HNTS=,I4,6X,5HNDIM=,I4,6X,4HNDF=,I4,6X,6HNUMNP=,I4,6X,
     .       6HNUMEL=,I4)
      1200  FORMAT(I5,E12.5E2)
      C1250 FORMAT(30X,11HTIME STEP =,I5,10X,6HTIME =,E12.5E2)
      1300  FORMAT(I7,6E12.5E2)
      C1349 FORMAT(6X,5HDISPL)
      1350  FORMAT(6E12.5E2)
      1400  FORMAT(I7,6E12.5E2)
      C1449 FORMAT(6X,17HSTRESS COMPONENTS)
      1450  FORMAT(6E12.5E2)
            STOP
            END
```

UTL.WRITE80/ASCII

```
UTL(1).WRITE80/ASCII(2)
            IDENTIFICATION DIVISION.
            PROGRAM-ID. WRITEASCII.
            ENVIRONMENT DIVISION.
            CONFIGURATION SECTION.
            SOURCE-COMPUTER. UNIVAC-1108.
            OBJECT-COMPUTER. UNIVAC-1108.
            INPUT-OUTPUT SECTION.
            FILE-CONTROL.
                SELECT  INFILE   ASSIGN TO CARD-READER.
                SELECT  OUT  ASSIGN TO INTERCHANGE Z.
            DATA DIVISION.
            FILE SECTION.
            FD  INFILE   LABEL RECORD IS OMITTED RECORDING MODE F
                         BLOCK CONTAINS     40     RECORDS.
            01  INREC   PIC X(80).
            FD  OUT  LABEL RECORD IS OMITTED
            RECORDING MODE F
            BLOCK CONTAINS 40 RECORDS.
            01  OUTREC  PIC X(80).
            WORKING-STORAGE SECTION.
            01  COUNTIT   PIC 99999  VALUE 0.
            PROCEDURE DIVISION.
            STARTIT.
                OPEN INPUT  INFILE WITH NO REL NO.
                OPEN OUTPUT OUT WITH NO REWIND.
            LOOP.
                READ INFILE     AT END GO TO THEND.
                     ADD 1 TO COUNTIT.
                MOVE INREC   TO  OUTREC.
                WRITE OUTREC.
                GO TO LOOP.
            THEND.
                CLOSE INFILE   WITH NO REWIND.
                CLOSE OUT WITH NO REWIND.
                     DISPLAY ' COUNT ' COUNTIT  UPON PRINTER.
                STOP  RUN.
```

FILEPREP

```
  1:#DELETE E=D1.,D2.,D3.,D4.,D5.,D6.,D7.,D8.,D9.,D10.,D11.,D12.,D13.,
14.,
D15.,D16.,D17.,D18.,D19.,D20.,D21.
  2:#DELETE E=P1.,P2.,P3.,P4.,P5.,P6.,P7.,P8.,P9.,P10.,P11.,P12.,P13.,
14.,
P15.,P16.,P17.,P18.,P19.,P20.,P21.
  3:#EDIT F.
  4:MAKE(1,23) D1.
  5:MAKE(24,8) P1.
  6:MAKE(27,23) D2.
  7:MAKE(50,8) P2.
  8:MAKE(53,23) D3.
  9:MAKE(76,8) P3.
 10:MAKE(79,23) D4.
 11:MAKE(102,8) P4.
 12:MAKE(105,23) D5.
 13:MAKE(128,8) P5.
 14:MAKE(131,23) D6.
 15:MAKE(154,8) P6.
 16:MAKE(157,23) D7.
 17:MAKE(180,8) P7.
 18:MAKE(183,23) D8.
 19:MAKE(206,8) P8.
 20:MAKE(209,23) D9.
 21:MAKE(232,8) P9.
 22:MAKE(235,23) D10.
 23:MAKE(258,8) P10.
 24:MAKE(261,23) D11.
 25:MAKE(284,8) P11.
 26:MAKE(287,23) D12.
 27:MAKE(310,8) P12.
 28:MAKE(313,23) D13.
 29:MAKE(336,8) P13.
 30:MAKE(339,23) D14.
 31:MAKE(362,8) P14.
 32:MAKE(365,23) D15.
 33:MAKE(388,8) P15.
 34:MAKE(391,23) D16.
 35:MAKE(414,8) P16.
 36:MAKE(417,23) D17.
 37:MAKE(440,8) P17.
 38:MAKE(443,23) D18.
 39:MAKE(466,8) P18.
 40:MAKE(469,23) D19.
 41:MAKE(492,8) P19.
 42:MAKE(495,23) D20.
 43:MAKE(518,8) P20.
 44:MAKE(521,23) D21.
 45:MAKE(544,8) P21.
 46:EXIT
 47:#NEWUTILITY
 48:GEON READ
 49:ALL.
 50:N
 51:
 52:FUNC READ
 53:P1.
 54:Y
 55:WRIT
 56:P1.
 57:READ
 58:P2.
 59:Y
 60:WRIT
 61:P2.
 62:READ
 63:P3.
 64:Y
 65:WRIT
 66:P3.
 67:READ
 68:P4.
 69:Y
 70:WRIT
 71:P4.
 72:READ
 73:P5.
 74:Y
 75:WRIT
 76:P5.
 77:READ
 78:P6.
 79:Y
 80:WRIT
 81:P6.
 82:READ
 83:P7.
 84:Y
 85:WRIT
 86:P7.
 87:READ
 88:P8.
 89:Y
 90:WRIT
 91:P8.
 92:READ
 93:P9.
 94:Y
 95:WRIT
 96:P9.
 97:READ
 98:P10.
 99:Y
100:WRIT
101:P10.
102:READ
103:P11.
104:Y
105:WRIT
106:P11.
107:READ
108:P12.
109:Y
110:WRIT
111:P12.
112:READ
113:P13.
114:Y
115:WRIT
116:P13.
117:READ
118:P14.
```

```
119:Y
120:WRIT
121:P14.
122:READ
123:P15.
124:Y
125:WRIT
126:P15.
127:READ
128:P16.
129:Y
130:WRIT
131:P16.
132:READ
133:P17.
134:Y
135:WRIT
136:P17.
137:READ
138:P18.
139:Y
140:WRIT
141:P18.
142:READ
143:P19.
144:Y
145:WRIT
146:P19.
147:READ
148:P20.
149:Y
150:WRIT
151:P20.
152:READ
153:P21.
154:Y
155:WRIT
156:P21.
157:EXIT
158:#SECTION
159:ALL.
160:
161:ALL.U
162:21
163:D1.
164:D1.U
165:D2.
166:D2.U
167:D3.
168:D3.U
169:D4.
170:D4.U
171:D5.
172:D5.U
173:D6.
174:D6.U
175:D7.
176:D7.U
177:D8.
178:D8.U
179:D9.
180:D9.U
181:D10.
182:D10.U
183:D11.
184:D11.U
185:D12.
186:D12.U
187:D13.
188:D13.U
189:D14.
190:D14.U
191:D15.
192:D15.U
193:D16.
194:D16.U
195:D17.
196:D17.U
197:D18.
198:D18.U
199:D19.
200:D19.U
201:D20.
202:D20.U
203:D21.
204:D21.U
205:21
206:P1.
207:P1.U
208:P2.
209:P2.U
210:P3.
211:P3.U
212:P4.
213:P4.U
214:P5.
215:P5.U
216:P6.
217:P6.U
218:P7.
219:P7.U
220:P8.
221:P8.U
222:P9.
223:P9.U
224:P10.
225:P10.U
226:P11.
227:P11.U
228:P12.
229:P12.U
230:P13.
231:P13.U
232:P14.
233:P14.U
234:P15.
235:P15.U
236:P16.
237:P16.U
238:P17.
239:P17.U
240:P18.
241:P18.U
242:P19.
243:P19.U
244:P20.
245:P20.U
246:P21.
247:P21.U
248:
249:
```

LOOK

```
 1:MOVIE
 2:ALL.U
 3:D17.U
 4:P17.U
 5: ROTA
 6: Y -30 X 25
 7:CONT
 8:17 23
 9:-10  0
10:VIEW
11:READ
12:
13:D13.U
14:P18.U
15:VIEW
16:READ
17:
18:D13.U
19:P19.U
20:VIEW
21:READ
22:
23:D20.U
24:P20.U
25:VIEW
26:READ
27:
28:D21.U
29:P21.U
30:VIEW
31:ANIM
32:5
33:1 5
34:Y
35:N
36:
37:
38:
39:
40:
41:1
42:
43:
44:VIEW
45:
46:
47:
48:
49:EXIT
```

APPENDIX B

Basics of Viscoelasticity

1. **Elastic material** - A material is called elastic if the current stress depends on the current strain only,

$$\sigma(t) = E \cdot \varepsilon(t) \quad .$$

2. **Viscoelastic material** - A material is called viscoelastic if the current stress depends on not only the current strain but also the entire past deformation history,

$$\sigma(t) = \int_{\tau=0}^{\infty} [\varepsilon(t - \tau)] \quad .$$

3. **The most familiar viscoelastic behaviors**

   a. **Relaxation**

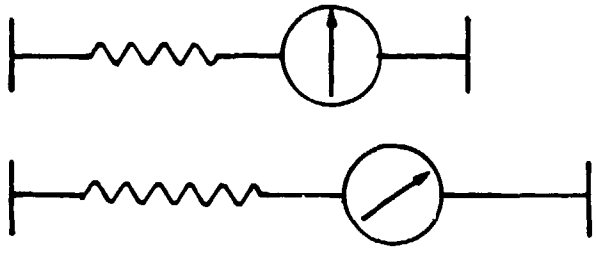

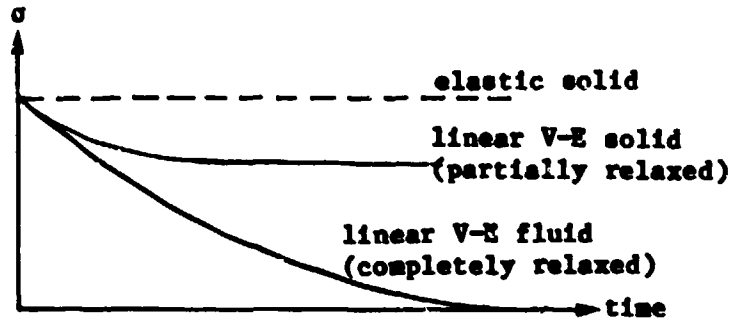

   b. **Creep**

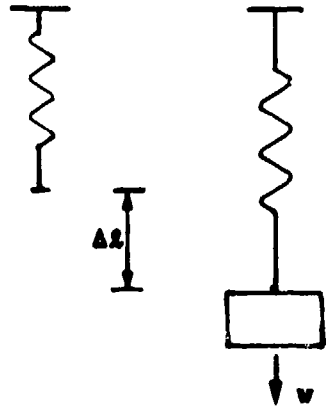

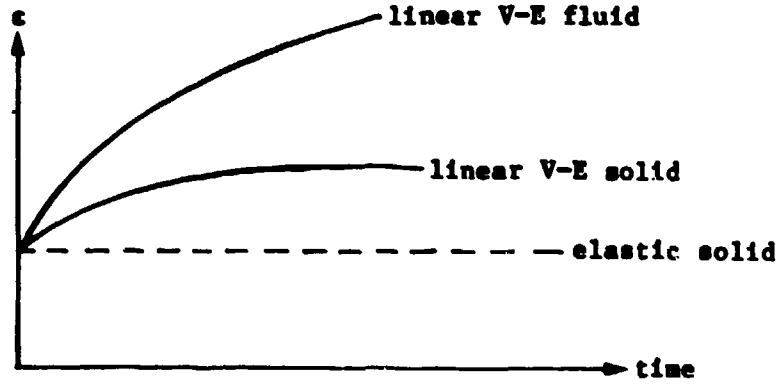

4. Linear viscoelastic material

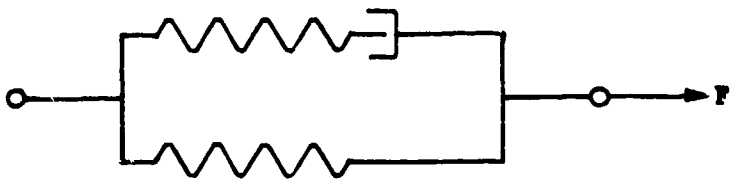

$$F + \tau_\varepsilon \frac{dF}{dt} = E_R\left(u + \tau_\sigma \frac{du}{dt}\right) \quad . \tag{1}$$

a. For unit step displacement at t, u(t) = 1(t), we can get relaxation function,

$$k(t) = E_R\left[1 - \left(1 - \frac{\tau_\sigma}{\tau_\varepsilon}\right) e^{-t/\tau_\varepsilon}\right] 1(t) \quad . \tag{2}$$

b. For unit step loading at t, F(t) = 1(t), we get creep function,

$$c(t) = \frac{1}{E_R}\left[1 - \left(1 - \frac{\tau_\varepsilon}{\tau_\sigma}\right) e^{-t/\tau_\sigma}\right] 1(t) \quad , \tag{3}$$

where

τ_σ = the time of relaxation of deflection under constant load,

τ_ε = the time of relaxation of load under constant deflection,

E_R = relaxed elastic modulus, and

1(t) = unit-step function, defined as

$$1(t) = \begin{cases} 1 & \text{when } t > 0 \\ 1/2 & \text{when } t = 0 \\ 0 & \text{when } t < 0 \end{cases} \quad .$$

To generalize the above formulation for a simple bar, which actually consists of infinite degrees of freedom, Boltzmann wrote

$$u(t) = \int_{-\infty}^{t} c(t - \tau) \frac{\partial F}{\partial \tau} (\tau) \, d\tau \quad , \tag{4}$$

and

$$F(t) = \int_{-\infty}^{t} k(t - \tau) \frac{du}{d\tau} (\tau) \, d\tau \quad , \tag{5}$$

to account for the linear load-deflection relationship of a simple bar.

In a complete description for the linear viscoelastic solid, in terms of stress and strain, we can rewrite

$$\sigma(t) = \int_{-\infty}^{t} K(t - \tau) \cdot d\varepsilon = \int_{-\infty}^{t} K(t - \tau) \cdot \dot{\varepsilon} \cdot d\tau \quad , \tag{6}$$

or

$$\varepsilon(t) = \int_{-\infty}^{t} C(t - \tau) \cdot d\sigma = \int_{-\infty}^{t} C(t - \tau) \cdot \dot{\sigma} \cdot d\tau \quad . \tag{7}$$

5. **Nonlinear viscoelastic material** (Green & Rivlin)

$$\sigma(t) = \int_{-\infty}^{t} \phi_1(t - \tau) \, \dot{\varepsilon}(\tau) \, d\tau + \iint_{-\infty}^{t} \phi_2(t - \tau, \, t - s) \cdot \dot{\varepsilon}(\tau) \cdot \dot{\varepsilon}(s) \, d\tau \, ds$$

$$+ \iiint_{-\infty}^{t} \phi_3(t - \tau, \, t - s, \, t - r) \cdot \dot{\varepsilon}(\tau) \cdot \dot{\varepsilon}(s) \cdot \dot{\varepsilon}(r) \, d\tau \, ds \, dr \quad .$$

$$+ \ldots . \tag{8}$$

6. **Quasi-linear viscoelastic material** (Fung)

$$\sigma(t) = \int_{-\infty}^{t} \Phi(t - \tau) \cdot d\dot{\sigma}^{(e)}(\tau)$$

$$= \int_{-\infty}^{t} \Phi(t - \tau) \cdot \left(\frac{d\sigma^{(e)}}{d\varepsilon}\right)\left(\frac{d\varepsilon}{d\tau}\right) \cdot d\tau \quad . \tag{9}$$

where

σ = stress at time t,

$\sigma^{(e)}$ = elastic response at time t,

ε = strain measure,

Φ = reduced relaxation function.

APPENDIX C. LIST OF EXPERIMENTAL DATA FROM WRAIR/LOVELACE ITRI

1. On the following experiments we have raw data from chart recorders.

Date	Explosive	Type	Range (ft)	HOB (ft)	Animal Orientation
092881	8 lb TNT	free field	21.3	3.2	right side on
100281	16 lb TNT	free field	27.0	6.0	right side on
092981	32 lb TNT	free field	44.4	8.0	right side on
093081	64 lb TNT	free field	76.3	10.1	right side on
?	10 ft. length 100 grain prime cord	shock tube	58.25		against end plate
120381	31 ft. length 100 grain prime cord	shock tube	58.25		
120481	61 ft. length 100 grain prime cord	shock tube	58.25		

2. These are experiments abstracted from Lovelace report, "Double Peak Study" on which we have raw data.

Date	Animal Number	Animal Location	Explosive	Range (ft)	Time Duration Between Shocks (ms)	Animal Orientation
			PART 1 (October 1981)			
102881	2	North	2-8 lb TNT	11	1.7	right side on
	1	North	2-8 lb TNT		3.6	right side on
102781	3	North	2-8 lb TNT	11	5.6	right side on
	2	North	2-8 lb TNT		7.6	right side on
102581	14	East	2-8 lb TNT	11	9.7	right side on
102781	1	North	2-8 lb TNT	11	11.5	right side on
102681	1	North	2-8 lb TNT	11	13.6	right side on
			PART 2 (May 1982)			
051382	2	West	8 lb pentolite charges	10.0	3.8	right side on
	1	East	8 lb pentolite charges		3.8	right side on
051182	2	West	8 lb pentolite charges	10.5	9.9	right side on
	1	East	8 lb pentolite charges		9.8	right side on
051182	2	West	8 lb pentolite charges	10.5	9.7	right side on
			PART 3 (May 1982)			
051782	2	West	8 lb pentolite charges	11	9.6	right side on
	1	East	8 lb pentolite charges		9.6	right side on
052182	2	West	8 lb pentolite charges	11	9.6	right side on
	1	East	8 lb pentolite charges		9.6	right side on
051982	2	West	8 lb pentolite charges	11	3.7	right side on
	1	East	8 lb pentolite charges		3.7	right side on
052082	2	West	8 lb pentolite charges	11	3.7	right side on
	1	East	8 lb pentolite charges		3.7	right side on

DISTRIBUTION LIST

12 copies	Director Walter Reed Army Institute of Research Walter Reed Army Medical Center ATTN: SGRD-UWZ-C Washington, DC 20307-5100
1 copy	Commander US Army Medical Research and Development Command ATTN: SGRD-RMI-S Fort Detrick, Frederick, MD 21701-5012
12 copies	Defense Technical Information Center (DTIC) ATTN: DTIC-DDAC Cameron Station Alexandria, VA 22304-6145
1 copy	Dean School of Medicine Uniformed Services University of the Health Sciences 4301 Jones Bridge Road Bethesda, MD 20814-4799
1 copy	Commandant Academy of Health Sciences, US Army ATTN: AHS-CDM Fort Sam Houston, TX 78234-6100